In compliance with the
Canadian Privacy Legislation
some supporting forms
may have been removed from
this dissertation.

While these forms may be included
in the document page count,
their removal does not represent
any loss of content from the dissertation.

University of Alberta

Size-Distributions for North-East Pacific Plate Boundary

by

Zuzana Dobiasova

A thesis submitted to the Faculty of Graduate Studies and Research in partial fulfillment of the requirements for the degree of **Master of Science**.

in

Geophysics

Department of Physics

Edmonton, Alberta
Fall 2003

National Library of Canada
Acquisitions and Bibliographic Services
395 Wellington Street
Ottawa ON K1A 0N4
Canada

Bibliothèque nationale du Canada
Acquisisitons et services bibliographiques
395, rue Wellington
Ottawa ON K1A 0N4
Canada

Your file Votre référence
ISBN: 0-612-87750-7
Our file Notre référence
ISBN: 0-612-87750-7

The author has granted a non-exclusive licence allowing the National Library of Canada to reproduce, loan, distribute or sell copies of this thesis in microform, paper or electronic formats.

The author retains ownership of the copyright in this thesis. Neither the thesis nor substantial extracts from it may be printed or otherwise reproduced without the author's permission.

L'auteur a accordé une licence non exclusive permettant à la Bibliothèque nationale du Canada de reproduire, prêter, distribuer ou vendre des copies de cette thèse sous la forme de microfiche/film, de reproduction sur papier ou sur format électronique.

L'auteur conserve la propriété du droit d'auteur qui protège cette thèse. Ni la thèse ni des extraits substantiels de celle-ci ne doivent être imprimés ou aturement reproduits sans son autorisation.

Canada

University of Alberta

Library Release Form

Name of Author: Zuzana Dobiasova

Title of Thesis: Size-Distributions for North-East Pacific Plate Boundary

Degree: Master of Science

Year this Degree Granted: 2003

Permission is hereby granted to the University of Alberta Library to reproduce single copies of this thesis and to lend or sell such copies for private, scholarly or scientific research purposes only.

The author reserves all other publication and other rights in association with the copyright in the thesis, and except as hereinbefore provided, neither the thesis nor any substantial portion thereof may be printed or otherwise reproduced in any material form whatever without the author's prior written permission.

Date: Jan 5, 2003

University of Alberta

Faculty of Graduate Studies and Research

The undersigned certify that they have read, and recommend to the Faculty of Graduate Studies and Research for acceptance, a thesis entitled **Size-Distributions for North-East Pacific Plate Boundary** submitted by Zuzana Dobiasova in partial fulfillment of the requirements for the degree of **Master of Science** in Geophysics.

Date: Jan. 5, 2003

Abstract

The Gutenberg-Richter (GR) relation, a widely used model for scaling of the earthquake size distributions, has been the subject of numerous studies. The GR relation is a power-law moment-frequency distribution, which implies that the earthquake rupture processes are scale invariant. However, the size distributions for large earthquakes deviate from GR scaling. These deviations indicate effects of characteristic scales of a fault or fault system. In this work we are interested how the fault geometry affects the earthquake scaling. To achieve this, we have studied the faults of the North East Pacific plate boundary.

An important characteristic scale associated with individual faults is the characteristic rupture length. The characteristic rupture length is marked by a departure from the GR relation in earthquake statistics, such that the GR relation overestimates the number of large earthquakes. Seismic moment and rupture length distributions were examined for several marine strike-slip faults with different lengths, widths, and aspect ratios (defined as the length divided by the width). Characteristic scaling can be explained by width or length saturation. Length (width) saturation means that the horizontal (vertical) size of the rupture is comparable with the total length (width) of the fault. While in case of width saturation the remaining energy can be released in the horizontal direction, no further horizontal release is possible for length saturation case. Examined were data for the Queen Charlotte fault, which has the best fit characteristic length 468 km (total fault length is 1120 km). Thus width saturation is suggested for this fault. The other studied faults, Revere-Dellwood, Sovanco and Nootka with significantly lower aspect ratios, have their characteristic lengths comparable or smaller to the total fault lengths. Thus both the length and width saturations are possible for these short faults.

Two models for size distribution scaling exist in the literature: the L model, which states that the size distribution scaling for the large earthquakes is proportional to the square of the rupture length, and the W model, which predicts linear scaling with the rupture length. Our examination of β values from seismic moment-frequency distributions generally follows (with some exceptions) the L rather than the W model.

Vanity of vanities, saith the Preacher, vanity of vanities; all is vanity.
What profit hath a man of all his labour which he taketh under the sun?
One generation passeth away, and another generation cometh:
but the earth abideth for ever.
(Ecclesiastes 1:2-4)

To the glory of God

Acknowledgements

I want to thank my family, especially my husband Peter, for their patience and for the overwhelming support they gave me during my research work. I'm also very thankful to my supervisor, Dr. Moritz Heimpel, for introducing me to this research area and for all help and encouragement he gave me. Special thanks go to R. Hyndman, J. Ristou, and T. Mulder from Pacific Geoscience Centre for many fruitful discussions and information on the seismic databases.

Contents

1 Tectonic Setting 4

1.1 Tectonic evolution 4

1.2 A Structure of Faults and Ridges 5

1.2.1 The Northern Pacific - North America plate boundary 5

1.2.2 Pacific - Juan de Fuca plate boundary 6

1.2.3 Cascadia Subduction Zone 10

2 Overview of the Statistics 13

2.1 Mechanics of earthquakes 13

2.1.1 Crack Propagation and Formation of Faults 13

2.1.2 Earthquake Phenomenology 14

2.2 Qualification and Quantification of Earthquakes 15

2.2.1 Fault-Plane Solution 15

2.2.2 Earthquake Size 17

2.3 Scaling Relations 19

2.3.1 Gutenberg - Richter Scaling Relation 19

2.3.2 The Deviations from GR 21

2.3.3 Fractal Approach to Scaling Relations 23

3 Data Analysis 25

3.1 Databases 25

3.2 Magnitude - Moment Conversion 26

3.3 Moment-frequency distributions 28

3.3.1 Selection of regions 28

3.3.2 Curve fitting 28

3.3.3 Results for moment distributions 29

3.4 Length-frequency distributions 54

3.4.1 Moment - length conversion 54
3.4.2 Results for length distributions 60
3.5 Numerical Models 76
3.6 Discussion 82
3.7 Error evaluation 85

4 Conclusions **87**

Bibliography **90**

List of Figures

1 Kelsey Bay Hwy., Vancouver Island, after 1946 earthquake. Picture courtesy PGC-NRCAN, Sidney, BC. 1

2 Nuclear power plant Jaslovske Bohumnice, Slovak Republic. (Picture fei.stuba.sk). 2

3 The dam in Gabcikovo, Slovak Republic. (Picture courtesy qccontrol.sk) . . 2

1.1 North East Pacific plate boundary (present situation); fault (line); ridge (bold line); arrow refers to the motion on the fault. 12

2.1 Fundamental types of fault motion. a) A block with a fault before any motion has taken place. For description of b), c), d) see text. (From Bath [1979]) . 16

2.2 Fault-plane solution for a) vertical strike slip, b) nonvertical strike slip, c) normal and d) thrust fault. (From Fowler [1990]) 16

2.3 Illustration of cumulative size distribution of earthquakes for a) a single fault or plate boundary segment and b) a large region containing many faults or plate boundary segments. (From Scholz [1997]) 22

3.1 Corresponding moment magnitude (M_w) and local magnitude (M_L) for 95 earthquakes 27

3.2 Top: pink - chosen region (from now on will be referred as $QC1$). Bottom: moment-frequency distribution with fitting curve (-) for cumulative dist. (o); bin dist. (+). For more details see text. 34

3.3 Top: pink - chosen region (from now on will be referred as $QC2$). Bottom: moment-frequency distribution with fitting curve (-) for cumulative dist. (o); bin dist. (+). For more details see text. 35

3.4 Top: pink - chosen region (from now on will be referred as $RD1$). Bottom: moment-frequency distribution with fitting curve (-) for cumulative dist. (o); bin dist. (+). For more details see text. 36

3.5 Top: pink - chosen region (from now on will be referred as $RD2$). Bottom: moment-frequency distribution with fitting curve (-) for cumulative dist. (o); bin dist. (+). For more details see text. 37
3.6 Top: pink - chosen region (from now on will be referred as $RD3$). Bottom: moment-frequency distribution with fitting curve (-) for cumulative dist. (o); bin dist. (+). For more details see text. 38
3.7 Top: pink - chosen region (from now on will be referred as $So1$). Bottom: moment-frequency distribution with fitting curve (-) for cumulative dist. (o); bin dist. (+). For more details see text 39
3.8 Top: pink - chosen region (from now on will be referred as $So2$). Bottom: moment-frequency distribution with fitting curve (-) for cumulative dist. (o); bin dist. (+). For more details see text 40
3.9 Top: pink - chosen region (from now on will be referred as $So3$). Bottom: moment-frequency distribution with fitting curve (-) for cumulative dist. (o); bin dist. (+). For more details see text. 41
3.10 Top: pink - chosen region (from now on will be referred as $No1$). Bottom: moment-frequency distribution with fitting curve (-) for cumulative dist. (o); bin dist. (+). For more details see text. 42
3.11 Top: pink - chosen region (from now on will be referred as $No2$). Bottom: moment-frequency distribution with fitting curve (-) for cumulative dist. (o); bin dist. (+). For more details see text. 43
3.12 Top: pink - chosen region (from now on will be referred as $No3$). Bottom: moment-frequency distribution with fitting curve (-) for cumulative dist. (o); bin dist. (+). For more details see text. 44
3.13 Top: pink - chosen region (from now on will be referred as $SoNo1$). Bottom: moment-frequency distribution with fitting curve (-) for cumulative dist. (o); bin dist. (+). For more details see text. 45
3.14 Top: pink - chosen region (from now on will be referred as $SoNo2$). Bottom: moment-frequency distribution with fitting curve (-) for cumulative dist. (o); bin dist. (+). For more details see text. 46
3.15 Top: pink - chosen region (from now on will be referred as $RDSoNo$). Bottom: moment-frequency distribution with fitting curve (-) for cumulative dist. (o); bin dist. (+). For more details see text. 47

3.16 Top: pink - chosen region (from now on will be referred as $Bl1$). Bottom: magnitude-frequency distribution; cumulative dist. (o); bin dist. (+). For more details see text. 48
3.17 Top: pink - chosen region (from now on will be referred as $Bl21$). Bottom: magnitude-frequency distribution; cumulative dist. (o); bin dist. (+). For more details see text. 49
3.18 Top: pink - chosen region (from now on will be referred as $Bl22$). Bottom: magnitude-frequency distribution; cumulative dist. (o); bin dist. (+). For more details see text. 50
3.19 Top: pink - chosen region (from now on will be referred as $Me1$). Bottom: magnitude-frequency distribution; cumulative dist. (o); bin dist. (+). For more details see text. 51
3.20 Top: pink - chosen region (from now on will be referred as $Me2$). Bottom: magnitude-frequency distribution; cumulative dist. (o); bin dist. (+). For more details see text. 52
3.21 Top: pink - chosen region (from now on will be referred as $Me3$). Bottom: magnitude-frequency distribution; cumulative dist. (o); bin dist. (+). For more details see text. 53
3.22 The mean slip over stress drop (scaled according to Yin and Rogers [1996]) as a function of aspect ratio as a result of numerical models. 58
3.23 Geometry of the used ruptures, circular (red), elliptical (blue) as proposed in Yin and Rogers [1996] 58
3.24 Top: slip (in model units) on circular rupture. The figure shows 1/10 of the full length of the fault of aspect ratio 25. Bottom: slip (in model units) on elliptical rupture. Shape of ruptures defined in Yin and Rogers [1996]. Figures provided by M. Heimpel. 59
3.25 Length-frequency distribution for $QC1$, with fitting curve (-) for cumulative dist. (o); bin dist. (+). Width of the fault is 20 km (top) and 30 km (bottom). Stress drop is 0.75 MPa for a), c), 1.471 MPa for b), and 1.009 MPa for d). For more details see text. 62
3.26 Length-frequency distribution for $QC2$, with fitting curve (-) for cumulative dist. (o); bin dist. (+). Width of the fault is 20 km (top) and 30 km (bottom). Stress drop is 0.75 MPa for a), c), 1.471 MPa for b), and 1.009 MPa for d). For more details see text. 63

3.27 Length-frequency distribution for $RD1$, with fitting curve (-) for cumulative dist. (o); bin dist. (+). Width of the fault is 5 km, stress drop is 0.75 MPa (top) and 1.471 MPa (bottom). For more details see text. 64
3.28 Length-frequency distribution for $RD2$, with fitting curve (-) for cumulative dist. (o); bin dist. (+). Width of the fault is 5 km, stress drop is 0.75 MPa (top) and 1.471 MPa (bottom). For more details see text. 65
3.29 Length-frequency distribution for $RD3$, with fitting curve (-) for cumulative dist. (o); bin dist. (+). Width of the fault is 5 km, stress drop is 0.75 MPa (top) and 1.471 MPa (bottom). For more details see text. 66
3.30 Length-frequency distribution for $So1$, with fitting curve (-) for cumulative dist. (o); bin dist. (+). Width of the fault is 5 km, stress drop is 0.75 MPa (top) and 1.471 MPa (bottom). For more details see text. 67
3.31 Length-frequency distribution for $So2$, with fitting curve (-) for cumulative dist. (o); bin dist. (+). Width of the fault is 5 km, stress drop is 0.75 MPa (top) and 1.471 MPa (bottom). For more details see text. 68
3.32 Length-frequency distribution for $So3$, with fitting curve (-) for cumulative dist. (o); bin dist. (+). Width of the fault is 5 km, stress drop is 0.75 MPa (top) and 1.471 MPa (bottom). For more details see text. 69
3.33 Length-frequency distribution for $No1$, with fitting curve (-) for cumulative dist. (o); bin dist. (+). Width of the fault is 5 km, stress drop is 0.75 MPa (top) and 1.471 MPa (bottom). For more details see text. 70
3.34 Length-frequency distribution for $No2$, with fitting curve (-) for cumulative dist. (o); bin dist. (+). Width of the fault is 5 km, stress drop is 0.75 MPa (top) and 1.471 MPa (bottom). For more details see text. 71
3.35 Length-frequency distribution for $No3$, with fitting curve (-) for cumulative dist. (o); bin dist. (+). Width of the fault is 5 km, stress drop is 0.75 MPa (top) and 1.471 MPa (bottom). For more details see text. 72
3.36 Length-frequency distribution for $SoNo1$, with fitting curve (-) for cumulative dist. (o); bin dist. (+). Width of the fault is 5 km, stress drop is 0.75 MPa (top) and 1.471 MPa (bottom). For more details see text. 73
3.37 Length-frequency distribution for $SoNo2$, with fitting curve (-) for cumulative dist. (o); bin dist. (+). Width of the fault is 5 km, stress drop is 0.75 MPa (top) and 1.471 MPa (bottom) For more details see text. 74

3.38 Length-frequency distribution for *RDSoNo*, with fitting curve (-) for cumulative dist. (o); bin dist. (+). Width of the fault is 5 km, stress drop is 0.75 MPa (top) and 1.471 MPa (bottom). For more details see text. 75
3.39 Top: moment-frequency distribution. Bottom: length-frequency distribution. Fitting curve (-), cumulative (o) and bin distribution (+). 78
3.40 Top: moment-frequency distribution. Bottom: length-frequency distribution. Cumulative (o) and bin distribution (+). 79
3.41 Top: moment-frequency distribution. Bottom: length-frequency distribution. Fitting curve (-), cumulative (o) and bin distribution (+). 80
3.42 Top: moment-frequency distribution. Bottom: length-frequency distribution. Fitting curve (-), cumulative (o) and bin distribution (+). 81

Introduction

Many important human centers are localized on, or close to, active seismic zones. As examples, we can mention the California coast (San Andreas Fault), Mexico-City and surrounding area, Japan, or the Mediterranean (Turkey, Italy) region. Therefore estimates of the seismic hazard, or possibly even prediction of earthquakes, are of vital importance. The possible impacts of large earthquakes in densely inhabited centers can be damaging (Fig. 1), and perhaps deadly. The estimate of seismic hazard is important not only for regions directly in the active zones, but also in other areas with less frequent earthquakes. For instance, the building sites for nuclear power plants (Fig. 2), localities for large dams (Fig. 3), and other large scale developments require careful quantification of possible seismic hazards, to minimize the threat to their surrounding (often large) region. Especially for nuclear power plants, the possible contamination due to even small leaks can reach hundreds of square miles.

Figure 1: Kelsey Bay Hwy., Vancouver Island, after 1946 earthquake. Picture courtesy PGC-NRCAN, Sidney, BC.

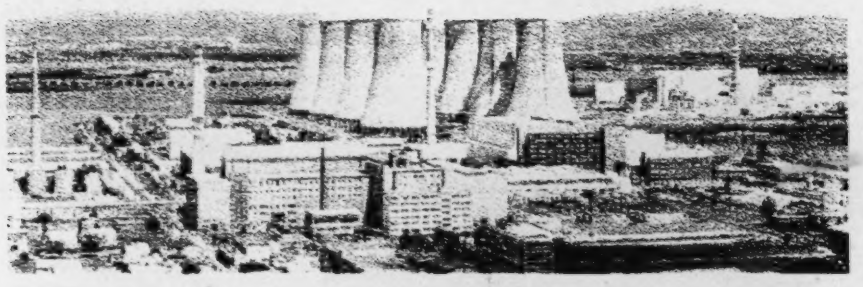

Figure 2: Nuclear power plant Jaslovske Bohumnice, Slovak Republic. (Picture fei.stuba.sk).

Figure 3: The dam in Gabcikovo, Slovak Republic. (Picture courtesy qccontrol.sk)

To evaluate seismic hazards in certain regions, various methods can be employed. One of the possible methods is the statistical evaluation of the history of previous earthquakes in the region. For instance, the cumulative numbers of earthquakes can provide us with a hint of the strength of possible earthquakes we can expect. Size frequency distributions of earthquakes are often approximated by the Gutenberg-Richter (GR) distribution [Gutenberg and Richter, 1944; 1954]. This approximation usually works well for smaller earthquakes. However, for large earthquakes the distribution is typically not valid, and the GR approximation is apparently not sufficient (because the large earthquakes scale differently from small ones).

A modified GR distribution that accounts for a scaling change for large earthquakes is

often a very good choice [Utsu, 1999]. Distributions that are linear for small earthquakes with an exponential decrease for large earthquakes describe the data behavior much better than the GR relation.

One of the factors affecting possible seismic hazard is the geometry of the fault. However, this factor is usually neglected in the statistical evaluation of seismic activity. In this work we present size-frequency distributions, and study their dependence on the fault geometry. This work does not claim to be a comprehensive study of global seismic activity, but focuses on several faults in the North East Pacific region.

A major problem with the statistical evaluation of earthquake activity is the incompatibility between various sources of accessible data. This is further combined with certain inaccuracies that are inherent for any seismic database. These inaccuracies are primarily caused by the fact that it is impossible to measure earthquake parameters directly. Instead they are obtained from seismic wave measurements, often very far from the epicenter of the earthquake itself. Another large factor is also the incompleteness of the databases.

We present statistics for the Queen Charlotte, Revere-Dellwood, Sovanco, Nootka, Blanco, and Mendocino faults. We used Pacific Geoscience Centre (PGC) and Advanced National Seismic System (ANSS) earthquake databases. We used a modified GR distribution [Utsu, 1999] to evaluate the statistical distributions. Seismic moment/magnitude and rupture length distributions were calculated for most of the above-mentioned faults, and the dependence of the statistics on the fault geometry was studied.

In the first two chapters we review the information about the geologic structure, and the geometric parameters of the North East Pacific plate boundary. We also include an overview of the numerous studies about the b-value (the slope of the GR distribution).

In chapter three we describe the data sources we used, format of available data, and regional selection for specific faults. It is followed by the statistical analysis of the faults, including methods for the fitting of the data and a detailed discussion of the results. We also present statistics of the numerically modeled seismic activity [Heimpel, 1997; 2003]. Then we compare these simulation results to observations. Numerical models can provide us with much better understanding of the dependence of the earthquake activity on the geometry of the fault, since it is possible to model a clear fault geometry. In contrast, the real faults have often very complicated geometry, and only the main features can be studied.

Chapter 1

Tectonic Setting

For our research we chose the North East (NE) Pacific plate boundary. Our attention was focused on marine transform faults (Queen Charlotte, Revere-Dellwood, Sovanco, Nootka, Blanco and Mendocino faults) situated on the Pacific-Juan de Fuca-North America plate boundary. Theoretically, marine transform faults have a simple structure - vertical strike slip motion. However, the situation in other regions of the Earth's crust, such as subduction zone fault systems are more complex.

1.1 Tectonic evolution

The origin of the tectonic structure of NE Pacific plate boundary region could be placed to roughly 55 Ma before present [Davis and Currie, 1993] when the Farallon Plate, surrounded by the Pacific and North American Plates, started to fragment. While the Pacific-Farallon plate boundary was a ridge crest, the Farallon-North America plate boundary was a subduction zone. At approximatelly 30 Ma one segment of the Pacific-Farallon Ridge started to be subducted under the North America Plate, which initiated the San Andreas Fault [Davis and Currie, 1993]. As the ridge subduction continued, the San Andreas Fault system growth also continued. Two newly created parts of the Farallon Plate separated by the San Andreas Fault are presently named Juan de Fuca and Cocos Plates. Both these plates have undergone complex history. Varying resistance of the Juan de Fuca Plate to subduction (the youngest parts show most resistance) caused differential rotation of the plate that caused a creation of the new subplate [Riddihough and Hyndman, 1991], in the North; the independent Explorer Plate, in which the internal deformation produced a small, independent, most recently formed fragment; the Winona Plate [Davis and Riddihough, 1982]. In the South part of the Juan de Fuca Plate the Gorda Plate broke off [Riddihough and Hyndman, 1991]. There is evidence that a microplate between the Winona, Pacific and North America

Plates could exist [Carbotte et al., 1989].

Today the situation (Figure 1.1) is characterized by the existence of several independent ocean ridges, separated by transform faults and separate plates and subplates. While some plates experience considerable internal deformation (Explorer, Gorda), in the others the internal deformation is rather small (Juan de Fuca) [Davis and Currie, 1993].

The present absolute motion (defined as motion relative to the hot spot reference frame) for the Pacific Plate off the Queen Charlotte Island is 51 mm/a (± 10 mm/a) at 320° (± 11°), for the North America Plate southwest of British Columbia, the estimate is 21 mm/a (± 12 mm/a) at 230° (± 30°) (it is less certain because hot spots are fewer and poorly defined), and for the Juan de Fuca Plate near Vancouver Island it is 25 mm/a (± 10 mm/a) at 62° (± 20°) [Riddihough and Hyndman, 1991]. For the differential slip rates see Table 1.1.

1.2 A Structure of Faults and Ridges

1.2.1 The Northern Pacific - North America plate boundary

The Pacific - North America plate boundary North of Vancouver Island to Alaska is formed by the Queen Charlotte Fault Zone (*QC*) and adjacent faults. In the Alaska region, the situation is quite difficult due to a triple junction between the Pacific and North America Plates and the Yakutat Block, starting at the Cross Sound. There are several opinions [Riddihough and Hyndman, 1991] on the current motion of the Yakutat Block. This block can be moving with the Pacific Plate and so the Fairweather Fault would be the Pacific - North America plate boundary, or it is moving independently from the Pacific Plate with a transform or thrust fault boundary, which continues to the Aleutian Trench (the thrust zone under Alaska). The primary collision zone between the Yakutat Block and the North America Plate is a thrust zone called Chugach - Saint Elias Fault System. This zone, with a great vertical motion, continues onshore to the Fairweather Fault with a strike - slip motion [Riddihough and Hyndman, 1991].

The seismic activity of the Denali Fault System in Yukon is lower, with slip rates up to 1 mm/a. The Denali Fault is connected to the Chatham Straight Fault which currently does not show any signs of seismic activity, and touches the *QC* North of the Dixon Entrance [Riddihough and Hyndman, 1991]. According to the seismic reflection profiles the Fairweather Fault System is an extension of the offshore Queen Charlotte Fault System (called also Queen Charlotte - Fairweather Fault System) which is predominantly a right-lateral

transform zone [Bruns et al, 1992]. The strike of this fault zone up to the Dixon Entrance is very similar to the Pacific - North America plate relative motion vector. But it differs from 7° up to 26° along the coast of the Queen Charlotte Islands [Rohr et al, 2000]. Wrench-fault structures (similar to those along the San Andreas Fault) and high, narrow, mid-slope ridges are present seaward, parallel to the Queen Charlotte Fault, from the Cross Sound to the Dixon Entrance [Bruns et al, 1992]. South of the Dixon Entrance the fault zone also becomes narrower and more linear. In this region a significant increase of the compression exists. The original theory of the existence of the underthrusting margin under the Queen Charlotte Islands [Hyndman and Ellis, 1981] seems to be brought into doubt by the recent study of Rohr et al [2000]. Their conclusion, based on new, multichannel, seismic reflection data, combined with other regional studies, suggests that the Pacific - North America plate boundary off the Queen Charlotte Islands (*QCI*) is a vertical strike-slip fault, and that transpression is taken up within each plate and so the *QCI* are the direct result of a trans-pressional deformation. There is clear evidence that the *QC* extends up to the northern edge of the Tuzo Wilson Seamounts, but there is no observable extension further southeast [Carbotte et al, 1989].

Both the Pacific and the North America Plates around the *QCI* have a current brittle-ductile transition (the depth above which 90% of the events occur) within the 13 to 21 km depth range, which is equivalent to the 700°C isotherm [Rohr et al, 2000]. According to Hyndman and Wiechert [1983], the depth of the Queen Charlotte Fault is 22 kilometers.

1.2.2 Pacific - Juan de Fuca plate boundary

The junction between the Pacific, North America and Explorer Plates creates a difficult situation. The regional tectonics are complicated due to the existence of one or more microplates and the interplate deformations [Carbotte et al, 1989] which define the triple junction of the major plates within the broad region between the Explorer and Tuzo Wilson spreading centre.

The border between the Pacific and Juan de Fuca Plates is characterized as a series of ridge segments (Tuzo Wilson Seamounts, Dellwood Knolls, Explorer, Juan de Fuca, and Gorda Ridges) and transform faults (Revere Dellwood, Sovanco, Nootka, Blanco, Mendocino).

Tuzo Wilson Seamounts (*TWS*) (10 km long and 3-3.5 km wide) are two distinct bathymetric highs separated by a saddle. The bathymetry mapping supports an idea that the morphology of the seamounts volcanism is associated with the seafloor spreading, although

they lack the lineated magnetic anomalies (this could be caused by the ridge jumps, rapid sedimentation, demagnetization) [Carbotte et al, 1989]. The Tuzo Wilson Seamounts are terminated as a spreading centre by the perpendicular border with the Queen Charlotte Fault to the North and the Revere Dellwood Fault Extention to the South. The existence of the Revere-Dellwood Fault Extention and a lack of the transform fault from the southwest end of the Tuzo Wilson Seamounts to the northeast of the Dellwood Knolls, as proposed by Carbotte et al [1989], rules out the former hypothesis of a separate existence of the Dellwood-Wilson and Revere-Dellwood transform faults.

The *Dellwood Knolls (DK)* could be considered a more developed, older analogy of the Tuzo Wilson Seamounts. Two models compatible with the data exist for these parallel features. One states that both segments are still active, simultaneous spreading centres, while the other states that the TWS and the DK were both spreading in the past, and now only the TWS persists actively [Carbotte et al, 1989].

The *Revere Dellwood Fault Extension (RDFE)* is a continuation of the Revere-Dellwood Fault. There is clear evidence for this from sea-floor imagery [Carbotte et al, 1989]. The $RDFE$ follows the southside end of the Dellwood Knolls to the southwest of the Tuzo Wilson Seamounts with the average trend 325° (nearly parallel to the QC on the opposite side of the TWS). An inactive part of the $RDFE$ can be traced from the TWS for about 50 km northwest [Carbotte et al, 1989].

The *Revere-Dellwood Fault (RD)* is a right lateral transform fault, linking the northern end of the Explorer Ridge, and the southwest end of the Dellwood Knolls. While the RD continues to the $RDFE$ in the West, its continuation in the East is by the Paul Revere Ridge (PRR) which is the uplifted, tilted, and subduced southern end of the Winona Block, initiated at about 1 Ma [Davis and Riddihough, 1982]. The PRR stretches 130 km southeast from the Explorer Ridge [Davis and Currie, 1993]. The total length of the RD and the $RDFE$, also called the Revere-Dellwood-Wilson Transform Fault, is approximately 140 km [Carbotte et al, 1989], and the seismicity is occuring in an area of a thin, hot lithosphere to depths of 3 to 8 km [Cassidy and Rogers, 1995].

The *Explorer Ridge* is the next segment in the Pacific - Juan de Fuca plate boundary, located off Vancouver Island (VI). The northern part of the ridge is formed by two parallel, deep, axial valleys. The northwestern valley is actively rifting, with the spreading rate of about 40 mm/a [Riddihough and Hyndman, 1991], while the second, parallel valley, located 35 km southeast, is probably dying [Davis and Currie, 1993]. The southern parts of the Explorer Ridge, characterized as a linear volcanic ridge, are plunging into a deep rift toward

the Sovanco Transform Fault Zone.

During its tectonic evolution, the Explorer Ridge underwent a series of clockwise twists and also migrated to the northwest [Riddihough, 1977]. Riddihough [1977] also suggested that this migration initiated the *Sovanco Transform Fault Zone (So)* about 7 Ma in the East - West direction.

A significant convergence of the Explorer and Pacific Plates across the *So* results in a highly anomalous morphology of this fault zone, "characterized by numerous distinct rhomboidal-shaped blocks, the sides of which are oriented roughly 60° and 135°, and by more continuous narrow ridges and depressions that on average strike approximately 125°" [Davis and Currie, 1993]. These structures lie between the southern Explorer and the northern Juan de Fuca Ridges in a length of 125 km and horizontal width of 30-34 km (width is defined by only lower resolution). Because of the difficult morphology and a probable internal deformation of the Explorer Plate the application of rigid - plate tectonics principles is not appropriate, and the tectonic history of the region cannot be well resolved [Davis and Currie, 1993].

The Explorer Plate (4 Ma old) is subducted under the North America Plate (21 mm/a, 50°) at less than half of the rate of the Juan de Fuca Plate (47 mm/a, 56°) [Clowes et al, 1997], which is consistent with the left lateral motion of the *Nootka Transform Fault Zone (No)* on the boundary.

The *No* is a 20 km horizontally wide zone of an active faulting in the ocean lithosphere [Hyndman et al, 1979]. While the northern end of the *No* subducts under the western edge of Vancouver Island, the southern end intersects the Juan de Fuca Ridge in a broad region of its Middle Valley (northeastern ridge). There are observed earthquakes in the subducted portion of the *No* with a left-lateral strike-slip motion, and with a small component of thrusting [Clowes et al, 1997]. A portion of the Nootka fault, already subducted under the *VI*, in which these quite large ($M \sim 6.7$) events occured, could be estimated to be several tens of kilometers from the continental shelf edge [Cassidy et al, 1988; Hyndman, 1995]. The south - western end is a more active part, filled with numerous, widespread, active faults [Hyndman et al, 1979].

The *Juan de Fuca Ridge (JdFR)*, bounded by the triple junction (Sovanco fault - Nootka fault - Juan de Fuca Ridge) on the North and by the Blanco Fracture Zone on the South, is denoted on a global scale as an intermediate, spreading ridge, with a rate of about 56 mm/a [Hooft and Detrick, 1995]. This ridge consists of several distinct spreading segments (the six major, from the North, are West Valley, Endeavour, Northern Symmetric, Axial

Seamount, Vance and Cleft). The morphology of the 500 km long Juan de Fuca Ridge is generally characterized by the rifted axial high although some of the segments (West Valley) show more of a rift valley morphology [Hooft and Detrick, 1995]. Although the genesis of the structure of spreading ridges in the Juan de Fuca Ridge system (including $JdFR, ER, DK, TWS$) is not well understood, it is connected to the temporal and spatial variations in the magma production along the ridges [Riddihough and Hyndman, 1991]. Hooft and Detrick [1995] show that for intermediate spreading ridges even relatively small changes result in a large difference in the ridge morphology.

The Juan de Fuca Ridge and the Gorda Ridge are linked by a 350 km long right-lateral *Blanco Transform Zone (Bl)*, located off the Oregon coast which consists of strike-slip fault sections, bounded by scarps or ridges and separated by deep extensional basins [Dziak et al, 1991]. The largest and the deepest of these basins is the Cascadia Depression, considered to be an active ridge segment located approximately in the middle of the Blanco Fault Zone. This implies the existence of two segments, northwest and southeast. The northwest segment is composed of three major strike-slip faults (each less than 60 km long) and two extensional basins in between them [Dziak et al, 1991]. The southeast segment has a single extensional basin between two major strike-slip faults. One of the faults connecting the Cascadia and Gorda Depressions, named Blanco Ridge (a series of heights delineated by a zone of a high angle right-lateral strike-slip motion, with a small component of dip-slip component) is about 150 km long and has no discontinuities along itself. On the Blanco Ridge (BR), the longest fault of the entire Bl, the largest earthquakes have occured, though more than 80% of the slip along the Bl seams to be aseismic (from a comparison of the plate motion and the seismic moment release) [Dziak et al, 2000].

The Pacific - Juan de Fuca plate boundary continues from the Blanco Fault Zone to the Gorda Ridge. The *Gorda Ridge (GR)*, as well as the Juan de Fuca Ridge is an example of the intermediate spreading center, with the rate about 56 mm/a at the northern end, decreasing to only about 24 mm/a at the southern end [Hyndman and Weichert, 1983]. There are three main parts of the GR, the northern, central and the southern Gorda Ridge, with the morphology generally characterized by a rift valley typical for slow spreading ridges [Hooft and Detrick, 1995]. Compared to the $JdFR$, Gorda Ridge is characterized by a thicker axial lithosphere and much higher level of seismicity associated with the thermal anomalies [Hooft and Detrick, 1995].

The *Mendocino Fracture Zone (MFZ)* can be characterized as a straight structure, more than 2000 km long, in the Pacific Plate, leading past the southern end of the Gorda Ridge

and joining the Mendocino triple junction (MTJ) near Cape Mendocino [Bakun, 2000]. The part from the Gorda Ridge to the coast is marked as the Mendocino Transform Fault (Me), showing signs of a right-lateral strike-slip motion [Bakun, 2000]. The major bathymetric feature of the Me is its single high transverse ridge (Mendocino Ridge), rising 270 km west of the California Coast. Topography of the Me is also atypical in the absence of a transform valley which is normally the principal zone of the deformation [Fisk et al, 1993]. Some studies suggest there is a subduction beneath the Mendocino Transform Fault, but there is no evidence (topographic or gravity) of material loss [Denlinger, 1992]. Although the Me is a seismically active boundary, the seismicity is present throughout the whole Gorda Plate, because the plate is undergoing anomalous deformation (implied also from magnetic isochrons, seafloor images) [Denlinger, 1992].

1.2.3 Cascadia Subduction Zone

The border between the North America Plate and the Juan de Fuca Plate is characterized by the megathrust Cascadia Subduction Zone (CSZ), forming a convergent margin from 40° to 51°. Convergence rates along the subduction zone are quite variable (see discussion for Nootka Fault) [Clowes et al, 1997].

While the Winona Block, situated in the North corner, may be underthrusting as an independent slab, the complex motion of the Explorer Plate results in different characteristics of a compression, uplift and seismicity between northern and southern Vancouver Island [Riddihough and Hyndman, 1991]. For the southern VI, the dip of the oceanic crust is about 3-4° seaward of the deformation front, and is increasing to 10° under the edge of the shelf and to 15° beneath the coast [Hyndman, 1995]. The geodetic data from this region shows the presence of an uplift (4mm/a) for the southwest coast decreasing inland, and shortening across the coastal region (10mm/a/100km) [Hyndman, 1995]. A locked subduction thrust fault is suggested from the uplift and shortening across the margin, and also from the seismicity along the margin (the existence of the deeper Waditi - Benioff seismicity in the subducting slab, and shallower earthquakes in the continental crust, but no thrust earthquakes on the subduction thrust fault) [Hyndman, 1995].

A slab beneath Washington and Oregon is characterized by a gentle dipping into depths of up to 40-60 km, and then by a more steep inclination to the depth 100-200 km beneath the volcanic arc. The dip increases from North to South along the CSZ [Riddihough and Hyndman, 1991]. The southern part of the Juan de Fuca Plate (off South Oregon and North California) is being deformed and fractured [Hyndman, 1995].

Fault name	Length [km]	Depth [km]	Slip [mm/a]	References length	depth	slip
Queen Charlotte	1120	22 13 - 21	55 50 - 60	[7]	[37] [52]	[37] [51]
Revere-Dellwood	140	10 5	55 40 -55	[10]	[36] [12] [67]	[37] [10]
Sovanco	125	10 5	42	[16]	[36] [12] [67]	[37]
Nootka	120 160	10 5	25	[42] [11] [34]	[36] [12] [67]	[51]
Blanco	350	10	56 58	[19]	[20]	[37] [19]
Mendocino	310	25	56		[14]	[37]

Table 1.1: Parameters of the faults: length of the active part of the fault (see Fig. 1.1), depth of the fault (seismogenic lithosphere), slip giving relative motion from global plate motion solution.

The CSZ was identified North of the Mendocino triple junction, but there is no identification for the southernmost part (few tens of kilometres) offshore Cape Mendocino, because of very complex faulted and folded sediments [Meriits, 1996].

All the mentioned faults are situated in the oceanic crust. South of the Mendocino triple junction the Pacific-North America plate boundary continues with the continental San Andreas Fault (SAF).

Each of the segments of the Pacific - Juan de Fuca - North America plate boundary described above has difficult and complex structure with a unique contribution to the overall tectonic description of the region.

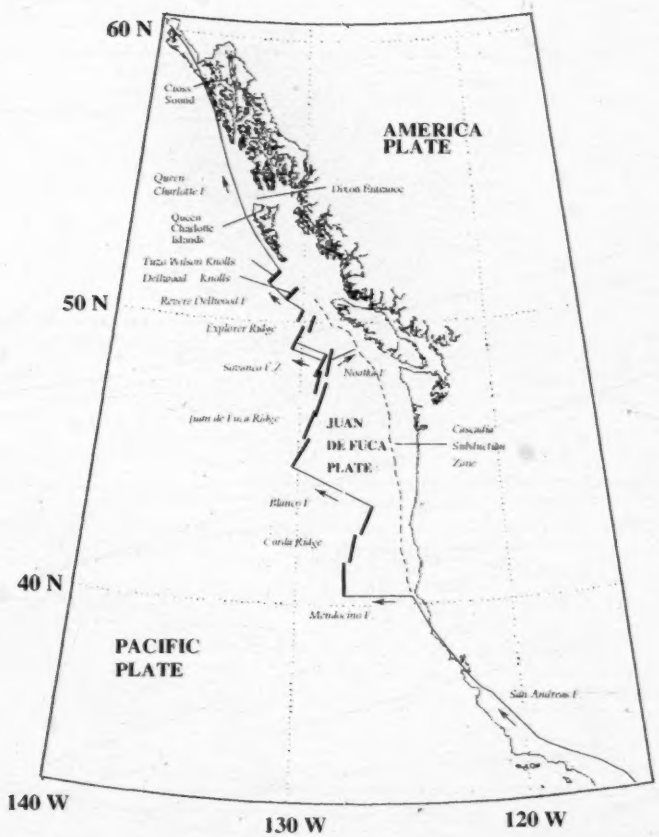

Figure 1.1: North East Pacific plate boundary (present situation); fault (line); ridge (bold line); arrow refers to the motion on the fault

Chapter 2

Overview of the Statistics

2.1 Mechanics of earthquakes

Aristotle pioneered a classification of Earthquakes according to the nature of the observed motion of the Earth. Also, in 132 AD Chinese philosopher Chang Heng devised an instrument to detect the direction of the first main impulse of the earthquake [Bullen, 1965]. In 1668 Hooke suggested that earthquakes are an elastic reaction to natural phenomena. Later followed Lyell (1868), who was aware of permanent changes of the Earth's surface caused by earthquakes. However, he believed that the immediate cause of the earthquakes were thermodynamic changes in the Earth [Scholz, 1990]. G. K. Gilbert was the first to make a connection between faulting and earthquakes (1872). He applied his theory only to the Great Basin, California, but it was soon shown to be valid elsewhere. However, a general validity of the connection between earthquakes and faulting instabilities was proven much later, after extensive global seismic networks were set [Scholz, 1990].

The present understanding of earthquake dynamics can be simplified as follows. A fault is a dynamic, elastic system. This system is slowly deformed, and this way a large amount of energy can accumulate at the location of the fault. After reaching a certain threshold, the stored energy is suddenly released in the form of an earthquake. Although it sounds simple, we do not understand fully the storage mechanism, and especially we are not able to predict the moment of reaching the threshold in advance.

2.1.1 Crack Propagation and Formation of Faults

Earthquakes are often described by kinematic models with suitably few parameters. Often used are the propagating dislocation model of Haskell (1964), and the Brune model (1970) which is rationalized in terms of dynamic properties of the source. These simple models provide no insight into the rupture process, so the use of dynamic models is needed [Scholz,

1990].

The dynamic models can provide us with a variety of information about earthquake dynamics. However, these results cannot be applied directly to real earthquakes, since the real ruptures obey much more complicated relations, and all the characteristics are likely to be heterogeneous on all spatial scales [Scholz, 1990]. We are therefore limited to general characteristics only.

As early as in 1776 Coulomb postulated that a brittle material, under stress, fractures along a plane of greatest tangential stress. In 1905 Anderson suggested that the fracture starts when the stress difference exceeds a certain threshold. Even later studies suggest that a combination of Coulomb and Anderson theories describes rupture formation well [Bullen, 1965]. However, there is a major class of faults not readily described by Anderson theory – low-angle overthrusts. These are very shallow faults upon which thin sheets of rock were transported horizontally. They have different orientation than Anderson theory predicts. Hubbert and Rubey hypothesized that under certain conditions the pore pressure can greatly exceed the hydrostatic. This offers a solution for this class of faults [Scholz, 1990]. Although Anderson theory provides good phenomenological understanding, it has problems with the explanation of fault growth, since it does not allow propagation of cracks within their own planes [Scholz, 1990].

Faults appear to have a fractal structure [Scholz and Aviles, 1986 and Scholz, 1990]. Based on this idea, Power, Tullis and Week (1988) developed a model of wear of fractal surfaces. It shows that the surfaces are constantly running in, because the steady state smoothness is never reached [Scholz, 1990]. Macroscopic scaling relationships show that the fault grows progressively in lateral extent and thickness as slip accumulates. At the same time deformation increases within the fault zone, leading to intensification of strain and associated structures within the fault zone. This together causes overall topographical smoothing of the fault zone [Scholz, 1990].

2.1.2 Earthquake Phenomenology

Most of the information that is available about earthquakes comes from the study of their elastic radiation. This requires a large number of observations and their careful analysis.

One of the most important pieces of information about an earthquake is its strength, which can be measured for instance in terms of magnitude or seismic moment. A detailed treatment of different magnitudes and moments and of the relationships between them is given in the next section.

Generally, major earthquakes happen without warning. However, some of the major earthquakes are preceded by smaller earthquakes, called foreshocks. It appears that the occurrence of the foreshocks is limited to certain seismic zones, and only a relatively small fraction of earthquakes [Bullen, 1965]. Often, earthquakes occur as a series within a short interval, with the same epicenter. The usual circumstance is a major earthquake followed by a series of smaller earthquakes called aftershocks. In some cases multiple major earthquakes can occur, but this is a very rare situation [Bullen, 1965].

2.2 Qualification and Quantification of Earthquakes

Most earthquakes are a result of lithospheric plate motion, and consequently most earthquakes take place along the plate boundaries, formed generally by faults and ridges. Different types of faults, and their various combinations are observed in the real Earth. For the three fundamental fault types (see Fig 2.1) various names were adopted [Bath, 1979].

The fault in Figure 2.1b is refered to as strike-slip fault, trancurren fault, lateral fault, tear fault, or wrench fault. This fault can be called sinistral (left-handed). For the opposite slip direction (marked by arrow), the fault is called dextral (right-handed). The angle of dip α is often near 90°. The second fault type (Fig. 2.1c) is called a normal fault, dip-slip fault, normal-slip fault, tensional fault, or gravity fault. Generally the angle of dip α is between 45° and 90°. For the last fundamental fault type (Fig. 2.1d) the adopted names, are a thrust fault, a dip-slip fault, a reverse-slip fault, reverse fault or a compressional fault. Often the angle of the dip is between 0 and 45° [Bath, 1979].

2.2.1 Fault-Plane Solution

The type of earthquake, and also the geometry of the fault plane, can be determined from the direction of motion (polarity) of the first seismic waves generated by the earthquake at seismograph stations located on the surface of the Earth. A plot of the polarity (positive = compressional = push, or negative = dilatation = pull) of the first motion from stations, in stereographic projection of lower hemisphere, gives a fault-plane solution (FPS) (see Fig. 2.2) [Fowler, 1990].

The fault-plane solution for a vertical strike-slip earthquakes (Fig. 2.2a) is formed by four quadrants, separated by two orthogonal planes (nodal surfaces), one of them being the fault plane (the slip vector always lies in the fault plane), and the other being an auxiliary plane (planes are not distinguishable from the fault plane solution only).

For non-vertical strike-slip motion, the FPS still has four quadrants. The fault plane

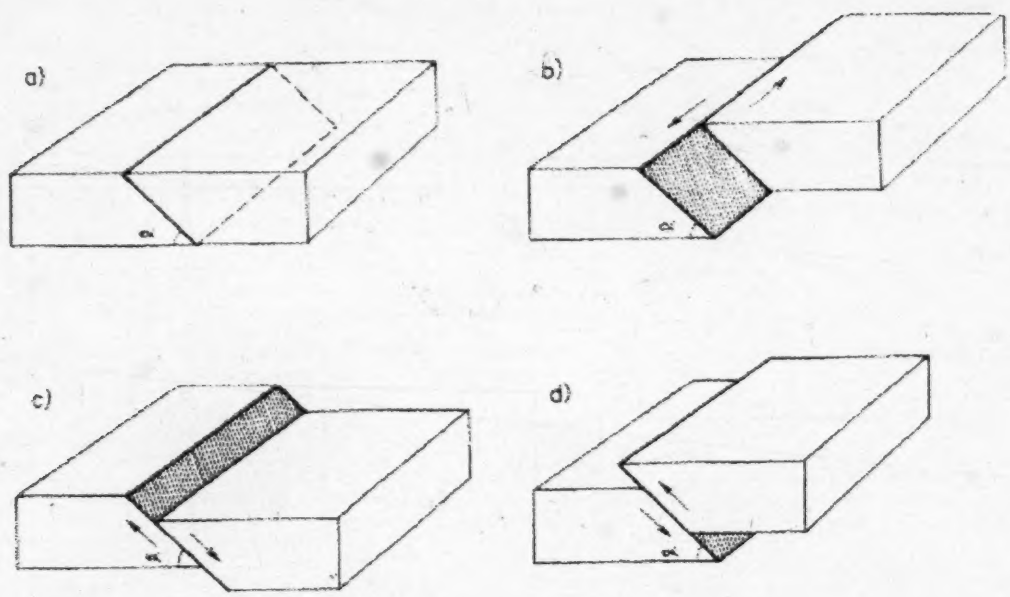

Figure 2.1: Fundamental types of fault motion. a) A block with a fault before any motion has taken place. For description of b), c), d) see text. (From Bath [1979])

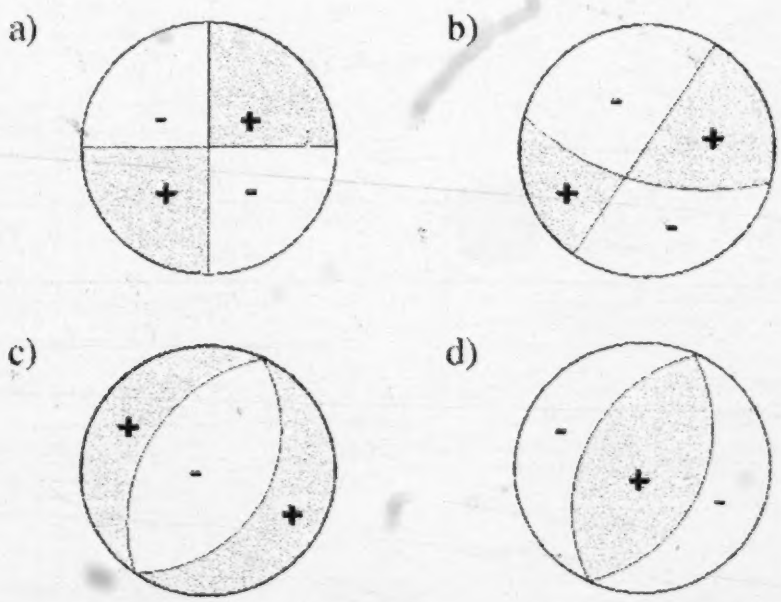

Figure 2.2: Fault-plane solution for a) vertical strike slip, b) nonvertical strike slip, c) normal and d) thrust fault. (From Fowler [1990])

and the auxiliary plane are plotted as orthogonal large circles, offset from the origin by the angle 90° - δ, where δ is their dip (Fig. 2.2b). The FPS-s for normal and thrusting faulting earthquakes (Fig. 2.2c,d) yield the unique strike of the nodal planes, but the dip of the fault plane is ambiguous. The first motion of the centre of the projection is always compressional, dilatational for the thrust, normal fault, respectively [Fowler, 1990]. Real earthquakes are often combinations of strike-slip motion with a normal or thrust component. The fault-plane solution does not provide any information about the size of an earthquake.

2.2.2 Earthquake Size

Over the last century many different approaches and scales were developed to describe size of the earthquakes. One of the most common is based on the use of magnitude scales. Historically the first one was the Richter magnitude scale, introduced in the 1930's by Californian seismologist C. F. Richter. He used two parameters to describe the size of earthquakes quantitatively: the distance from an earthquake to a seismograph, and the largest value of amplitude recorded on the seismogram. Richter magnitude (or local magnitude) was originally used to monitor the size of Southern California's shallow earthquakes, recorded by a Wood-Anderson torsion seismograph (with given constant of free period 0.8 sec, magnification 2800, damping 0.8) within 100 km [Bath, 1979]. Local magnitude, as originally devised in 1935 ($M_L = \log A - 2.48 + 2.76 \log D$, where A is the maximum trace amplitude, and D is the distance from the source [Lay and Wallace, 1995]), cannot be used to compare the size of earthquakes that took place in different regions. However, there are other stations (e.g. Alaska, Hawaii, Utah, Yellowstone [neic.usgs.gov, USGS tech. rep., 1999]) which use/used this type of magnitude (local magnitude) with local corrections. A general form for the local magnitude is:

$$M_L = \log A - \log A_0, \tag{2.1}$$

where A is the maximum trace amplitude in microns, and $\log A_0$ is a distance correction. Richter's idea to compare the size of earthquakes using magnitude scales was a great success. However, due to limitations of the local magnitude scales, several other magnitude scales were developed.

In 1945 Gutenberg created a magnitude scale based on Rayleigh surface waves with period 20 $\pm$ 2 sec. Later (1956), Gutenberg and Richter defined a body-wave magnitude scale from the amplitude of the compressional body P wave with period 4 to 5 sec [Bath, 1981]. Often used is also another type of scale, the duration magnitude scale, called also coda magnitude, which is obtained by fitting an exponential curve through the recorded

amplitude decay.

Many different variations of expressing the magnitude [Bath, 1981], usually taking into account specific local geographic conditions, exist. Generally, the formula for magnitude is in the form

$$M = \log(A/T) + f(D,h) + C_S + C_r, \tag{2.2}$$

where M is magnitude, A is ground amplitude in microns, T is wave period, f is a correction function for the epicentral distance D in degrees, and the earthquake focal depth h in km, C_S is a station correction for the special conditions at the position of the station (local structure, etc.), and C_r is a regional correction, different for different earthquake areas, and depending on the earthquake mechanism, and the wave propagation [Bath, 1979]. There are several empirical relations which relate different magnitude scales.

Limitations of the magnitude scales, such as frequency range, type of seismic signal, and most of all saturation (magnitude saturates when the value of the magnitude does not grow from a certain level, even though the released energy does) have led to the introduction of a different approach to the earthquake size measurements – the seismic moment M_{0ij}. This quantity is physically more meaningful, and does not have an upper limit. It is defined as the second rank tensor

$$M_{0ij} = \mu\Big(\bar{\Delta u_i} n_j + \bar{\Delta u_j} n_i\Big) A, \tag{2.3}$$

where $\bar{\Delta u_i}$ is the mean slip vector averaged over the fault area A with the unit normal vector n_j, and μ is the shear modulus. The scalar value of the seismic moment is $M_0 = \mu \bar{\Delta u} A$. Two directions given by the seismic moment tensor define the slip and fault orientation (fault plane solution). Thus the seismic moment tensor describes the orientation of the fault, direction of the fault motion, and the size of the earthquake [Scholz, 1990].

Magnitude scales, although improper for large earthquakes, have been widely used for many years because of their availability. Therefore, there have been efforts to correlate magnitudes to seismic moment and the moment magnitude. Hanks and Kanamori [1979] conclude that the magnitude M vs. seismic moment M_0 (scalar value) relation

$$M = 2/3 \log M_0 - 10.7 \tag{2.4}$$

is uniformly valid for

$$\begin{aligned} 3 \leq \quad & M_L \quad \leq 7, \\ 5 \leq \quad & M_S \quad \leq 7.5, \\ & M_w \geq 7.5, \end{aligned}$$

where M_L is local magnitude, M_S is surface wave magnitude, and M_w is moment magnitude [Hanks and Kanamori, 1979]. Numerous other correlating relations exist (see e.g. Okal and Romanowicz, 1994), with regard to the regional size or other limitations.

An alternative way of measuring earthquake size is by its energy release. Theoretically, the calculation of the radiated energy of the ruptured fault requires an integration of the energy flux over all the generated frequencies, over both, time, and space. At present, the seismic energies are calculated on a routine basis. Worldwide deployment of modern digital seismographs yields fast and explicit estimates for all large earthquakes [neic.usgs.gov]. The relation between seismic energy E_S and seismic moment M_0 is $E_S \approx \frac{1}{2}\frac{\sigma}{\mu}M_0$, where σ is the stress drop and μ is the shear modulus [Scholz, 1990].

Earthquakes can also be quantified by their intensity. Intensity is determined by the effects the earthquake have on people, human structures, and natural environment. It measures the strength of shaking at a certain location. Therefore the regional conditions significantly influence local intensity.

2.3 Scaling Relations

Stress drop may be considered to be one of the most fundamental scaling parameters. This is linearly related to dynamic characteristics of rupture (e.g. slip, velocity, or acceleration). Practically, it is difficult to determine the exact stress drop due to the heterogeneous distribution of stress drop on the fault, spatial and temporal determination of the slip distribution, high model dependence, etc., therefore the reported values differ [Scholz, 1990]. Although there is considerable variation in the observed stress drop value of earthquakes, the only systematic effect that has been found is between intraplate and interplate earthquakes [Scholz, 1990]. Observations of both large and small earthquakes indicate that stress drop is approximately constant and independent of earthquake size for individual faults [Scholz, 1990].

2.3.1 Gutenberg - Richter Scaling Relation

The most widely used scaling relationship is the empirical Gutenberg-Richter (GR) or Ishimoto-Aida magnitude frequency relation

$$\log N(m) = a - bm, \tag{2.5}$$

where N is the cumulative number of the earthquakes with magnitude larger or equal to m ($\log x$ is used for the decadic logarithm, $\ln x$ is used for the natural logarithm), a is a

parameter that is a function of the level of the regional seismic activity, b (which gives the negative slope of the GR relation) is an important parameter, characterizing the seismicity of the region. There are numerous studies of spatial and temporal variations of seismicity in various regions of the world. This causes rather large uncertainities in b, although some studies have proposed that b does not differ significantly from the universal value (discussed below).

Laboratory experiments have shown that b-value primarily depends on stress (decreasing b-value is related to the increase in stress). Scholz [1968] suggests a possible physical explanation for this dependence. Small earthquakes occur predominantly on pre-existing cracks as a result of the low stress, whereas the existence of larger earthquakes is a result of the increasing stress generated on new cracks. The energy released between a few faults yields low b-values, but between numerous small faults it yields larger b-values [Scholz, 1968].

There are quite a few studies dealing with the variations of the b-value with the regional state of stress [Wiemer and Wyss, 1997, Hamdache et. al. 1998, Sobiesiak, 2000, Sylvander, 1999, Qin et al, 1999, Frankel, 1991]. Wiemer and Wyss [1997] analyzed b-values from the perspective of asperities (small discrete contact surfaces of finite strength). They proposed that asperities along a fault zone may be mapped by anomalously low b-value, based on data from the San Andreas region. A similar study, for different regions, was done by Sobiesiak [2000] and Sylvander [1999]). They also showed that the b-value decreases as a function of depth from the high quality data sets. b-value vs. depth dependence was also studied by Frohlich and Davis [1993], Kagan [1999], Okal and Kirby [1995]. The variations of the b-value are also connected with different tectonic features. Frohlich and Davis [1993] conclude that b-values for thrust and strike slip faulting mechanisms are significantly less than b for normal earthquakes, except for the Tonga – Fiji region where earthquakes, deep in the subducting slab, shows b larger than elsewhere in the world. The same conclusion was obtained by Okal and Kirby [1995].

There is a wide range of observed b-values for different regions as well [Frohlich and Davis, 1993; Okal and Romanowicz, 1994; Hamdache et. al., 1998; Qin, 1999 and others]. Frohlich and Davis [1993] suggest that for different regions b is almost never less than 0.5, and almost never greater than 2.0, but Kagan [1999] states that "b-value variations are not caused by regional tectonics or physical factors, and regional variations of the b-values are largely artifacts of systematic effects." The b-value has also been studied in the context of material properties, degree of fracturing, time (used to estimate expected reccurrence of earthquakes), pore-fluid pressure, etc. [Utsu, 1999].

With respect to regional and temporal variations, b-values can be significantly affected by: properties of the magnitude scale used, magnitude range of the data, their completeness, method of determination, insufficient knowledge of the Earth's structure, non-uniform distribution of seismic stations, and others [Utsu, 1999; Kagan, 1999].

2.3.2 The Deviations from GR

While the original GR relation gives a straight line dependence between the logarithm of the cumulative number, and the magnitude, the observed data exhibit deviations from this straight line for large, as well as for very small earthquakes (see definition of large and small earthquakes is in section 2.3.3).

The deviation from the GR relation for the very small earthquakes, unlike for the moderate (small), or the large ones, is not frequently discussed. In the past it was thought that this deviation is caused by the incompleteness of the data. But this deviation has also been observed for regions with very good seismic station coverage, and for the data over the detection limit. A possible explanation for this feature is provided by the analytical stochastic model [Heimpel, 1996; Heimpel and Malin, 1998], characterized by asperity fault. The results of this model are in very good agreement with the size-frequency distribution of the data from the Parkfield fault segment from about magnitude zero, which is the detection limit for this region.

More attention is given to the deviations for the large earthquakes which can have either convex, or concave character. A wide range of different modifications of the GR model have been proposed, trying to characterize deviations from the observed data. According to Utsu [1999], there are four basic groups for the description of the convex type distributions. These groups used polynomial, exponential, logarithmic, or the combination of logarithmic and exponential functions. Only a few expressions for the concave type distributions were proposed, and they were based mostly on combining GR equations (e.g. $N = e^{a_1 - b_1 m} + e^{a_2 - b_2 m}$). Except for these, there are many complicated equations using the likelihood functions, proposed in seismology papers [Utsu, 1999]. Next we will briefly mention some specific scaling models, and views on this problem.

In the previous literature there has been discussion within the seismological community about the accuracy of the L and W models. One group, represented by Pacheco, Scholz, and others [Scholz, 1997], proposed an elastic L model in which the seismic slip scales with the length of the rupture L (which implies that stress drop is constant for all L), and is based on the fact that the group of large and the group of small earthquakes scale differently.

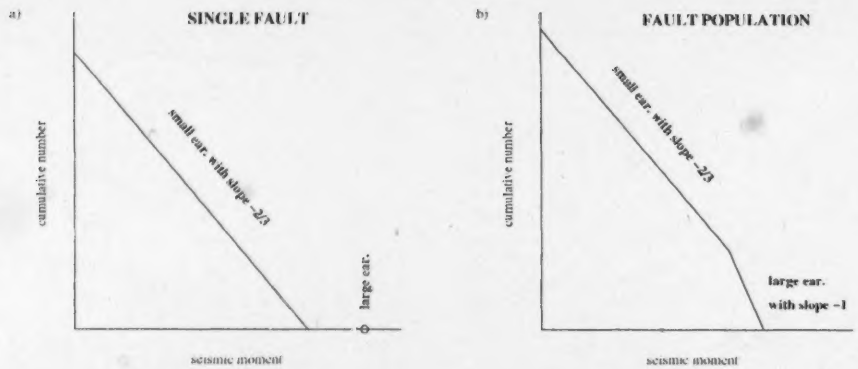

Figure 2.3: Illustration of cumulative size distribution of earthquakes for a) a single fault or plate boundary segment and b) a large region containing many faults or plate boundary segments. (From Scholz [1997])

The other group, connected to Rundle's idea [1989], uses the principle of scale invariance. They proposed the crack (dislocation) model, which suggest that the slip scales with the smallest dimension of the fault – the down dip width W_0 (which is the vertical thickness of the seismogenic layer). The W model implies that stress drop scales with L for large earthquakes [Rundle, 1989; Romanowicz and Rundle, 1993]. In terms of moment-frequency distributions, the L model propose $M_0 \propto L^3$ (where M_0 is the scalar seismic moment), for smaller earthquakes. The large earthquakes scale according to $M_0 \propto W_0 L^2$. The scaling according to the W model is different for the large earthquakes. This model predicts a linear scaling with the rupture length. From the observations, a change in the distribution for small and large earthquakes typically appears at about magnitude 7.5 [Pacheco, 1992].

Yin and Rogers [1996] tried to resolve this problem. They proposed a theoretical model based on the elastic theory of dislocations, considering an elliptical rupture with nonuniform slip. They conclude that for small earthquakes ($L < W_0$) the mean slip scales linearly with the rupture width. For large earthquakes ($L > W_0$), when the rupture length is smaller than a cross-over length (which is a function of rupture width; the cross-over length is about 75 km for $W_0 = 15$ km. and 125 km for $W_0 = 25$ km), the mean slip scales nearly linearly with the rupture length. But when the rupture length is larger then the cross-over length, the mean slip approaches, asymptotically, a constant value, and scales approximately with the rupture width. Their conclusions suggest that the characteristic length is not the thickness of the seismogenic layer, but rather the cross-over length. These results also match up with the observational data.

Although the question of scaling is not completely resolved yet, the conclusion from all

the models is that the scaling relation does indeed change for large earthquakes.

The previous discussion was connected to the strike-slip mechanism of the earthquakes. A contrasting situation is described by Stock and Smith [2000]. They showed that, for dip-slip events, self-similarity does not break down, except for very large earthquakes. Furthermore, the scaling change for very large events has no statistical significance.

There is also a different point of view to the earthquake scaling relation [Wesnousky et al, 1983; Schwartz and Coppersmith, 1984; Wesnousky, 1994, 1999; Scholz, 1997; etc.]. These studies proposed that the moment-frequency distributions on the individual faults did not follow the modified GR behavior (which means that the distribution follows the power law of the GR relation for small earthquakes, with an exponential drop-off for large earthquakes) but rather the characteristic earthquake model (which proposes larger frequency of occurence for the events of specific, characteristic size). For example, Wesnousky [1994] examined the geological and instrumental data for the major strike-slip faults of southern California. He concluded a strong preference for characteristic earthquake model for single faults and modified GR behavior for the fault zone. Scholz [1997] proposed the theoretical explanation for a different behavior for single faults and fault populations. The behavior of single faults compared to fault populations is shown in Figure 2.3.

All of the ideas about scaling relations up to here were connected to the magnitude or the seismic moment. Wu [2000] used the broad-band radiated energy to study frequency-size distribution of earthquakes. He concludes that unlike the distribution of the seismic moment (magnitude), which shows a deviation from GR, the distribution of the broad-band radiated energy obeys a single power law (like the standard GR relation) for shallow earthquakes world-wide.

2.3.3 Fractal Approach to Scaling Relations

The GR size distribution ($N = \alpha 10^{-bm}, \alpha = 10^{a}$) is a typical power law for fractal sets (a fractal set is defined as $N_i = C/r_i^D$, where N_i is the number of objects with a characteristic linear dimension r_i, C is a constant of proportionality, and D is the fractal dimension, which is generally not an integer [Turcotte, 1997; Scholz, 1990]).

Turcotte [1997] stated that all zones of the tectonic deformation obey fractal statistics in a variety of ways, and that the fractal dimension D of regional or worldwide seismic activity is twice the b-value (b from the GR relation). This relation between b and D follows from the seismic moment scaling. As a reasonable working hypothesis yielding the fractal distributions of earthquakes, he proposed that there is a fractal distribution of faults,

and each fault has its own characteristic earthquake. However, this does not mean that the fractal dimension of the frequency-size distribution for a fault is the same as the one for earthquakes. Turcotte [1997] argued that there is a wide variety of different mechanisms which are responsible for the formation of faults, and not all fault or fault systems are expected to yield fractal distributions.

According to Scholz [1990], small earthquakes (self-similar events whose rupture dimensions are smaller than the width of the seismogenic layer), and the large earthquakes (also considered to be self-similar events that rupture the whole seismogenic layer, and subsequently propagate horizontally along the fault plane), obey different scaling relations. Because of this difference in scaling, these two groups of earthquakes are not similar to each other, so they belong to distinct fractal sets (the difference arises because the system contains a characteristic dimension W_0) [Scholz, 1997].

In recent years quite a few studies of self-organized criticality have arisen (a system is in the state of self-organized criticality if it is sustained near the critical point, where a natural length scale does not exist any longer, but fractal statistics is applicable [Turcotte, 1997]). Although Scholz [1991] has argued that the entire Earth's crust is in this state, the entire concept of the self-organized criticality is controversial [Turcotte, 1997].

As was briefly shown above, the topic of the earthquake frequency-size distributions has been intensively studied, and judging from the immense amount of literature on the subject, it is one of the most important topics in the physics of earthquakes, and in the estimation of the seismic hazard.

Chapter 3

Data Analysis

In this chapter we describe the data analysis and all the results and discussions implied by it. We provide basic information about the databases, then how we handle the data and finally we present the results and analysis.

3.1 Databases

As mentioned earlier, our focus was to analyze faults of the North East Pacific plate boundary, particularly the Queen Charlotte, Revere-Dellwood, Sovanco, Nootka, Blanco and Mendocino faults/fault systems.

Seismic data for oceanic faults on Canadian territory (QC, RD, So, No) was provided by the Pacific Geoscience Centre (PGC), Geological Survey of Canada, Sidney, British Columbia. This database provides information about more than eleven thousand events along the active plate margin of the West coast of Canada, with the first event dated on February 17, 1793. We analyzed the data up to August 31, 2001. The number of reported events per year increase with time, as the ability to monitor seismic activity grows (represented by an increase in the number of seismic stations and the sensitivity of the seismometers). Monitoring of the seismic activity, and consequently the database information is estimated to be reliable from the 1960's (Roy Hyndman, PGC, personal communication).

The current magnitude completeness levels for the West coast of Canada are as follows: West coast of Vancouver Island reported magnitude $M \geq 1.0$, offshore of Vancouver Island (West of the North America/Juan de Fuca Plate boundary) $M \geq 2.5$, Queen Charlotte Islands $M \geq 1.0$, Alaska Panhandle $M \geq 2.7 - 2.8$, Chugach/St. Elias Mountains $M \geq 2.0$, Gulf of Alaska $M \geq 2.7 - 2.8$ (Taimi Mulder, PGC, personal communication).

The database provides information about time (year, month, day, hour, minute, second), location (latitude and longitude), depth and magnitude. But not all reports include infor-

mation about depth and in fact there are only few (2303) events which do not have fixed depth value. The magnitude is also not available for some events, but all others (10779) are reported in local magnitude.

For the Blanco and Mendocino Fault Systems (West of the USA) we used the Advanced National Seismic System (ANSS), the former Council of the National Seismic System (CNSS) database, which compiles worldwide information about earthquakes from the beginning of the 20th century. Data for these faults, used in our work, cover time span from May 1961 to March 2002. Similar to the PGC database, the ANSS record provides time, location, depth, magnitude, type of magnitude, and additional information (such as the number of stations which recorded a particular event, and the network that provided the used information, as well as the ID number). The ANSS database provides mainly body wave magnitude (M_b) for the regions around Bl and mainly coda magnitudes (M_c) are reported for the Mendocino region.

3.2 Magnitude - Moment Conversion

The databases mentioned above provide only information about the magnitude of the earthquakes. Since the seismic moment is a physically more adequate quantity, our first step was to convert reported values of magnitude to scalar seismic moment M_0 (for definition see Chapter 2.2.2).

Hanks and Kanamori [1979] provide the formula between universal moment magnitude M_w, which does not saturate (for definition see Chapter 2.2.2) and scalar seismic moment M_0 (equation (2.4)).

The Geological Survey of Canada (http://www.pgc.nrcan.gc.ca/seismo/ MTS) provides regional moment tensor solutions for earthquakes in Western Canada for the last three years. Each of the solutions contains the value for scalar seismic moment and corresponding moment magnitude, which are calculated directly from the M_0 using the standard Hanks and Kanamori formula (John Ristau, PGC, personal communication). We used this information for the marine earthquakes on the studied faults, combined with local magnitude from the PGC database for corresponding events, to get the $M_w(M_L)$ relation. Over all, we used information from about 95 earthquakes. We assumed the linear relation between M_w and M_L:

$$M_w = a + bM_L. \tag{3.1}$$

We obtained the parameters a and b using the linear least squares method, specifically

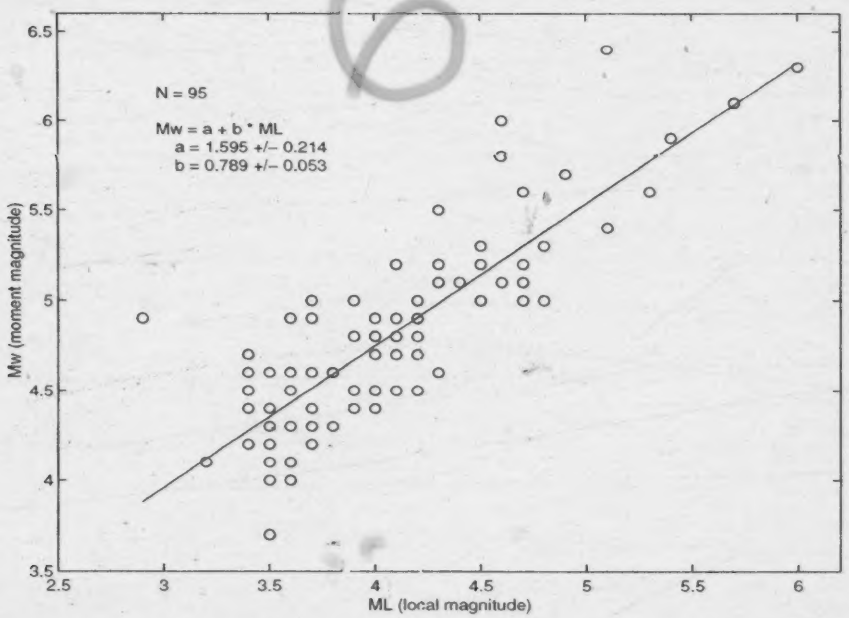

Figure 3.1: Corresponding moment magnitude (M_w) and local magnitude (M_L) for 95 earthquakes

$a = 1.595 \pm 0.214$, and $b = 0.789 \pm 0.053$ (see Figure 3.1). Then, combining the latter result with Equation (2.4), we obtained an expression for the scalar seismic moment in terms of local magnitude (M_L) in SI units:

$$M_0 = 10^{1.18275 M_L + 11.4878}. \tag{3.2}$$

Finally, applying derived $M_0(M_L)$ relation to all PGC data, we received database for scalar seismic moment.

Our intention was to use a similar approach for the Blanco and Mendocino data, but the only source for scalar seismic moment for this region was the Harvard Centroid Moment Tensor (CMT) database. This type of analysis requires a database that spans small or moderate to large earthquake sizes, and this database deals only with large earthquakes and runs only from January 1977, it does not provide a satisfactory amount of data to derive the $M_w(M_b)$ and $M_w(M_c)$ relations. Therefore we did not convert these magnitudes to the scalar moment.

3.3 Moment-frequency distributions

3.3.1 Selection of regions

Since our aim is to study the connection of the fault geometry with the size distributions for individual faults, first we separated data for the individual faults from the whole database. For this we used program `reg_ar_mo.f90`. This program extracts data for a chosen arbitrary four-sided region. It calculates the slope of the line between each two neighboring points and then, using the system of conditions, tests the location of earthquake to check whether it falls in the region.

Earthquake locations are subject to error, depending on the number of near-by stations. The errors for the offshore events, where there are no nearby stations, are usually about 10-20 km (John Ristau, PGC, personal communication). For this reason we chose several variations of area size corresponding to specific fault/fault system. We also separated different combinations of the fault regions (region of area of Revere-Dellwood, Sovanco and Nootka (*RDSoNo*), and Sovanco with Nootka area (*SoNo*)) for further investigation.

Next we calculated cumulative numbers and bin numbers for each chosen size of region. Cumulative number gives the number of the earthquakes with seismic moment larger or equal to certain value M_0 and bin number gives the number of the earthquakes larger or equal to M_0 and smaller than $M_0 + \delta$, where δ is the bin size of $10^{0.1}$. We use the program `mocb.m`, which calculates the cumulative and bin numbers for scalar seismic moments from 10^9 to 10^{24} Nm. First it calculates the reference moments, and then compares the moment for the earthquake from the database to the reference moments according to the criteria for the cumulative and binned numbers (described above), these numbers increase the value. Thus as a result were the files with three columns of seismic moments, cumulative and bin numbers for each size of studied regions. Finally, we plotted moment-frequency distributions for individual fault regions.

3.3.2 Curve fitting

Since we were interested in finding the characteristics associated with the change in statistics for large earthquakes, we used a modified GR distribution (see discussion in Chapter 2), as the fitting curve for the data. This modified GR distribution [Heimpel, 2003; Utsu,1999] obeys the power-law distribution of events sized up to a roll-off point, where cumulative number drops off exponentially, and has the form:

$$N = (s/\alpha)^{-\beta} exp[-(s/\lambda)^{\gamma}], \tag{3.3}$$

where N is the cumulative number, s is the size, and may be either seismic moment or rupture length, α corresponds to the GR a parameter ($\alpha = 10^a$, for $M_0 = 10^m$), which depends on the level of the regional seismic activity, β is the slope of the GR part of the distribution, λ is the roll-off point of s, which gives a measure of the characteristic size of the distribution and γ gives the steepness of the exponential roll-off.

We used the linear and nonlinear least squares method to obtain parameters α, β, γ, λ of fitting curve (modified GR distribution) for each fault region. For this purpose we developed program `ls_non_bez.m`. First step in the program was to pick the linear part of the $N(M_0)$ dependence. Then parameters α, β and standard deviation $\delta\beta$ are calculated from this linear part, using the linear least squares method. For the equation $y = a + bx$:

$$a = \frac{\sum_i x_i^2 \sum_i y_i - \sum_i x_i \sum_i x_i y_i}{n\sum_i x_i^2 - \sum_i x_i \sum_i x_i}, \tag{3.4}$$

$$b = \frac{n\sum_i x_i y_i - \sum_i x_i \sum_i y_i}{n\sum_i x_i^2 - \sum_i x_i \sum_i x_i}, \tag{3.5}$$

$$\delta b = \left(\frac{n\sum_i [y_i - (a + bx_i)]^2}{(n-2)\left[n\sum_i x_i^2 - \left(\sum_i x_i\right)^2\right]} \right)^{1/2}, \tag{3.6}$$

[Kundracik, 1997], where n is the number of couples $[x_i, y_i]$, in our case x_i is the logarithm of the reference seismic moment and y_i is the logarithm of the cumulative number. Applying the least squares method for the whole curve $logN = \beta log\alpha - \beta logs - (1/ln10)(s/\lambda)^\gamma$, simplified as $y = a + bx - c10^{xd}$, we obtained for $c = (1/ln10)\lambda^{-\gamma}$ and $d = \gamma$ the equations :

$$\sum (y_i - a - bx_i) 10^{x_i d} + c \sum 10^{2x_i d} = 0, \tag{3.7}$$

$$\sum (y_i x_i - a x_i - b x_i^2) 10^{x_i d} + c \sum x_i 10^{2x_i d} = 0. \tag{3.8}$$

The solution of equations (3.7) and (3.8) yields λ, γ. To solve these equations, an initial guess for $\gamma(\gamma_0)$ is required. With this guess we obtain c from equation (3.8). Then, using known c, and increasing the size of γ_0, we find the interval for γ with the solution of equation (3.7). Next, applying bisection [Press et al, 1992] to equation (3.7), we find γ. Now this γ is in turn used as the initial guess, and the whole process is repeated until the required accuracy is reached. This way we obtained all required parameters. The results of the moment-frequency fittings are shown in the next section.

3.3.3 Results for moment distributions

In this chapter we briefly summarize the moment-frequency distributions and the parameters of the fitting curve for the chosen regions.

Figures 3.2 - 3.21 show the positions of earthquakes in chosen regions (pink dots among black dots representing all other earthquakes) with location parameters (latitude and longitude) for the edge points and the number of earthquakes (N) with magnitude ≥ 2.5 (top), and moment-frequency distributions with fitting curves for the cumulative distributions (bottom). The parameters of the fitting curves are summarized in Table 3.1.

For the Queen Charlotte fault system (which can be described as a quite narrow fault system with one dominant fault plane) we analyzed two different sizes of region (see Fig. 3.2, 3.3). These two regions are chosen for the entire length of the fault (including the Fairweather fault as a straight continuation of QC) and the first region includes a larger area. As can be seen from the figures, the statistics are very close, which implies very close/same values for parameters of the fitting curve, so they may be analyzed together. Moment-frequency distributions show a strong power-law for a large part of the distribution. However, for the large earthquakes, the statistics are characterized by the typical drop off. The β parameter, which represents the slope of the Gutenberg-Richter part of the distribution has a quite low value (~ 0.4). On the other hand, the steepness of the exponential roll-off, represented by the γ parameter has the largest value (~ 3.8) compared to all of the studied systems. The QC is very long, and the λ parameter has a large value as well. The characteristic size for QC is close to 1×10^{21} Nm.

Figures 3.4, 3.5, and 3.6 show the size distributions for the Revere-Dellwood fault system, which is predominantly characterized by one smooth line. The first analyzed region included the events in quite a large area around the fault plane and events from the Explorer Ridge area. The second and the third region do not include the Explorer Ridge events and differ in the size of the chosen region. But moment-frequency distributions for all three regions show very similar behavior. A strong power law is characteristic for small earthquakes. Distribution smoothly changes to exponential tail for the large events. Parameters of the fitting curve differ from the previous case (QC). Compared to other studied faults, the β parameter has the largest value (~ 0.6). But the γ parameter drops to the value of 1.40. Since the length of the RD is significantly shorter than QC (see Table 1.1), this implies a lower λ parameter. The average value of the λ parameters can be considered the characteristic moment 3.7×10^{19} Nm.

The third studied fault system is the Sovanco, which is geologically characterized as a wide zone (30-34 km of horizontal width [Davis and Currie, 1993]) consisting of short (5 km) fault planes and adjacent pieces of ridge. The first of three chosen sizes of regions (Fig. 3.7, 3.8, 3.9) includes the events in a quite large area around the fault system, while

the second region is for a smaller region between the Explorer Ridge and the Nootka fault system. The third region is a small area corresponding only to the geological boundary set by Davis and Currie [1993], which probably does not include all related events, since some shifts/mislocations are quite possible in this region. The first two moment distributions show very similar behavior, but the third distribution is slightly different. A strong power-law for small earthquakes continuously changes to an exponential tail in the cumulative statistics. This behavior is more significant for the first two regions. The third distribution which has much fewer analyzed events, could be described by a sudden drop of the power-law for the large earthquakes. The parameters of the fitting curve remain quite stable. The β parameter has typical value ~ 0.4, and the γ parameter is 1.4. The value of the λ is slightly lower than for the RD. Also the total length of the So is slightly lower. The second region is probably the best choice for So, and its characteristic size is 2.3×10^{19} Nm. Thus the value of the λ parameter implies that the Sovanco behaves like a single continuous fault, rather than a group of short separated, unconnected faults.

The object studied next was the Nootka fault system with left lateral movement. Its horizontal width is estimated to be 20 km and it contains numerous short faults in the main direction (see Chapter 1). The first region (Fig. 3.10) is for a large area including also the part under the Vancouver Island. The second region (Fig. 3.11) is closer to the boundary of the studied fault, and the third region (Fig. 3.12) does not include the part under the VI. All three cumulative size distributions show similar behavior, although the third one is probably missing the events characterized as predominantly left-lateral, with small subduction movement. Cumulative distributions for the No have the unique character. Small earthquakes might be characterized by the power-law distribution which very slowly continues to the exponential drop-off. This behavior implies a very low value ($\sim 0.6 - 1$) for the γ parameter. The β parameter is typical for the group (~ 0.5) and the value for λ places the No in the group of short faults, such as RD and So. The average value of the λ parameters for the three analyzed regions is 1.4×10^{19} Nm.

We also analyzed the combinations of the studied fault areas to understand the behavior of the whole system. We analyzed distributions for the $SoNo$ and the $RDSoNo$ regions. On the Figures 3.13 and 3.14 are analyzed distributions for the $SoNo$ area with different size. Both regions show a similar behavior, close to the analyzed Sovanco group. The $RDSoNo$ distribution (Fig. 3.15) can be also included to this family, though contribution of RD increase the value of β to 0.52. Distributions of combined areas mainly adopt the behavior of one particular fault, and other individual characteristics are suppressed.

Fault systems south of the Canadian border were not, due to lack of information (explanation in Chapter 3.2), analyzed more precisely (in the terms of fitting curve). While all Canadian offshore faults unambiguously show the modified GR behavior, the statistics for the Blanco and Mendocino are diametrally different. The cumulative distributions for the BL and Me show a strong characteristic behavior (for definitions see Chapter 2), indicated by the 'foot' on the cumulative distribution for the large events.

Figure 3.16 shows cumulative and bin magnitude-frequency distributions for the region around the entire Blanco fault. The Bl is the system of faults, which are according to Dziak [1991] separated by Cascadia Depression and show different behavior. From this reason we also analyzed these two parts separately. In Fig. 3.17 is the distribution for the northeastern part of the Bl, which shows power-law for the small events and one offset event. Second half of the Bl (southwestern part), with one dominant fault, has distribution on Figure 3.18, with characteristic behavior for the cumulative statistics. Two peaks in bin statistics (instead of typical one) might indicate also the importance of little adjacent fault on the very east of this segment.

The last analyzed feature was the Mendocino fault system. All chosen regions (Fig. 3.19, 3.20, 3.21), differing in the size of studied area, have very similar distributions. The cumulative statistics indicate the strong characteristic behavior. The bin statistics show besides the one traditional peak also the little adjacent bump, since Me is described as a complex of different geological features.

Each of the studied fault/fault system is very complex, with specific individual features, which have to be taken into account for all size distribution analysis.

Fault	M:	β_M	$\Delta\beta_M$	γ	λ_M [Nm]	β_{M_1}	β_{L_1}/β_{M_1}	L:	β_{L_1}	$\Delta\beta_{L_1}$	λ_L [m]
QC1		0.441	0.006	3.80	1.13e21	0.45	2.87	set11	1.29	0.02	9.72e5
						0.45	2.89	set12	1.30	0.02	4.98e5
						0.45	2.84	set21	1.28	0.01	6.52e5
						0.45	2.87	set22	1.29	0.02	4.87e5
QC2		0.400	0.005	3.80	1.04e21	0.40	2.93	set11	1.17	0.01	8.95e5
						0.41	2.88	set12	1.18	0.01	4.59e5
						0.41	2.83	set21	1.16	0.01	6.01e5
						0.41	2.88	set22	1.18	0.01	4.49e5
RD1		0.615	0.007	1.40	3.17e19	0.66	3.02	set a	1.99	0.04	1.10e5
						0.65	3.02	set b	1.96	0.03	5.66e4
RD2		0.574	0.010	1.40	3.96e19	0.68	3.01	set a	2.05	0.06	1.37e5
						0.64	3.03	set b	1.94	0.05	7.04 e4
RD3		0.564	0.010	1.40	3.91e19	0.66	3.03	set a	2.00	0.06	1.35e5
						0.63	3.02	set b	1.90	0.05	6.95 e4
So1		0.393	0.006	1.40	1.94e19	0.40	3.00	set a	1.20	0.02	6.77e4
						0.40	2.98	set b	1.19	0.02	3.51e4
So2		0.416	0.006	1.40	2.32e19	0.40	3.03	set a	1.21	0.02	8.07e4
						0.41	2.98	set b	1.22	0.02	4.18e4
So3		0.464	0.008	1.40	3.70e19	0.46	3.00	set a	1.38	0.04	1.28e5
						0.46	3.00	set b	1.38	0.03	6.58e4
No1		0.467	0.012	0.60	1.18e19	0.44	2.93	set a	1.29	0.03	4.17e4
						0.47	2.91	set b	1.37	0.04	2.19e4
No2		0.457	0.010	0.60	1.31e19	0.43	2.95	set a	1.27	0.03	4.61e4
						0.46	2.91	set b	1.34	0.04	2.41e4
No3		0.469	0.011	0.99	1.61e19	0.44	2.95	set a	1.30	0.03	5.64e4
						0.47	2.94	set b	1.38	0.04	2.94e4
SoNo1		0.452	0.006	1.40	2.44e19	0.40	3.00	set a	1.20	0.02	8.48e4
						0.43	2.93	set b	1.26	0.03	4.39e4
SoNo2		0.461	0.006	1.40	2.07e19	0.42	3.00	set a	1.26	0.03	7.21e4
						0.45	2.91	set b	1.31	0.03	3.74 e4
RDSoNo		0.524	0.006	1.40	2.33e19	0.52	2.96	set a	1.54	0.03	8.10e4
						0.54	2.94	set b	1.59	0.03	4.19e4

Table 3.1: Parameters for fitting curves: M refers to moment distributions, L refer to length distributions; for QC: set11 is for $W_0 = 20$km, $\sigma = 0.75$ MPa; set12 is for $W_0 = 20$km, $\sigma = 1.471$ MPa; set 21 is for $W_0 = 30$km, $\sigma = 0.75$ MPa; set22 is for $W_0 = 30$km, $\sigma = 1.009$MPa; all other faults have $W_0 = 5$km and set a is for $\sigma = 0.75$ MPa and set b is for $\sigma = 1.471$ MPa.

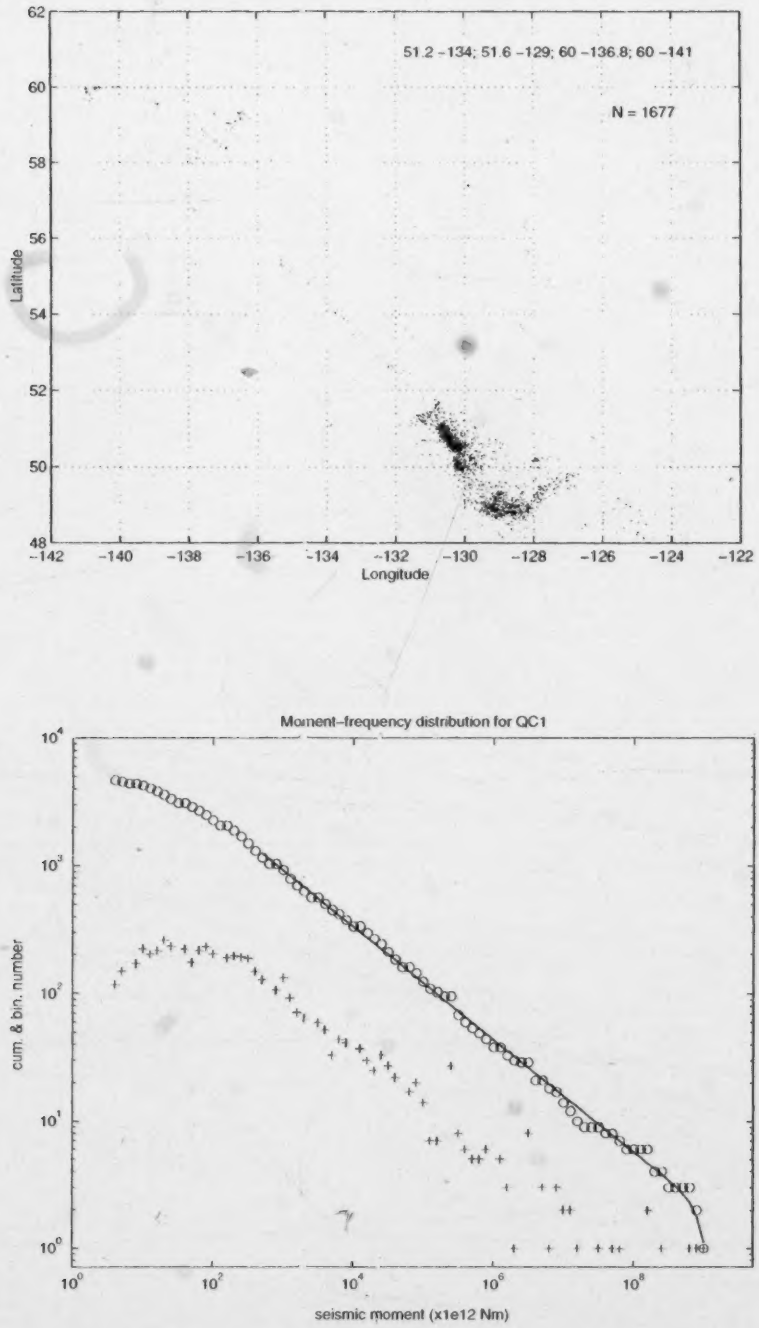

Figure 3.2: Top: pink - chosen region (from now on will be referred as $QC1$). Bottom: moment-frequency distribution with fitting curve (-) for cumulative dist. (o); bin dist. (+). For more details see text.

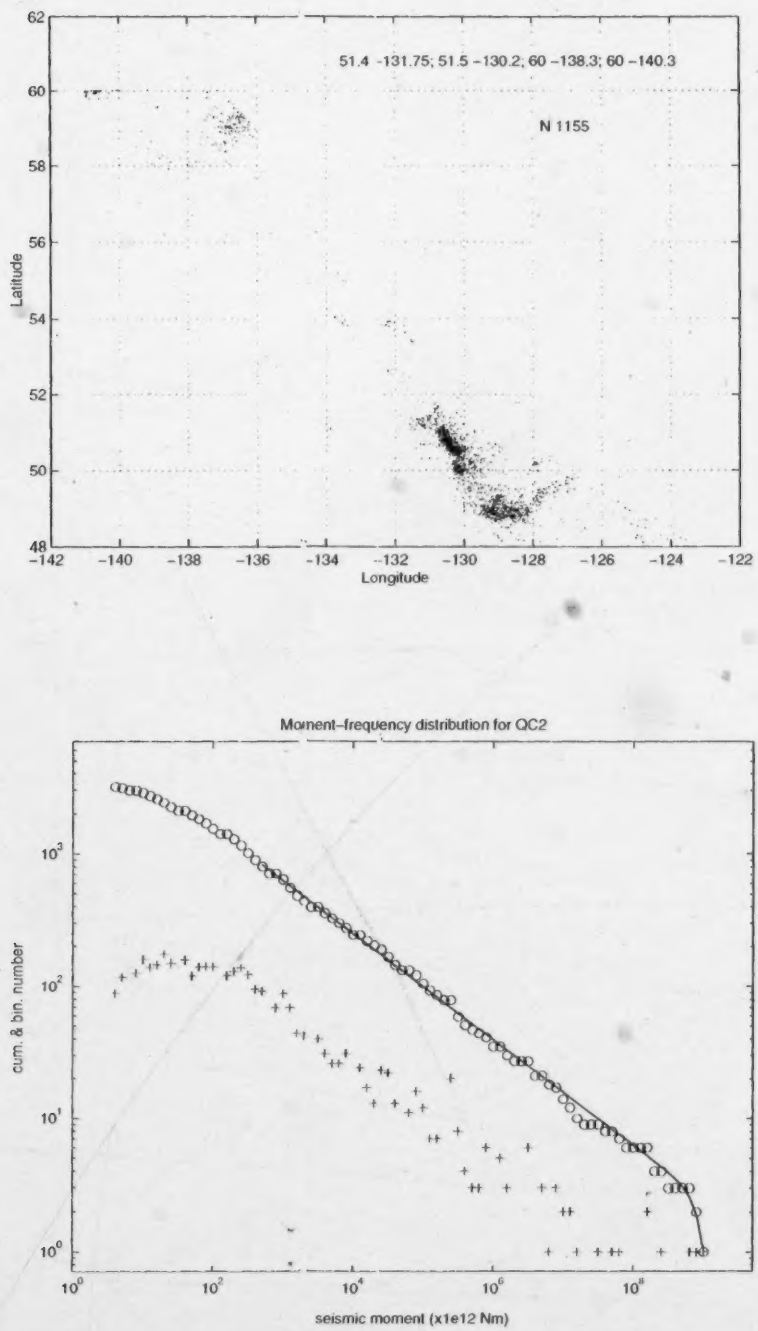

Figure 3.3: Top: pink - chosen region (from now on will be referred as $QC2$). Bottom: moment-frequency distribution with fitting curve (-) for cumulative dist. (o); bin dist. (+). For more details see text.

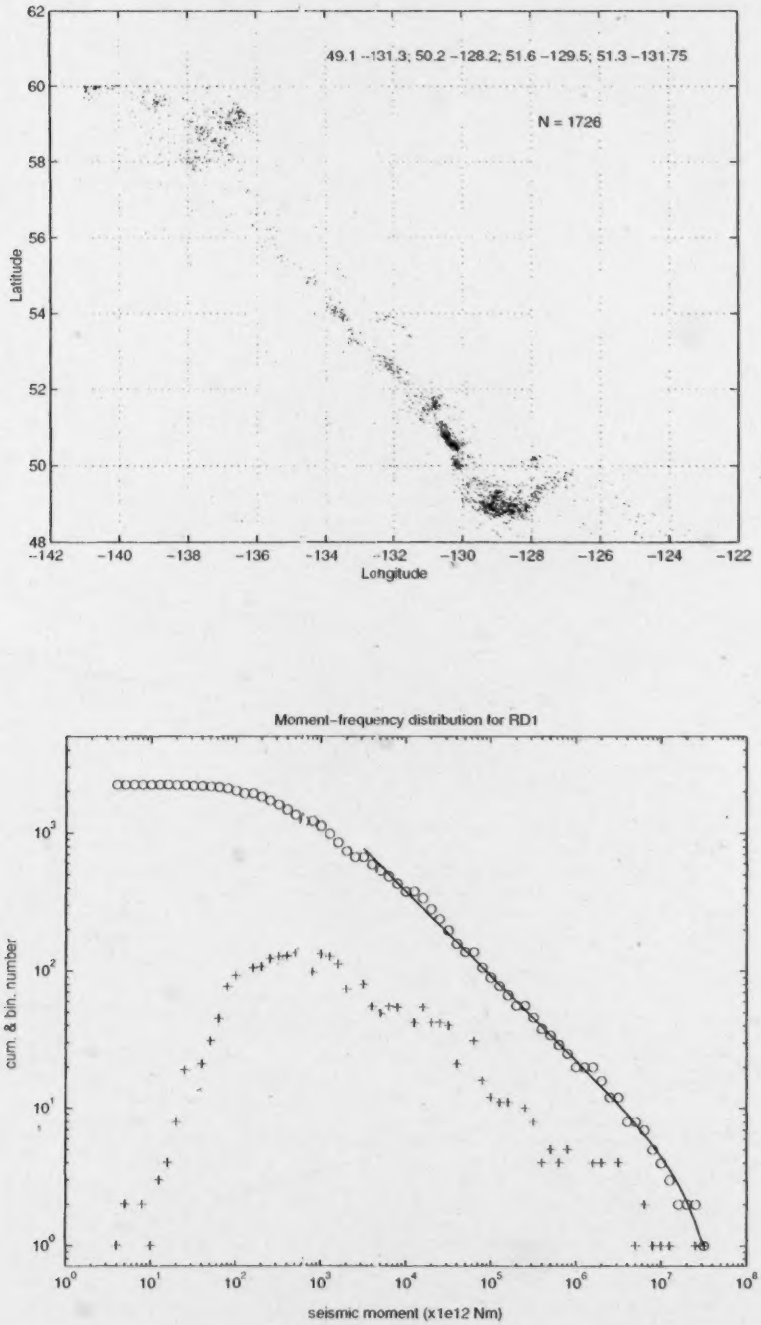

Figure 3.4: Top: pink - chosen region (from now on will be referred as $RD1$). Bottom: moment-frequency distribution with fitting curve (-) for cumulative dist. (o); bin dist. (+). For more details see text.

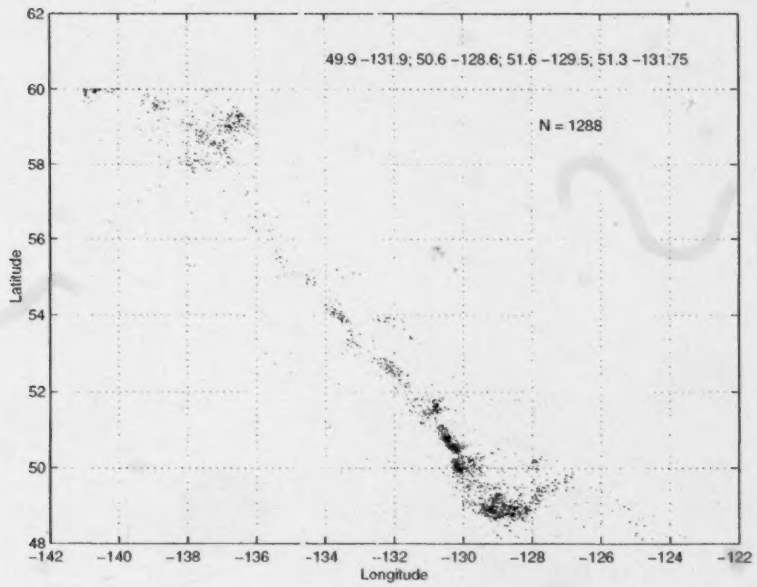

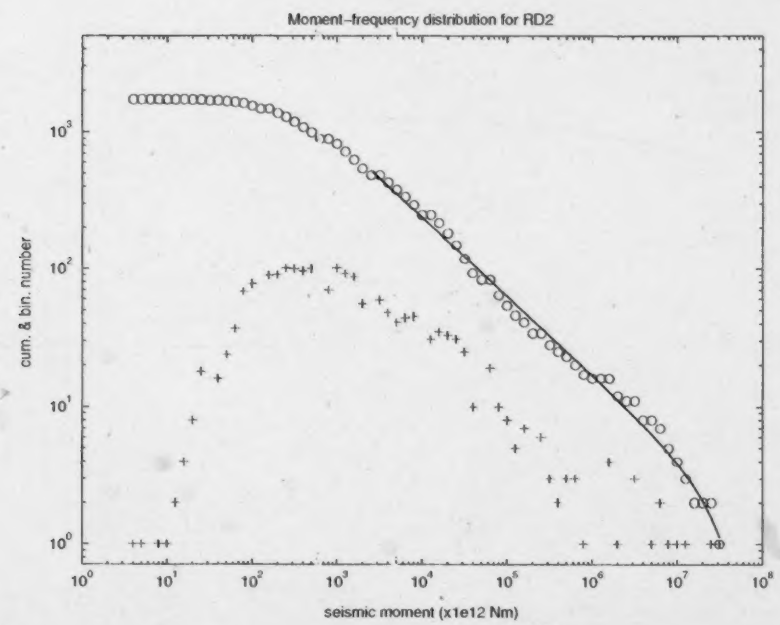

Figure 3.5: Top: pink - chosen region (from now on will be referred as *RD*2). Bottom: moment-frequency distribution with fitting curve (-) for cumulative dist. (o); bin dist. (+). For more details see text.

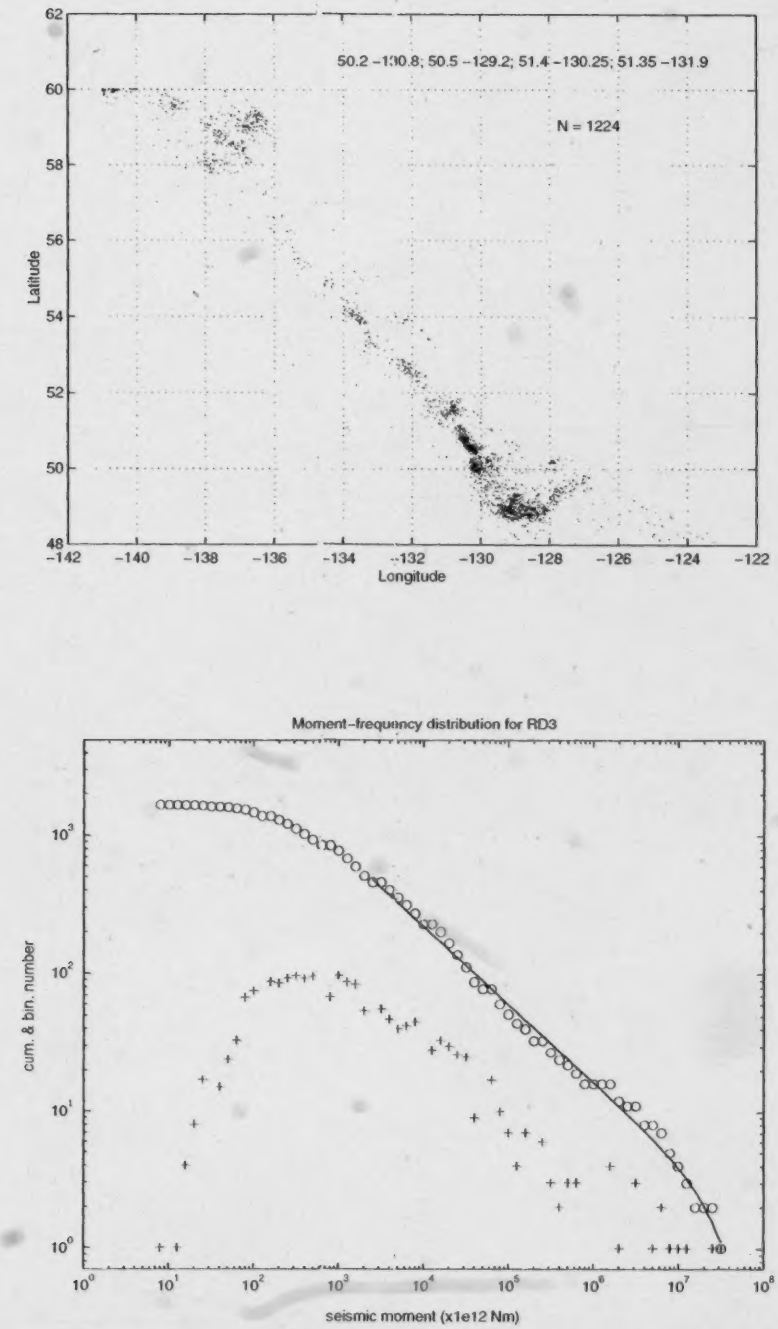

Figure 3.6: Top: pink - chosen region (from now on will be referred as *RD3*). Bottom: moment-frequency distribution with fitting curve (-) for cumulative dist. (o); bin dist. (+). For more details see text.

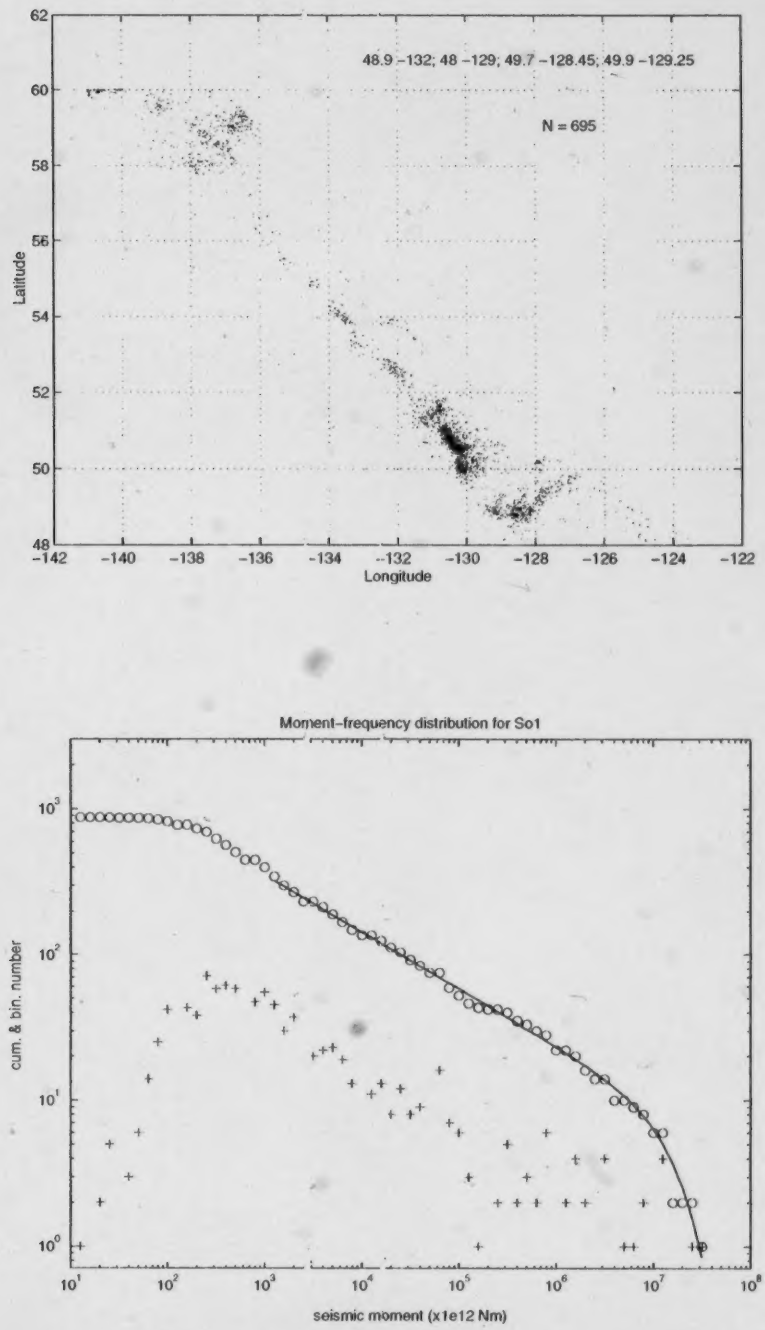

Figure 3.7: Top: pink - chosen region (from now on will be referred as *So*1). Bottom: moment-frequency distribution with fitting curve (-) for cumulative dist. (o); bin dist. (+). For more details see text

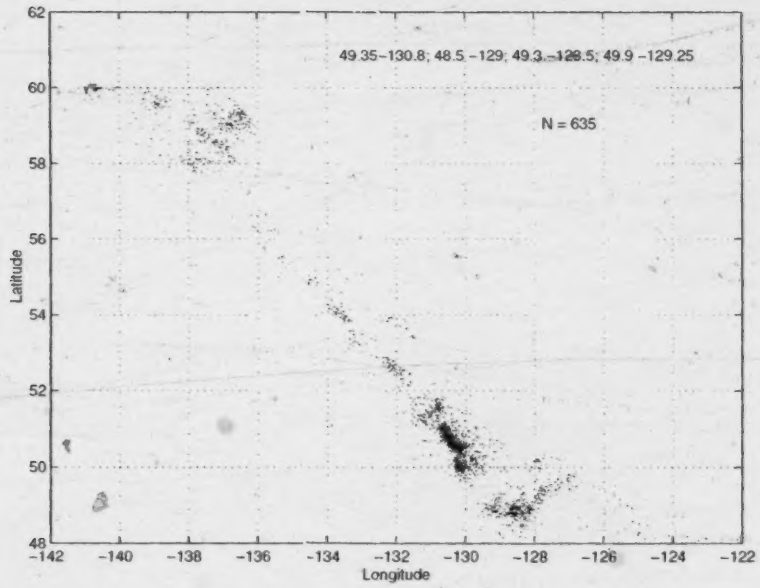

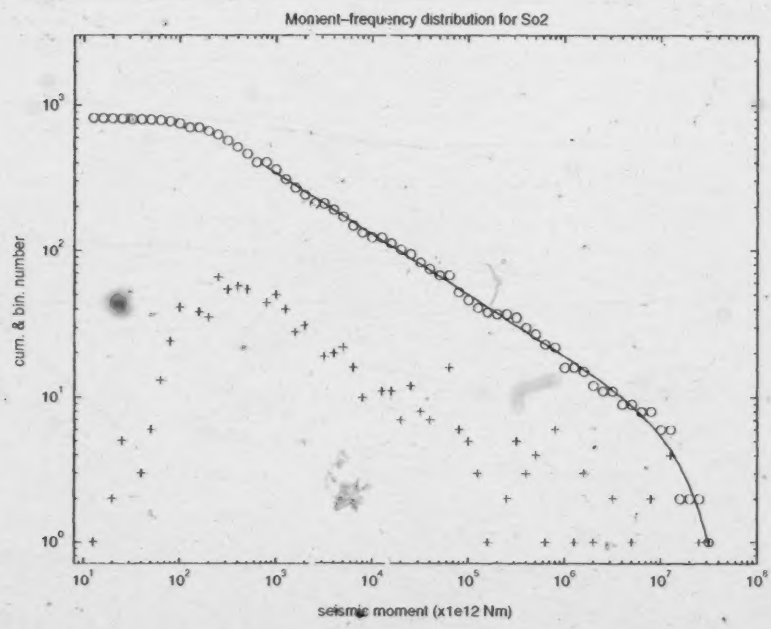

Figure 3.8: Top: pink - chosen region (from now on will be referred as $So2$). Bottom: moment-frequency distribution with fitting curve (-) for cumulative dist. (o); bin dist. (+). For more details see text

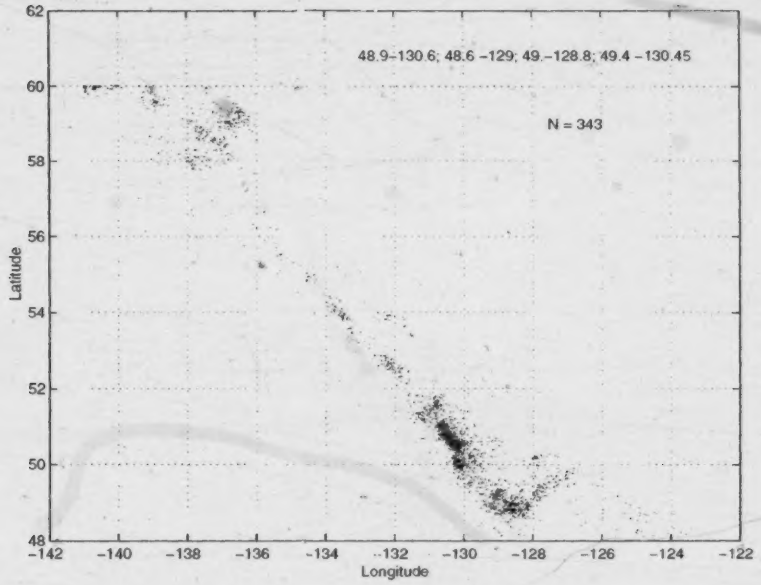

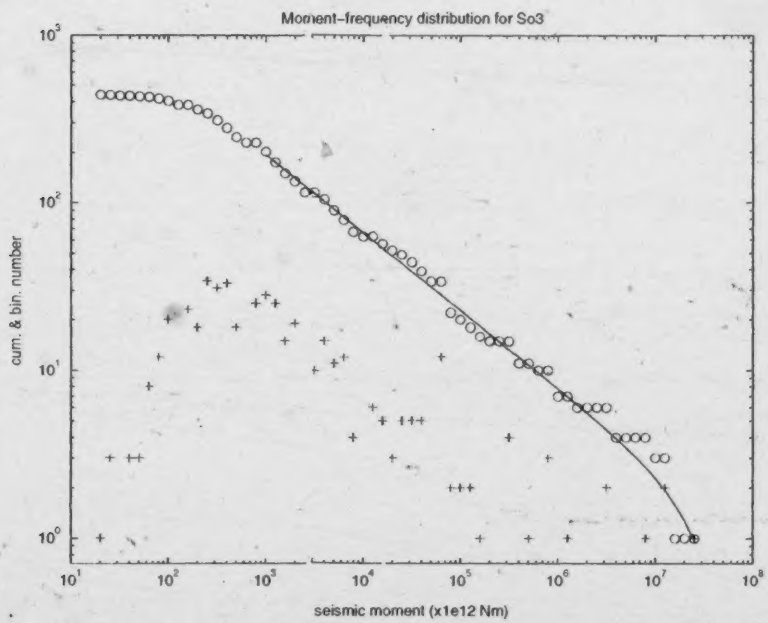

Figure 3.9: Top: pink - chosen region (from now on will be referred as *So3*). Bottom: moment-frequency distribution with fitting curve (-) for cumulative dist. (o); bin dist. (+). For more details see text.

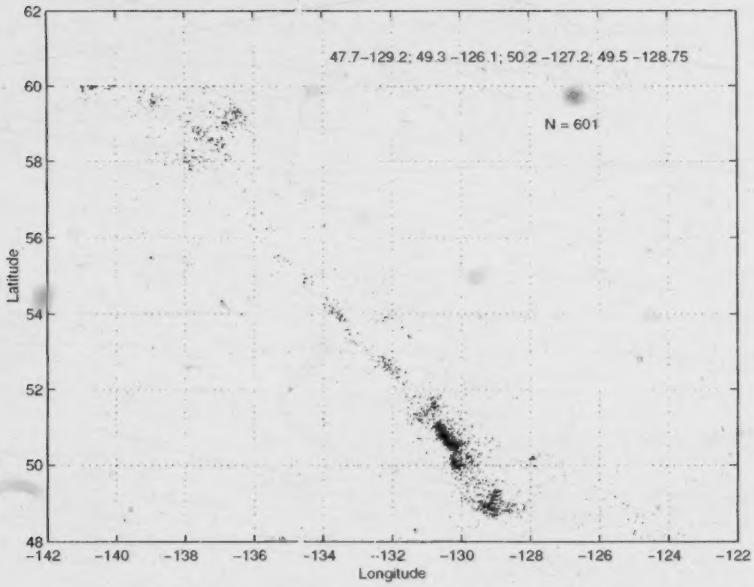

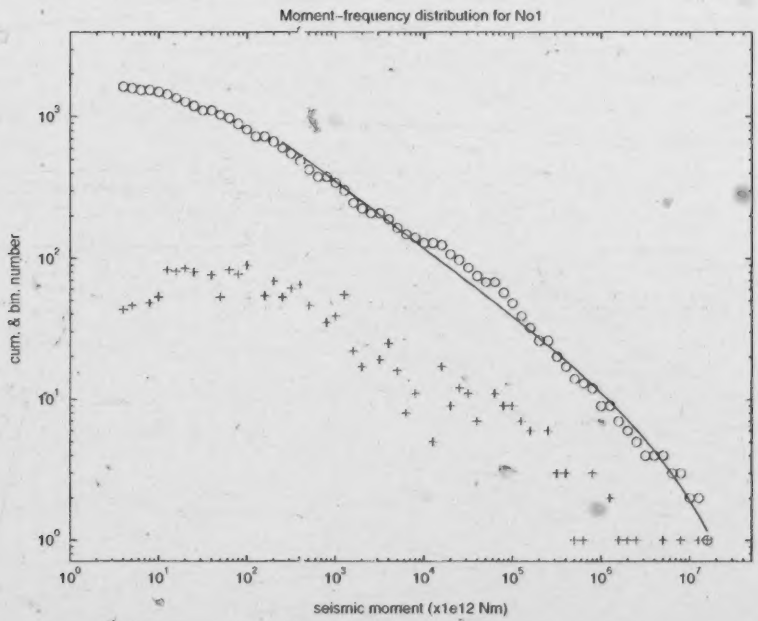

Figure 3.10: Top: pink - chosen region (from now on will be referred as *No*1). Bottom: moment-frequency distribution with fitting curve (-) for cumulative dist. (o); bin dist. (+). For more details see text.

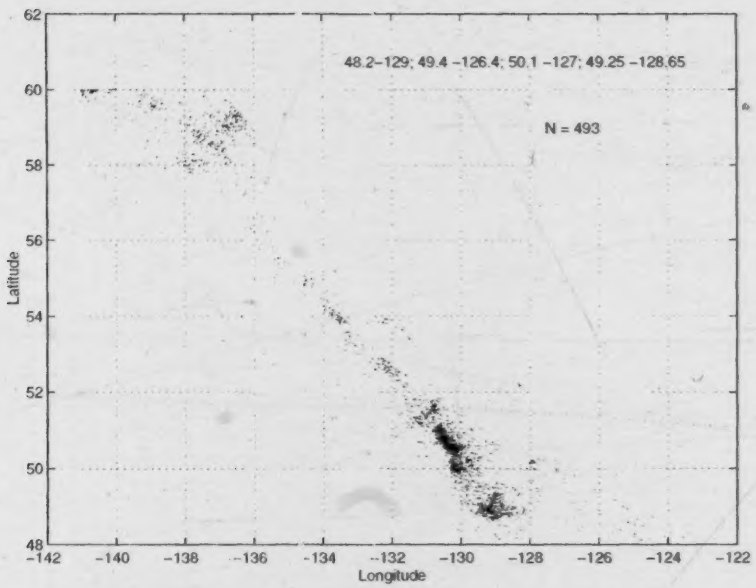

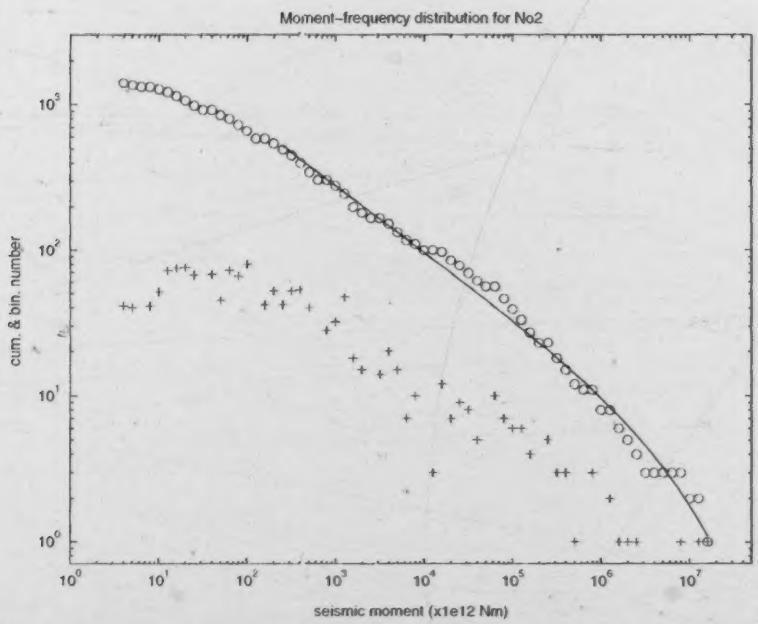

Figure 3.11: Top: pink - chosen region (from now on will be referred as $No2$). Bottom: moment-frequency distribution with fitting curve (-) for cumulative dist. (o); bin dist. (+). For more details see text.

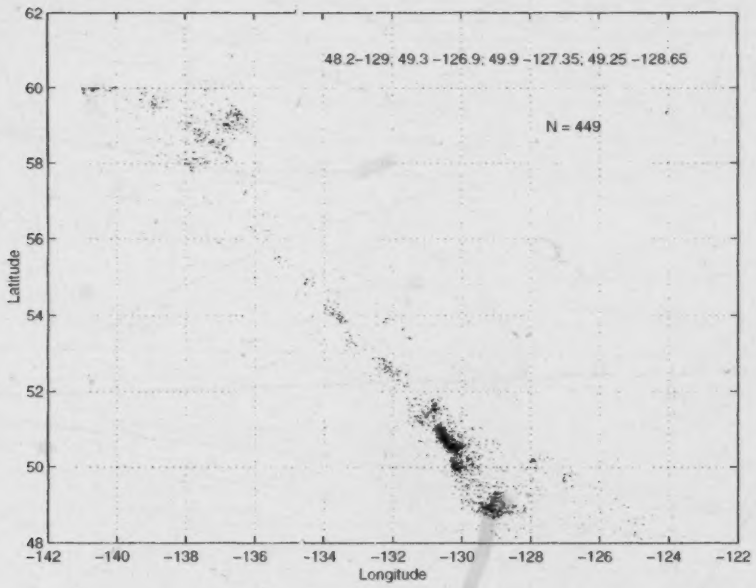

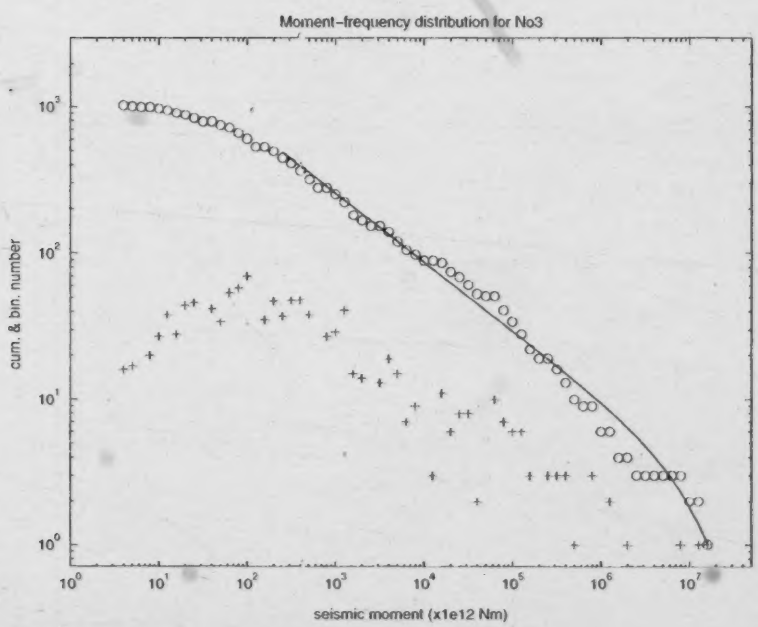

Figure 3.12: Top: pink - chosen region (from now on will be referred as *No3*). Bottom: moment-frequency distribution with fitting curve (-) for cumulative dist. (o); bin dist. (+). For more details see text.

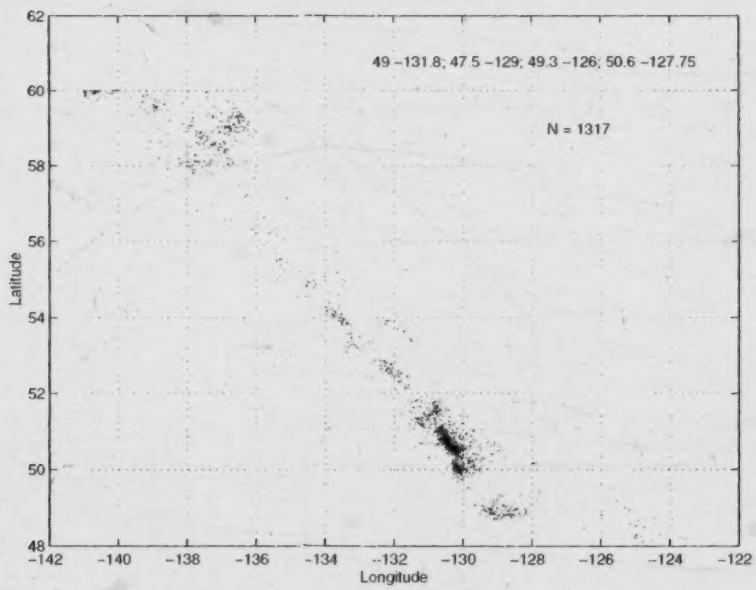

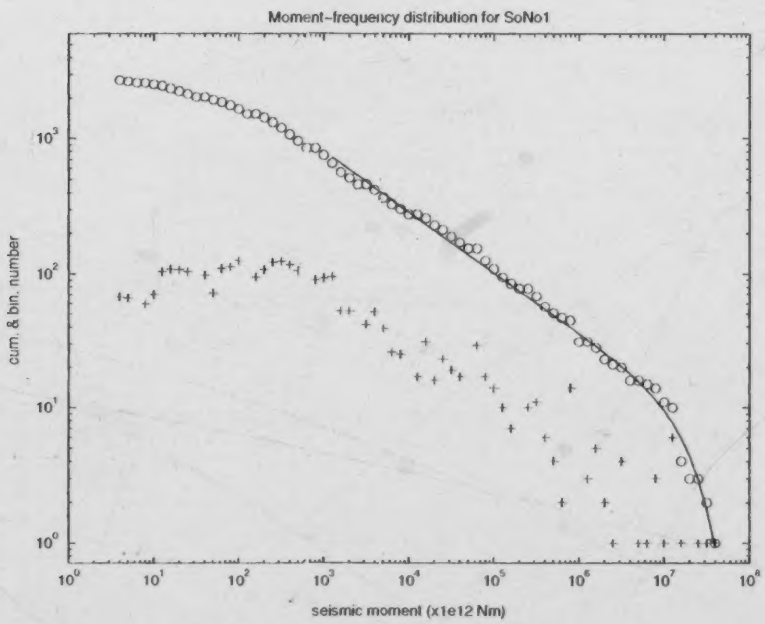

Figure 3.13: Top: pink - chosen region (from now on will be referred as *SoNo1*). Bottom: moment-frequency distribution with fitting curve (-) for cumulative dist. (o); bin dist. (+). For more details see text.

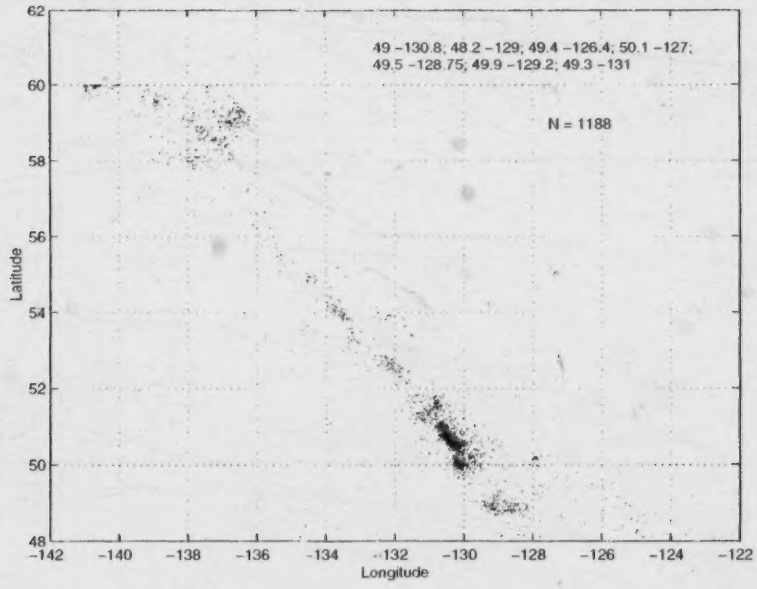

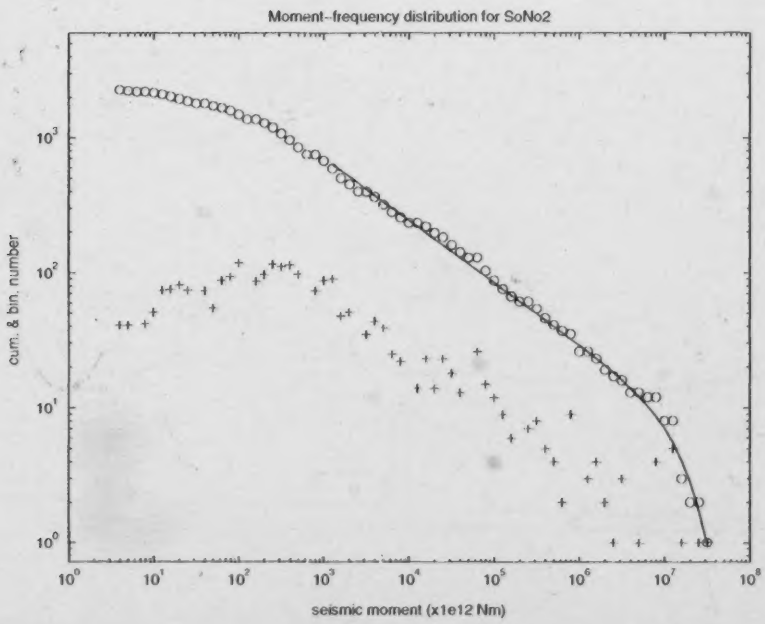

Figure 3.14: Top: pink - chosen region (from now on will be referred as *SoNo2*). Bottom: moment-frequency distribution with fitting curve (-) for cumulative dist. (o); bin dist. (+). For more details see text.

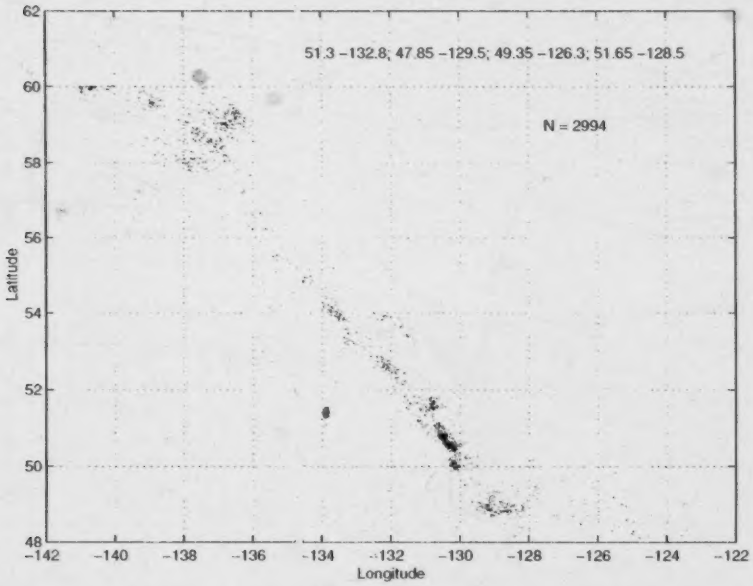

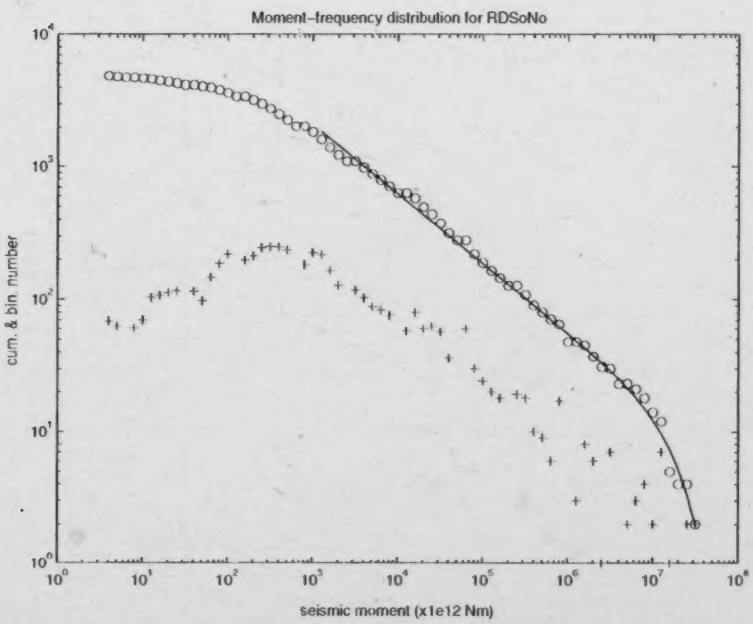

Figure 3.15: Top: pink - chosen region (from now on will be referred as *RDSoNo*). Bottom: moment-frequency distribution with fitting curve (-) for cumulative dist. (o); bin dist. (+). For more details see text.

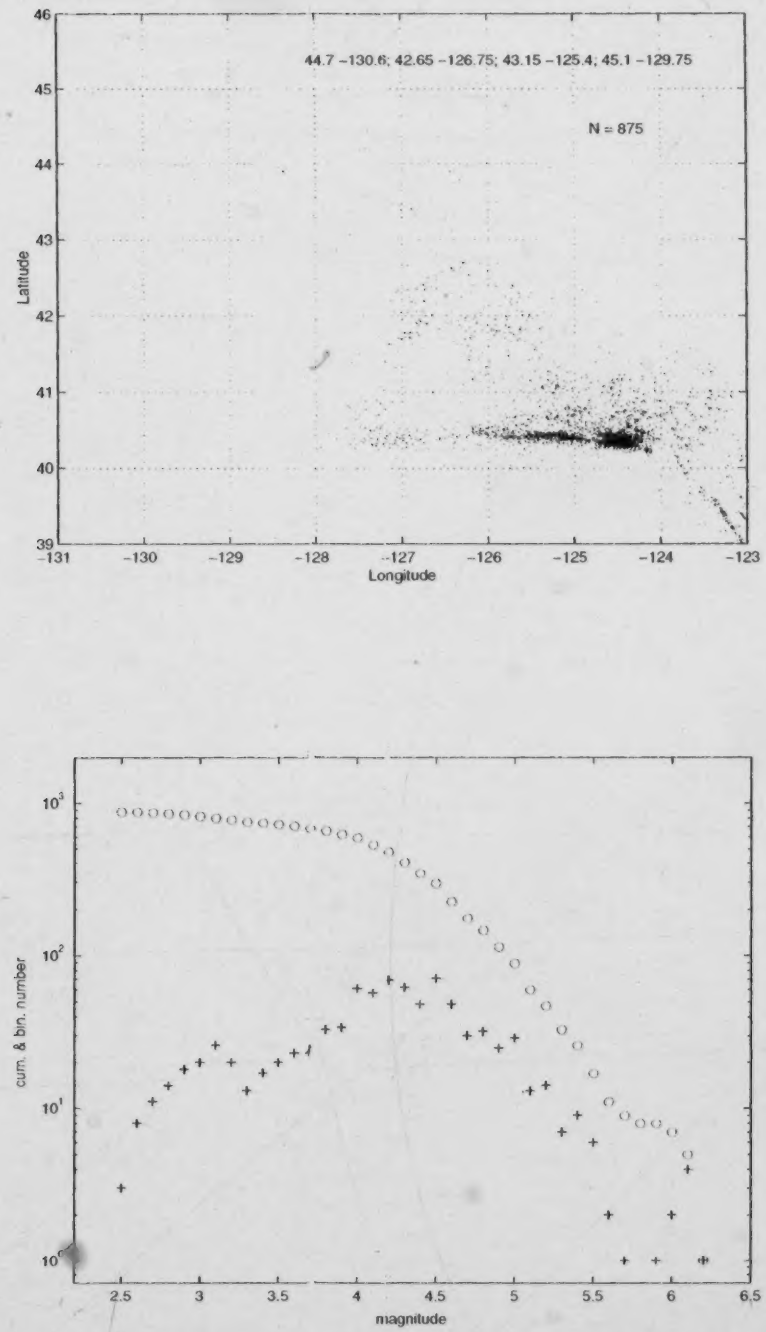

Figure 3.16: Top: pink - chosen region (from now on will be referred as *Bl*1). Bottom: magnitude-frequency distribution; cumulative dist. (o); bin dist. (+). For more details see text.

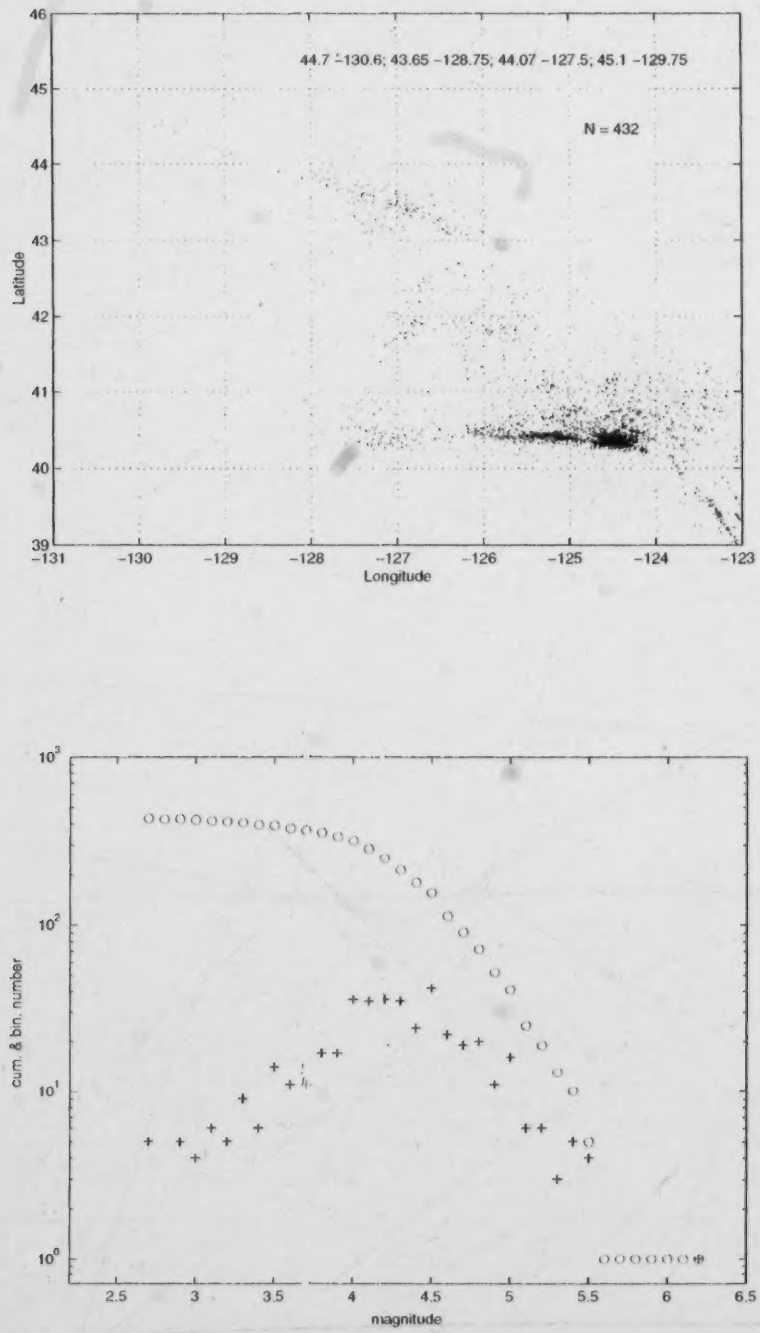

Figure 3.17: Top: pink - chosen region (from now on will be referred as *Bl*21). Bottom: magnitude-frequency distribution; cumulative dist. (o); bin dist. (+). For more details see text.

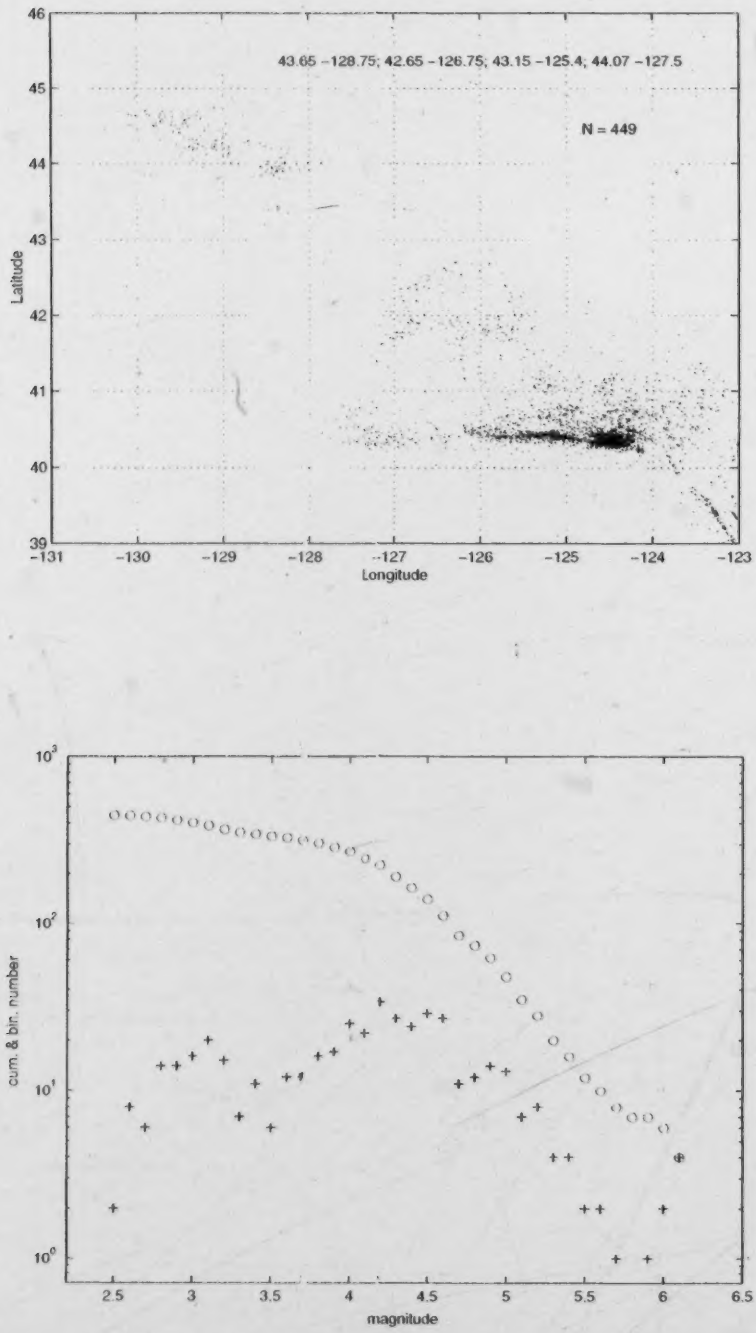

Figure 3.18: Top: pink - chosen region (from now on will be referred as *Bl*22). Bottom: magnitude-frequency distribution; cumulative dist. (o); bin dist. (+). For more details see text.

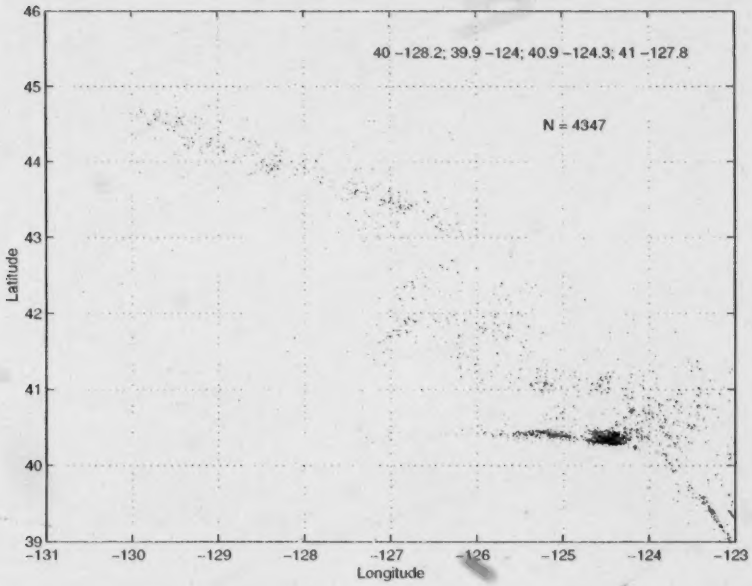

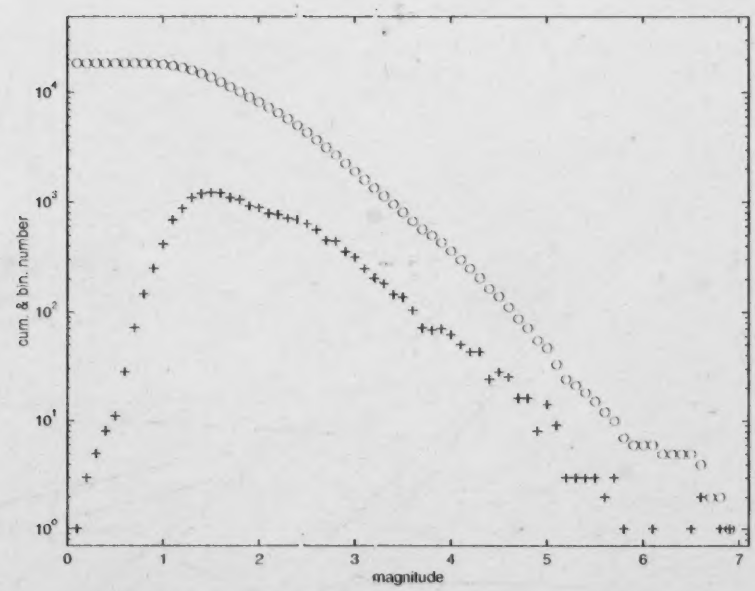

Figure 3.19: Top: pink - chosen region (from now on will be referred as $Me1$). Bottom: magnitude-frequency distribution; cumulative dist. (o); bin dist. (+). For more details see text.

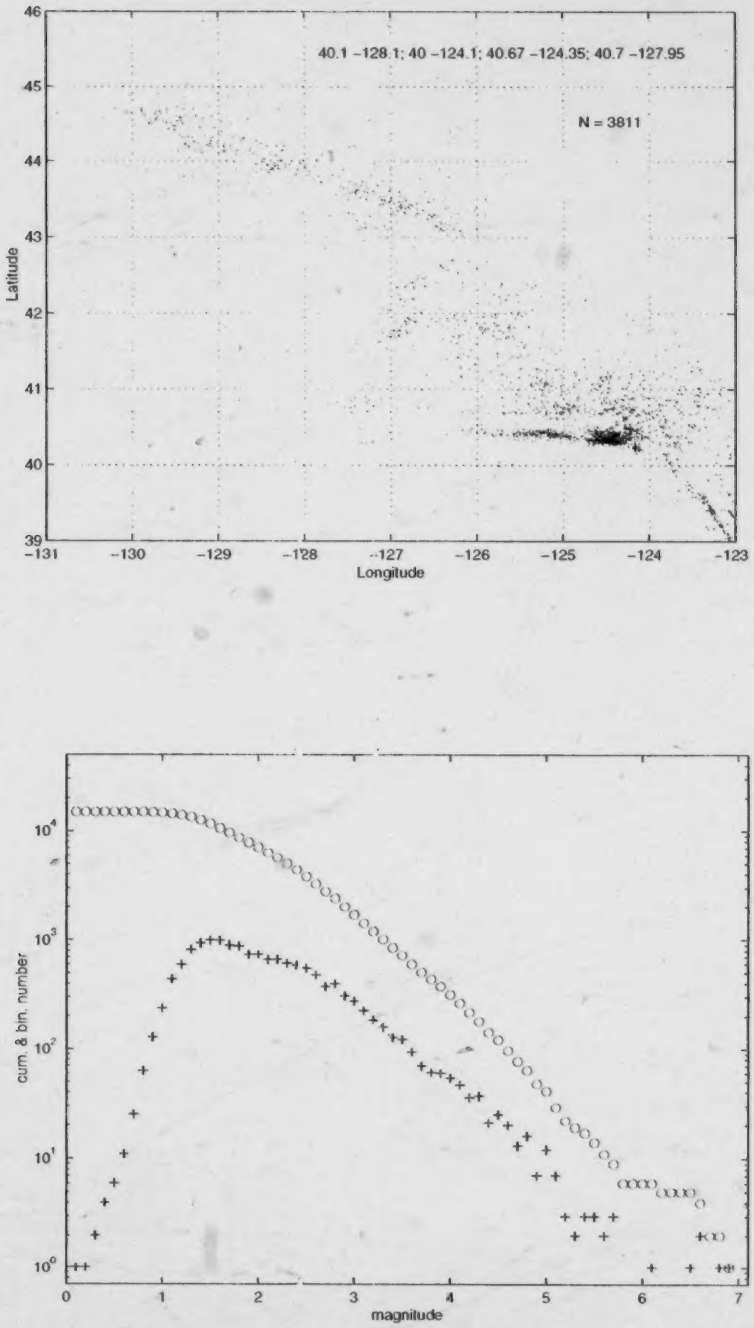

Figure 3.20: Top: pink - chosen region (from now on will be referred as $Me2$). Bottom: magnitude-frequency distribution; cumulative dist. (o); bin dist. (+). For more details see text.

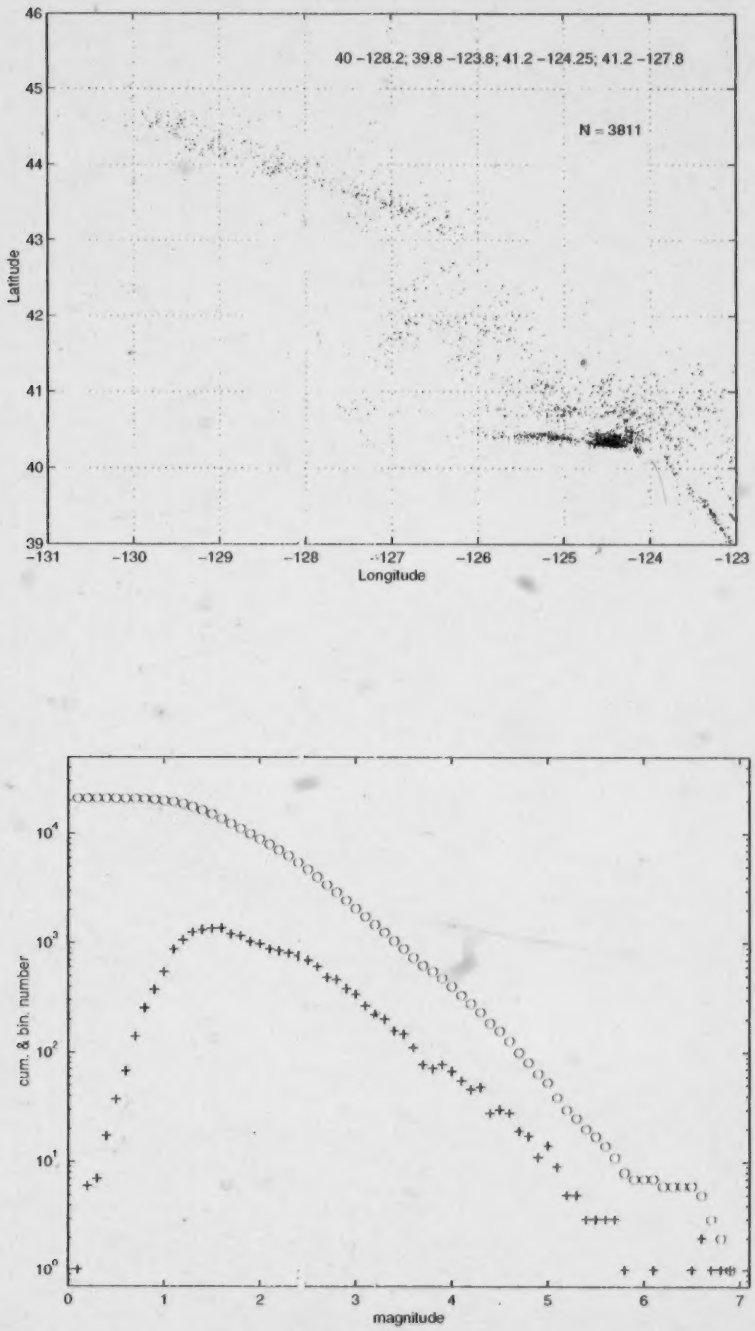

Figure 3.21: Top: pink - chosen region (from now on will be referred as *Me*3). Bottom: magnitude-frequency distribution; cumulative dist. (o); bin dist. (+). For more details see text.

3.4 Length-frequency distributions

3.4.1 Moment - length conversion

In order to evaluate length-frequency distributions, we need to determine the rupture length from the scalar seismic moment M_0. The basic relation for the scalar of the seismic moment is

$$M_0 = \mu \bar{u} A, \tag{3.9}$$

where μ is shear modulus, $\bar{u}$ is the mean slip, and A is the fault area.

The shear modulus μ is approximately constant. We consider Dziak's estimation for oceanic lithosphere (for the Blanco region), $\mu = 4 \times 10^4 MPa$ [Dziak 1991] as a typical value for the studied region. In the literature μ varies between 2.8×10^4 and 4×10^4 MPa.

The mean slip as a function of aspect ratio ($Ar = L/W_0$, where L is the rupture length and W_0 is the width of the seismogenic zone) was provided by Moritz Heimpel as a result of numerical models [1997, 2003]. Since this mean slip was dimensionless, it was scaled to the results of Yin and Rogers [1996] as shown in Figure 3.22 (mean slip over stress drop). They used circular ruptures for small earthquakes and elliptical ruptures for large ones as shown in the Figure 3.23. An example of the slip on used circular and elliptical ruptures as a result of numerical models are in Figure 3.24.

Since the models provide only the mean slip divided by the stress drop, we need to make assumptions about the stress drop. Even though there is a considerable range in the observed stress drop value of earthquakes, the stress drop is approximately constant for individual faults (see Chapter 2.3). Estimated range for stress drop σ is from about $\sigma = 0.03$ MPa to $\sigma = 30$ MPa [Scholz 1990]. Scholz [1982] suggested the stress drop ~ 0.75 MPa for strike-slip faults. In our calculations we used this value and the higher values (1.009 MPa, 1.471 MPa) as well, with the assumption that stress drop is constant for all rupture lengths.

For the rupture area we can approximate rupture propagation to proceed as in a uniform 3-dimensional full space. Thus we expect circular cracks for small earthquakes ($L \leq W_0$) with area $A_c = \pi r^2$, where r is the radius of the circular rupture. If we consider $r = L/2$, then we obtain from equation (3.9) for L

$$L = 2\sqrt{\frac{M_0}{\pi \mu \bar{u}(L)}}. \tag{3.10}$$

When the earthquake reaches the seismogenic thickness W_0 and continues to grow, it's rupture shape changes from circular to being elongated along strike (approximately

elliptical shape). Elliptical rupture as proposed by Yin and Rogers [1996] has lower half ellipse with a constant short half axis equal to $W_0/2$ and the upper half ellipse with a fixed ratio $(2b' - W_0)/(2a' - W_0) = 1/5$, where a' and b' are the long and short half axes of the upper half ellipse and $2a' = L$ (see Figure 3.23). The area of this elliptical rupture can be expressed as

$$\begin{aligned} A_e &= \frac{\pi}{8} L W_0 \\ &+ \frac{L}{2}\left(\frac{L}{10} + \frac{2}{5}W_0\right)\left[\arcsin\left(5\frac{W_0}{L+4W_0}\right)\right. \\ &+ \left.\frac{1}{2}\sin\left(2\arcsin\left(5\frac{W_0}{L+4W_0}\right)\right)\right]. \end{aligned} \tag{3.11}$$

Substituting the last expression into equation (3.9) gives the equation for the rupture length L, which does not have an analytical solution. For this reason, the area of the 'partial' ellipse (eq. 3.11) was calculated first for a specific W_0 and a range of rupture lengths (similarly as for the mean slip). The determination of rupture length L was then a matter of interpolation from

$$\bar{u}(L)A_e(L) = \frac{M_0}{\mu}. \tag{3.12}$$

Solving equations (3.10) and (3.12) allowed us to converge the seismic moments to rupture lengths for the former selected regions. For the conversion was developed the program `mole_area.m`. This program require the input of seismogenic width specific for each fault. The conversion leads to solving the equations for circular (3.10) and elliptical cracks (3.12), for which was used bisection and interpolation [Press et al,1992]. Conversion was made with respect of keeping the same cumulative and bin numbers as for corresponding seismic moments.

Obtained length distributions were then fitted with two curves based on modified GR relation. One curve fits the first part of the length distribution, which means the earthquakes with $L \leq W_0$ and the second curve fits the distribution with $L > W_0$ (further referred as second part of the distribution). The boundary between the first and the second part is later referred as the transition. Let the subscript 1 refer to the parameters of first fitting curve (for small earthquakes) and the subscript 2 refer to the parameters of fitting curve from the transition (for large earthquakes). Parameters α_1, β_1 were calculated using the linear least squares method. Parameter α_2 was counted to have the two fitting curves continuous. Parameter β_2 was set as one half of β_1 (explanation follows in the next section). The γ parameter was fixed to three times γ of corresponding moment distribution (γ_M) for the first part, and 1.5 times γ_M for the second part (explanation in the following section). The

λ parameter was taken from corresponding moment distribution and converted according to the principle of above described moment-length conversion. The same value of the λ was used for both parts. Mentioned conditions of fitting were applied to the length distributions using program `len_fix_b.m`.

Moment - length scaling

For small earthquakes ($L \leq W_0$) with circular cracks, we have $M_0 = \mu\bar{u}\pi(L/2)^2$ (using informations from Chapter 3.4.1, $M_0 = \mu\bar{u}A = \mu\bar{u}\pi r^2 = \mu\bar{u}\pi(L/2)^2$). The numerical models [Heimpel, 1997, 2003] provide for small earthquakes (see also Figure 3.22) $\bar{u} \propto L$. The above relations imply $M_0 \propto L^3$. For large earthquakes ($L > W_0$), the elliptical rupture is expected (with area equal to constant times L, so $A \propto L$, see Chapter 3.4.1) so that $M_0 \propto \bar{u}L$. For smaller aspect ratios, the mean slip is $\bar{u} \propto L$, thus these imply $M_0 \propto L^2$. But for very large earthquakes, the mean slip saturates and is constant with respect to growing size. Combining with elliptical character of rupture, these imply $M_0 \propto L$.

Using the modified GR relation for cumulative number $N = (s/\alpha)^{-\beta}exp[-(s/\lambda)^{\gamma}]$ (for notation see equation 3.3) and above described $M_0 - L$ dependence (specifically $M_0 \propto L^3$ for small earthquakes and $M_0 \propto L^2$, resp. $M_0 \propto L$ for large and very large earthquakes) imply relation between fitting parameters of moment and length distributions. Let the subscript M refer to parameters of moment distributions and the subscript L refer to parameters of length distributions. With respect to γ parameter, modified GR relation for moment distribution is $N \propto exp[-(M_0/\lambda_M)^{\gamma_M}]$. Then substituting into it $M_0 \propto L^3$, we get $N \propto exp[-(L^3/\lambda_M)^{\gamma_M}]$ for small earthquakes, which implies that for length distributions $\gamma_L = 3\gamma_M$. For this reason this prescription was used for fitting curve of length distributions for small earthquakes. The same principle applied to large and very large earthquakes then implies γ_L equal to (2 to 1) of γ_M. $\gamma_L = 1.5\gamma_M$ was chosen for fitting curve of earthquakes after transition.

From the same reason as for γ, the β_L should be three times of β_M for small earthquakes. But both β_L and β_M were calculated by the least square method from the data and were the object of observation with results discussed later. The change in β_L parameter from small to large earthquakes can be understand from the following arguments. The theory of elasticity and the random walk model imply $N \propto A^{-1}$ [Heimpel, 1997].

For the small earthquakes, taking $M_0 \propto \bar{u}A$ (from equation 3.9) and $\bar{u} \propto L \propto A^{1/2}$ (as argued above), we get $M_0 \propto A^{3/2}$ or $A \propto M_0^{2/3}$. Then from basic assumption $N \propto A^{-1} \propto M_0^{-2/3}$. Combining the latter statement with moment-length relation $M_0 \propto L^3$ (as shown

above), we get $N \propto L^{-2}$ for small earthquakes.

Similarly for the large ones $M_0 \propto \bar{u}A$, where $A \propto W_0 L$ (since W_0 is constant, $A \propto L$) and $\bar{u} \propto L$. These imply $M_0 \propto L^2$ and since $L \propto A$ (see above), then $M_0 \propto A^2$ or $A \propto M_0^{1/2}$. Using the last statement and $N \propto A^{-1}$ gives $N \propto M_0^{-1/2}$ and in the terms of L, $N \propto L^{-1}$.

Thus these calculations imply the slope of large earthquakes (β_{L_2}) to be a one half of slope for small ones (β_{L_1}), so the parameter β_{L_2} (β of length distribution for large earthquakes) was set up as 1/2 of β_L for small earthquakes.

For the very large earthquakes the slope of length distributions starts to change again. The slope of length distributions increase, due to exponential part of modified GR relation (equation 3.3).

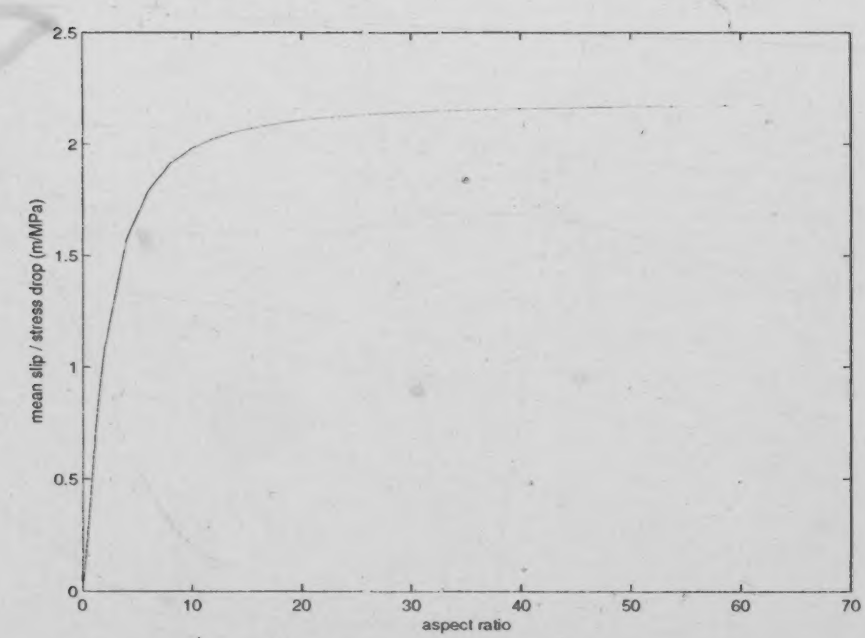

Figure 3.22: The mean slip over stress drop (scaled according to Yin and Rogers [1996]) as a function of aspect ratio as a result of numerical models.

Figure 3.23: Geometry of the used ruptures, circular (red), elliptical (blue) as proposed in Yin and Rogers [1996]

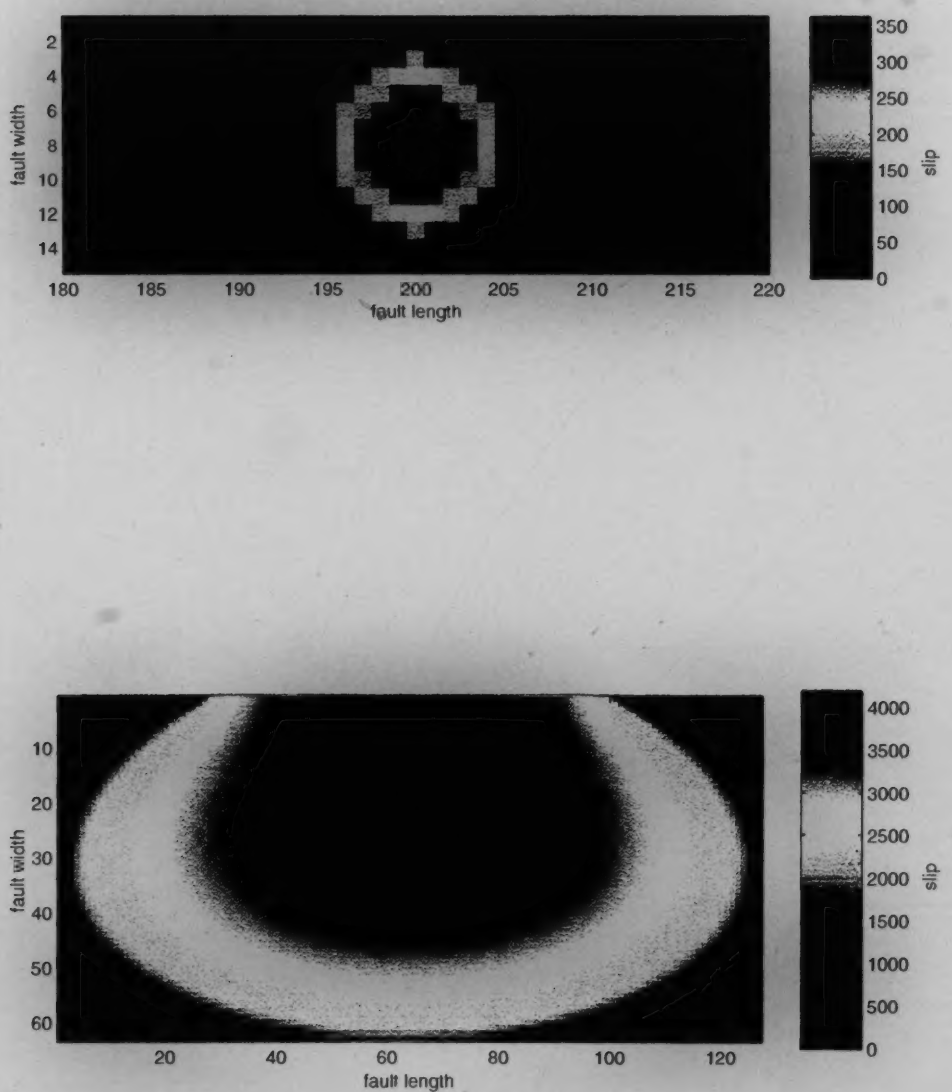

Figure 3.24: Top: slip (in model units) on circular rupture. The figure shows 1/10 of the full length of the fault of aspect ratio 25. Bottom: slip (in model units) on elliptical rupture. Shape of ruptures defined in Yin and Rogers [1996]. Figures provided by M. Heimpel.

3.4.2 Results for length distributions

This section summarizes the results of length-frequency distributions and corresponding fitting curves for the same variations of the chosen regions used for the moment distributions. Length distributions are presented in Figures 3.25 - 3.38 and corresponding parameters in Table 3.1.

The length-frequency distributions for the Queen Charlotte fault in Fig. 3.25 and 3.26 show very similar behavior. We analyze four different sets for each QC region. The first set (in Fig. 3.25 a, 3.26 a, for $QC1$ and $QC2$ respectively) used for moment-length conversion, fault width 20 km and stress drop 0.75 MPa. For set in Figures 3.25 b and 3.26 b was used the same width (20 km) and the stress drop 1.471 MPa. This stress drop was chosen to fit the maximum converted rupture length to 450 km. 450 km is presented as the best estimate [Rogers, 1985] for rupture length of the maximum earthquake occurred on QC fault with magnitude 8.1, that occurred on August 22, 1949, with assumed fault width of 20 km. For the next two sets (Figure 3.25 c, d, Figure 3.26 c, d, respectively) we chose 30 km as the typical seismogenic width, which may be a better estimate for QC. We used Scholz's [1982] suggestion of stress drop 0.75 MPa for the case shown in Figures 3.25 c and 3.26 c. The last set (further referred as *case d*), shown in Figures 3.25 d and 3.26 d, used the stress drop 1.009 MPa, which fits the maximum rupture length to 450 km (explanation above).

As mentioned before the length distributions were fitted by two curves. The transition (as defined in previous section) should appear at rupture length the same as the chosen fault width (since the rupture shape change from circular to elliptical). But for all the QC sets we observe the slight delay, which is the smallest in the *case d*. This case can be examined as the best fit and the characteristic lengths are 487 km, 449 km for $QC1$, $QC2$ respectively. Parameters β for the first part of distributions have values 1.2 to 1.3. Other parameters are prescribed by the rules set up in previous section.

For all other fault regions ($RD, So, No, SoNo, RDSoNo$) we choose 5 km for the seismogenic width and two different values for the stress drop: 0.75 MPa following Scholz's [1982] suggestion for strike-slip faults (this case is shown on the top of the figures) and 1.471 MPa (explained above) as the value for QC maximum earthquake length fit (shown on the bottom of the figures).

The Revere-Dellwood length distributions are the next example of fitting, shown in Fig. 3.27, 3.28, 3.29. While the $RD1$ distributions are fitted very well, the fitting curves for $RD2$, $RD3$ with lower stress drop (0.75 MPa) slightly underestimate the second part of

the distributions. All three regions show similar behavior and the transition corresponds to the chosen value of seismogenic width (5 km) well. The first part of the distribution (as defined in previous section) can be characterized as power-law without any curvature. The β_1 values are close to 2, which are significantly larger values than for other faults. The second part shows exponential tail. In terms of γ and λ parameters, the first part does not 'feel' their influence but they characterize the drop-off for the end of second part. The characteristic length would be 110 - 137 km for $\sigma = 0.75$ MPa or 57 - 70 km for $\sigma = 1.471$ MPa.

Even though the Sovanco fault system is, geologically, probably one of the most challenging, the length-frequency distributions show typical behavior with successful fitting. The small earthquakes are characterized by a power law (see Fig. 3.30, 3.31, 3.32) with $\beta \sim 1.2 - 1.4$ for all chosen regions. The transition corresponds to prescribed fault width of 5 km. Obtained characteristic lengths vary from 68 to 128 km for lower stress drop (0.75 MPa) and they are from 35 - 66 km for higher one (1.471MPa).

The Nootka fault is another difficult and complex fault system. *No* shows atypical behavior for length-frequency distributions. For all three selected regions for Nootka fault (Fig. 3.33, 3.34, 3.35), the first part (the part of length distributions considered up to transition), does not show the plain power law so typical for other analyzed regions. Instead, the cumulative distribution has a 'bump' on the fitting curve for the small rupture lengths, followed by a drop-off for larger earthquakes. The transition is not very clear and can be guessed to be shifted several kilometers from prescribed value. Lambda parameters suggest characteristic size from 42 to 56 km and 22 to 29 km for $\sigma = 0.75$ MPa, $\sigma = 1.471$ MPa, respectively.

Combined distributions of *So* and *No* adopted mostly the *So* behavior and as shown on Fig. 3.36, 3.37 they belong to the 'typical' group. Even the transition is not so clear as in *So* case. The power law for the first part and exponential tail in the end of second part are also observed for *RDSoNo* region (Fig. 3.38). The β_1 is higher than in the previous case, what is caused by *RD* contributions.

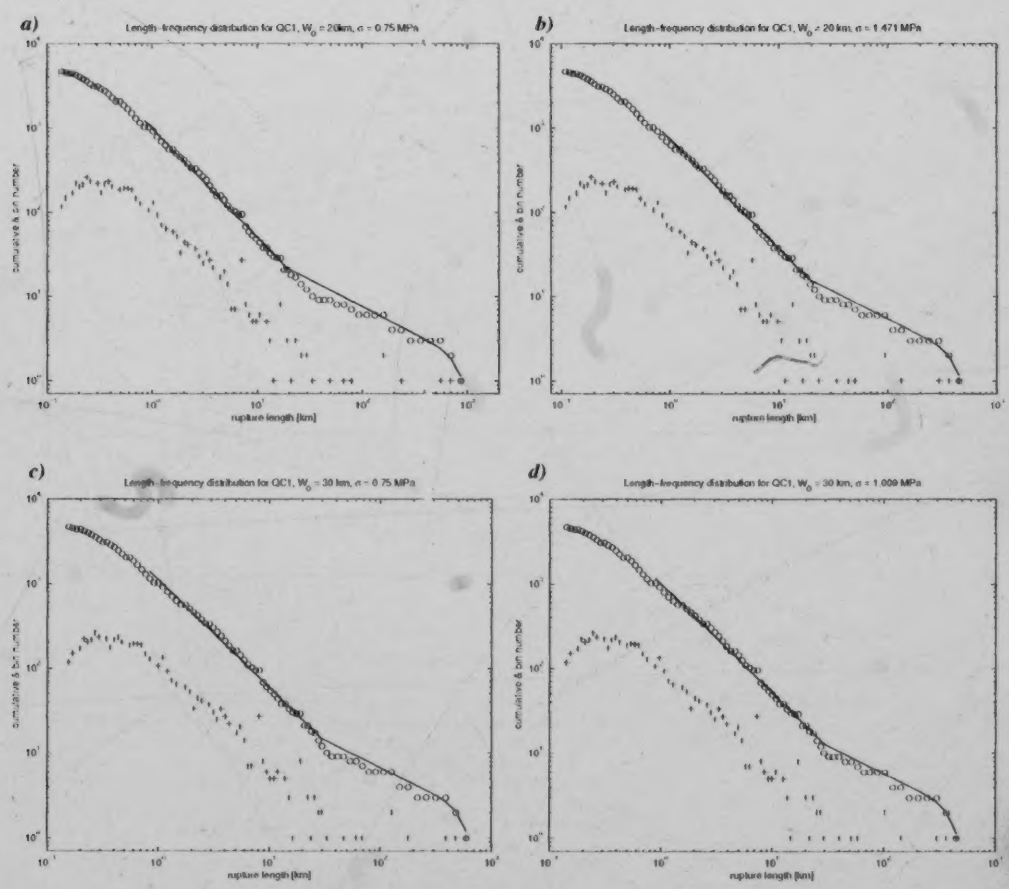
a)
Length-frequency distribution for QC1, W0 = 20km, σ = 0.75 MPa
b)
Length-frequency distribution for QC1, W0 = 20 km, σ = 1.471 MPa
c)
Length-frequency distribution for QC1, W0 = 30 km, σ = 0.75 MPa
d)
Length-frequency distribution for QC1, W0 = 30 km, σ = 1.009 MPa
cumulative & bin number
rupture length [km]

Figure 3.25: Length-frequency distribution for $QC1$, with fitting curve (-) for cumulative dist. (o); bin dist. (+). Width of the fault is 20 km (top) and 30 km (bottom). Stress drop is 0.75 MPa for a), c), 1.471 MPa for b), and 1.009 MPa for d). For more details see text.

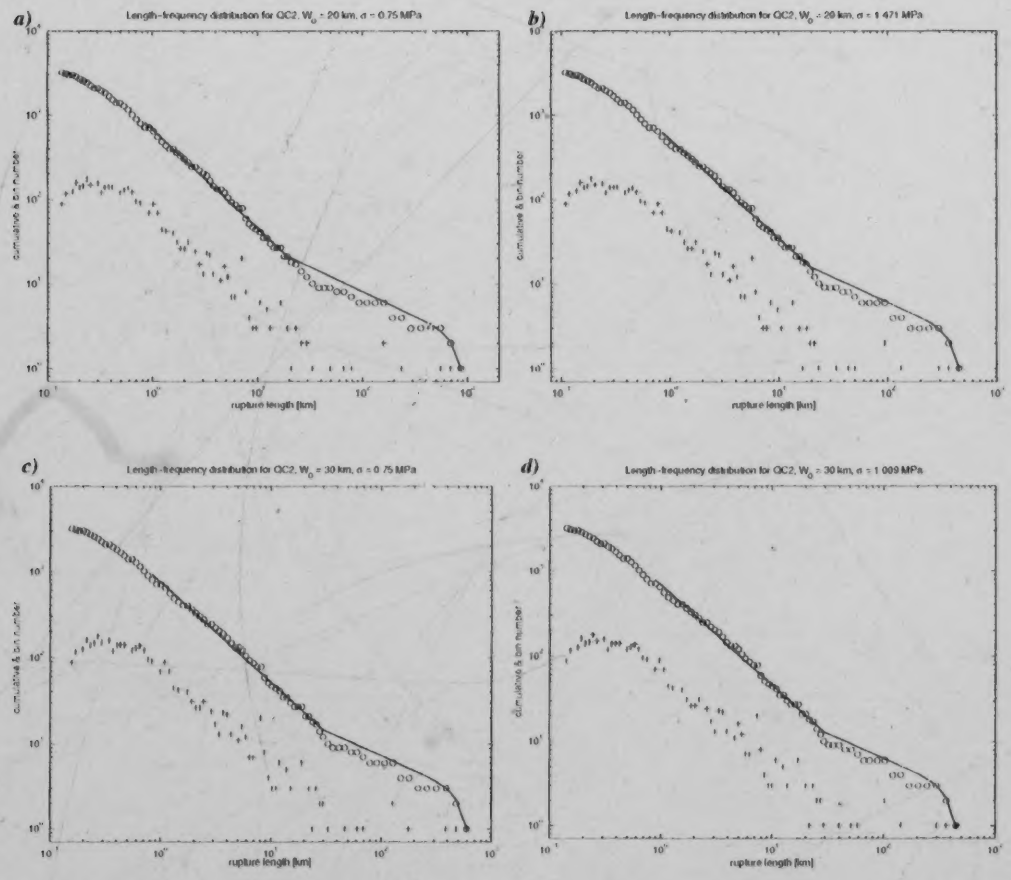
a)
Length-frequency distribution for QC2, W0 = 20 km, σ = 0.75 MPa
b)
Length-frequency distribution for QC2, W0 = 20 km, σ = 1.471 MPa
c)
Length-frequency distribution for QC2, W0 = 30 km, σ = 0.75 MPa
d)
Length-frequency distribution for QC2, W0 = 30 km, σ = 1.009 MPa
cumulative & bin number
rupture length [km]

Figure 3.26: Length-frequency distribution for $QC2$, with fitting curve (-) for cumulative dist. (o); bin dist. (+). Width of the fault is 20 km (top) and 30 km (bottom). Stress drop is 0.75 MPa for a), c), 1.471 MPa for b), and 1.009 MPa for d). For more details see text.

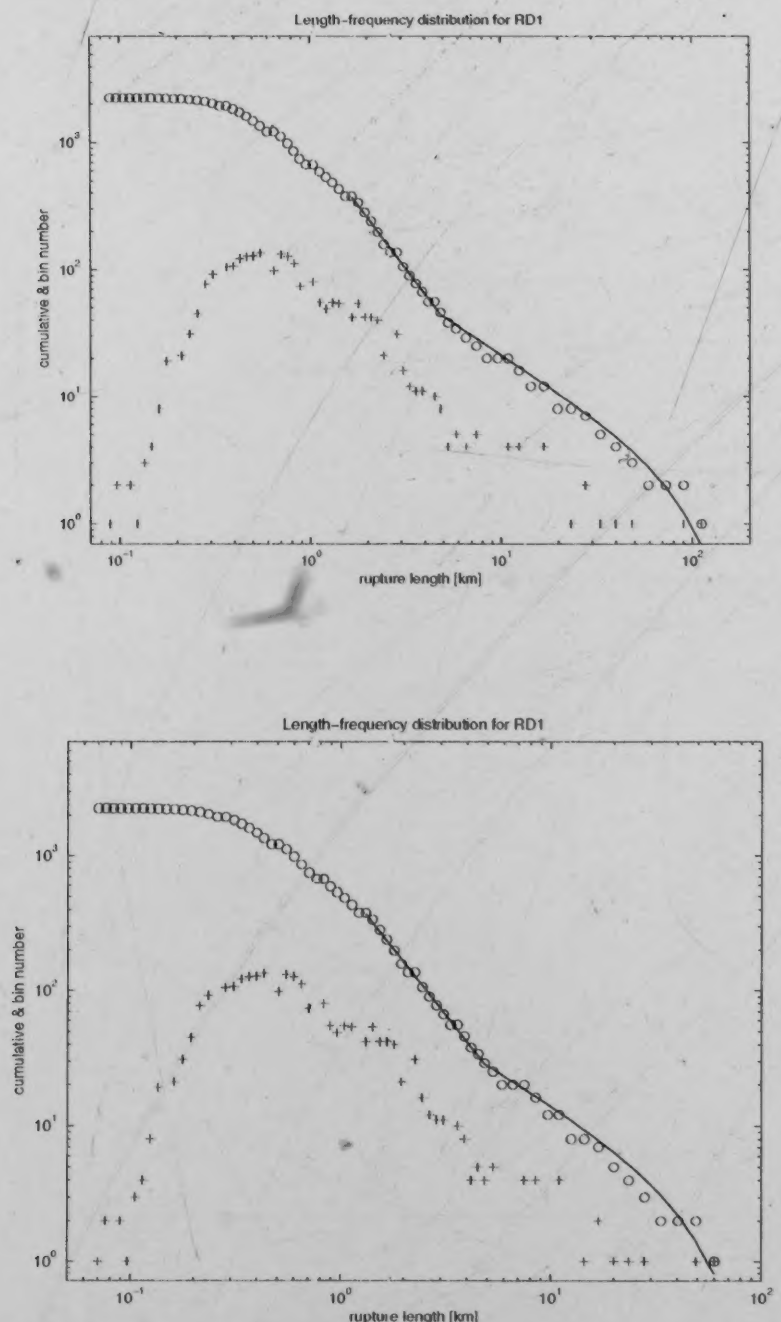

Figure 3.27: Length-frequency distribution for $RD1$, with fitting curve (-) for cumulative dist. (o); bin dist. (+). Width of the fault is 5 km, stress drop is 0.75 MPa (top) and 1.471 MPa (bottom). For more details see text.

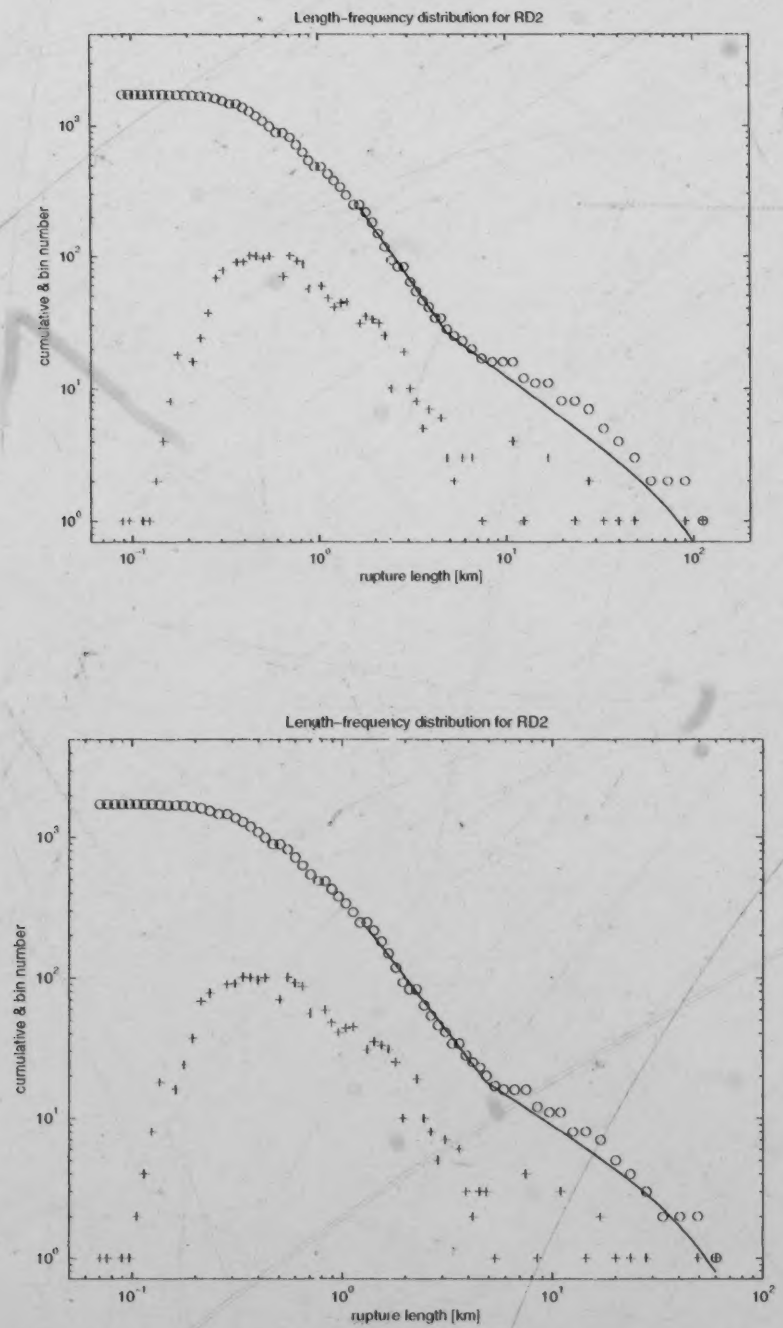

Figure 3.28: Length-frequency distribution for $RD2$, with fitting curve (-) for cumulative dist. (o); bin dist. (+). Width of the fault is 5 km, stress drop is 0.75 MPa (top) and 1.471 MPa (bottom). For more details see text.

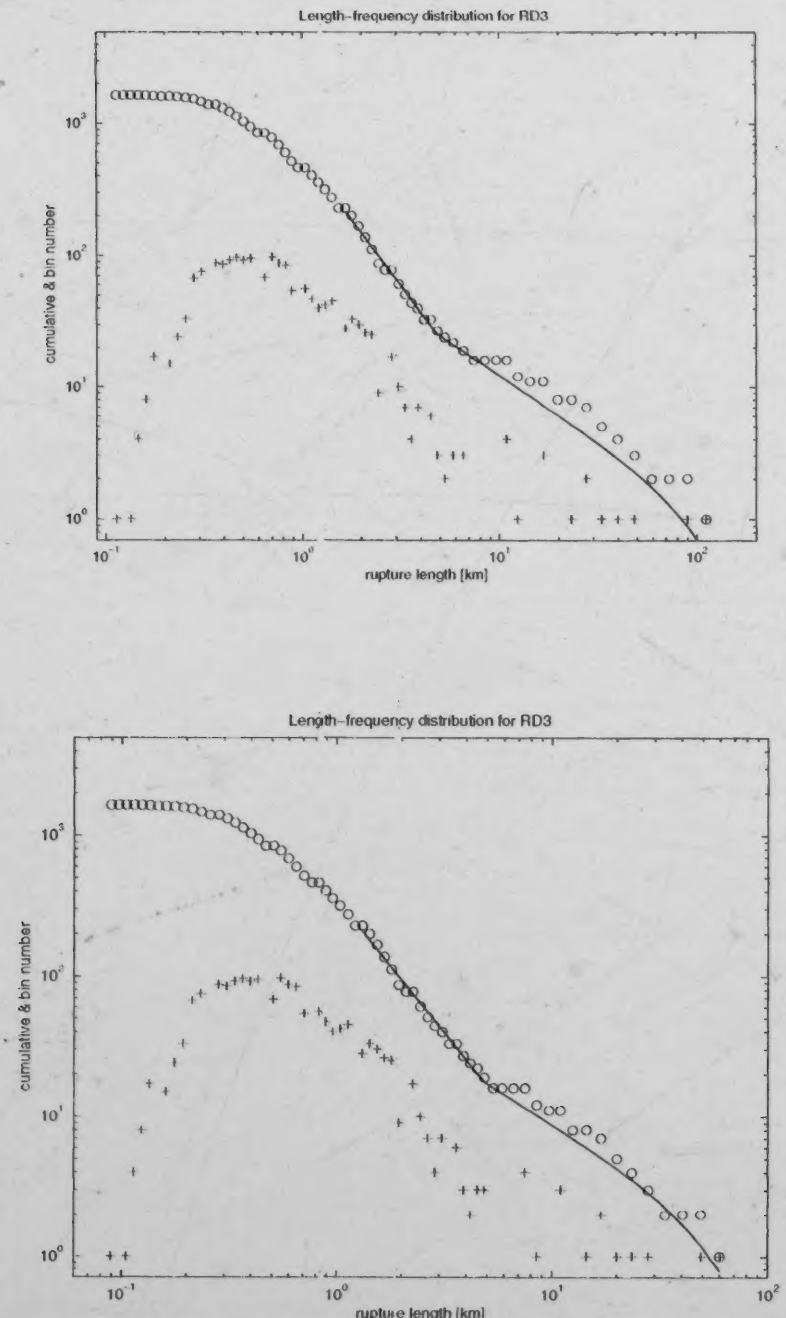

Figure 3.29: Length-frequency distribution for $RD3$, with fitting curve (-) for cumulative dist. (o); bin dist. (+). Width of the fault is 5 km, stress drop is 0.75 MPa (top) and 1.471 MPa (bottom). For more details see text.

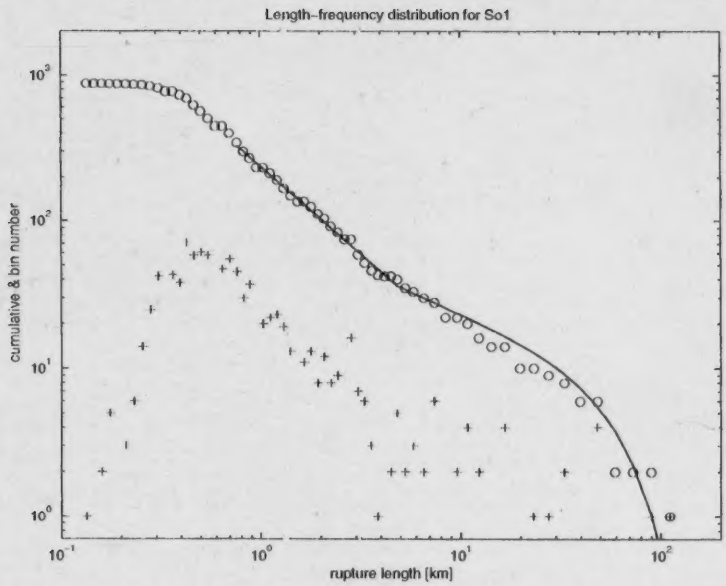

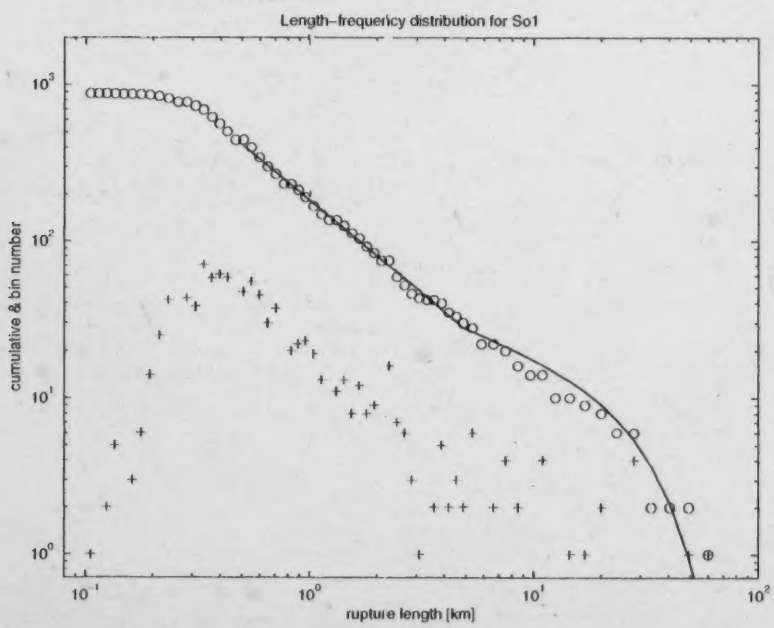

Figure 3.30: Length-frequency distribution for *So*1, with fitting curve (-) for cumulative dist. (o); bin dist. (+). Width of the fault is 5 km, stress drop is 0.75 MPa (top) and 1.471 MPa (bottom). For more details see text.

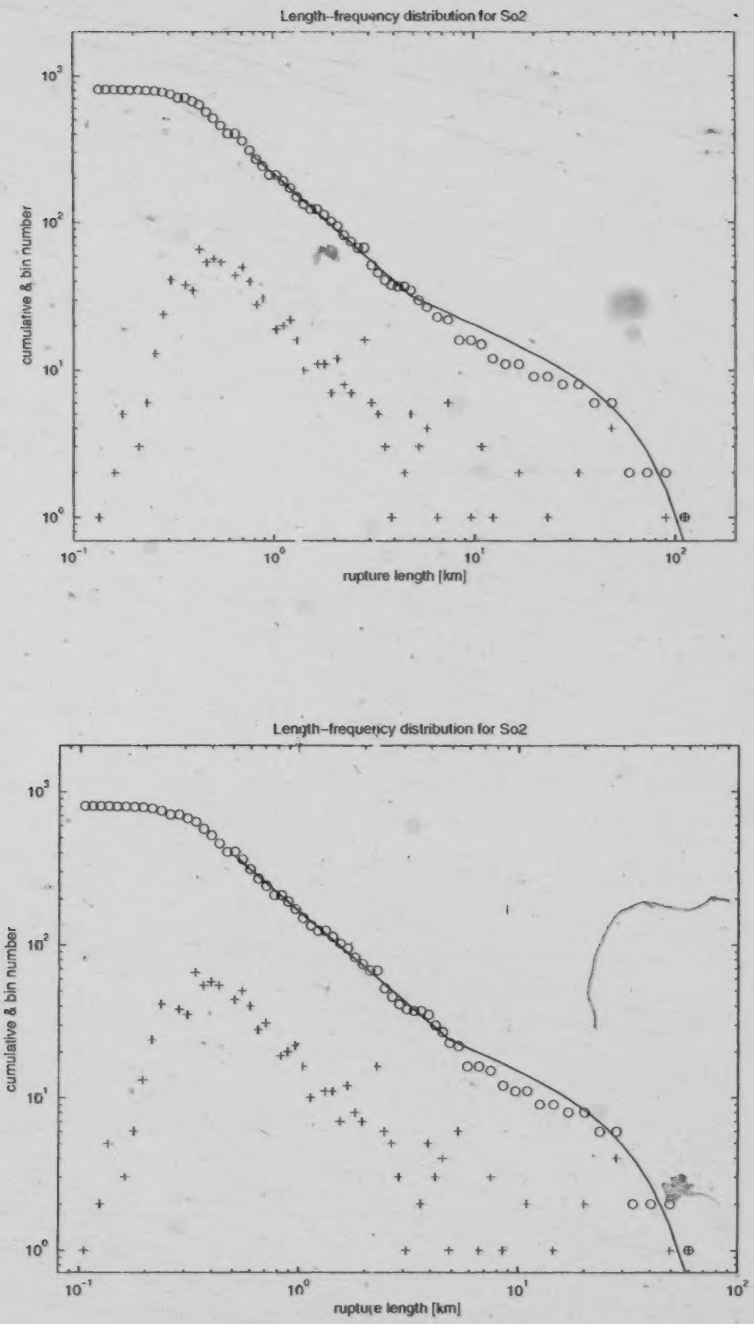

Figure 3.31: Length-frequency distribution for *So2*, with fitting curve (-) for cumulative dist. (o); bin dist. (+). Width of the fault is 5 km, stress drop is 0.75 MPa (top) and 1.471 MPa (bottom). For more details see text.

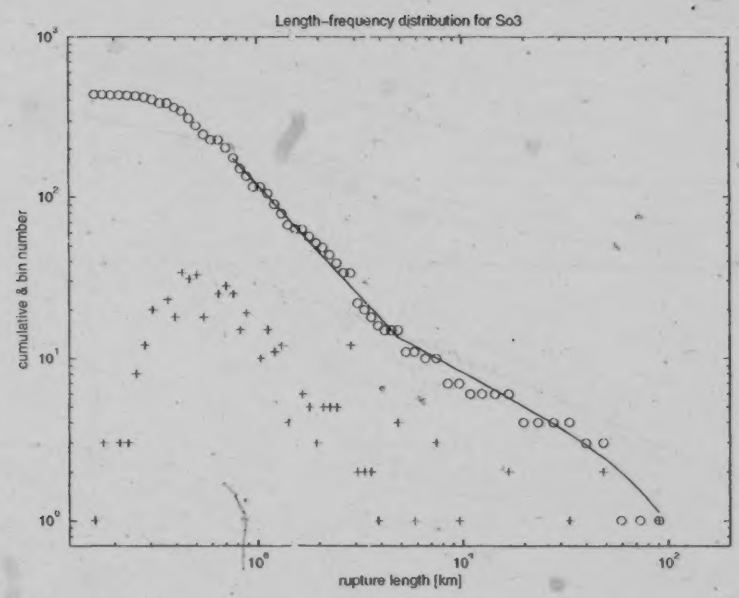

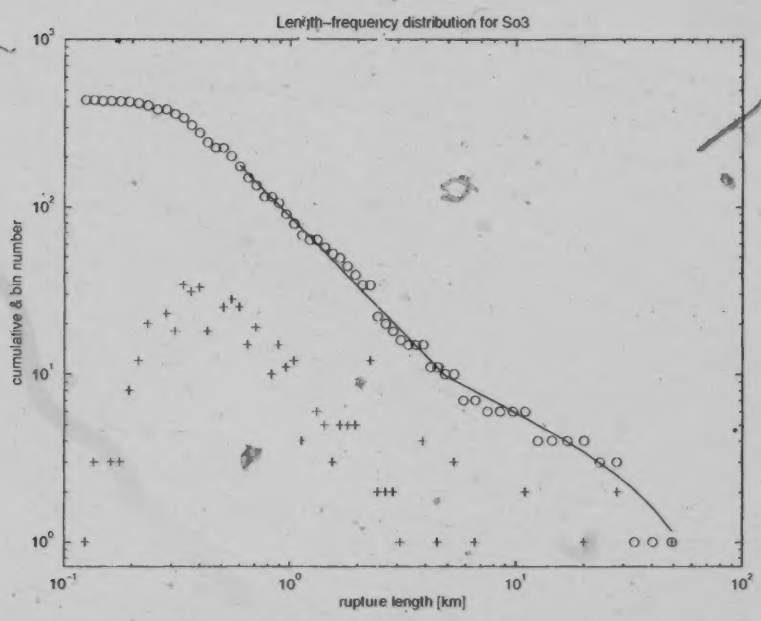

Figure 3.32: Length-frequency distribution for *So3*, with fitting curve (-) for cumulative dist. (o); bin dist. (+). Width of the fault is 5 km, stress drop is 0.75 MPa (top) and 1.471 MPa (bottom). For more details see text.

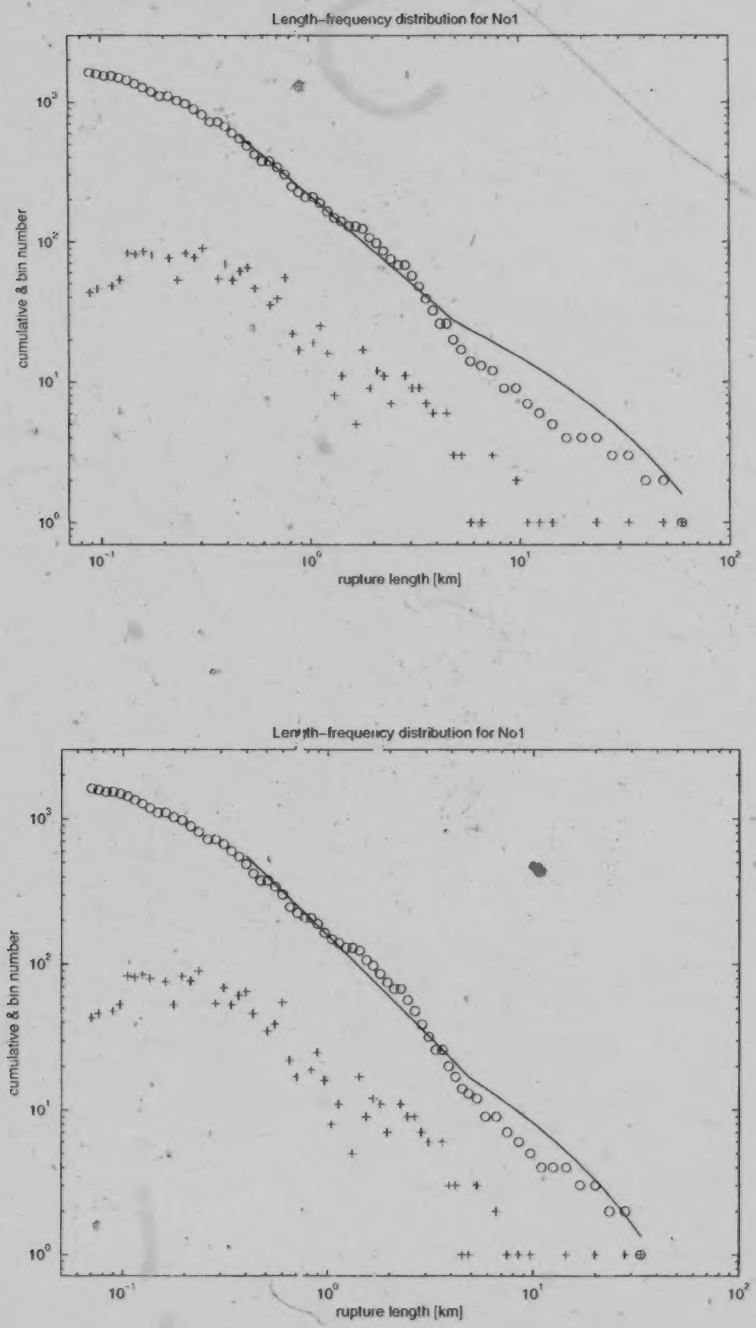

Figure 3.33: Length-frequency distribution for *No*1, with fitting curve (-) for cumulative dist. (o); bin dist. (+). Width of the fault is 5 km, stress drop is 0.75 MPa (top) and 1.471 MPa (bottom). For more details see text.

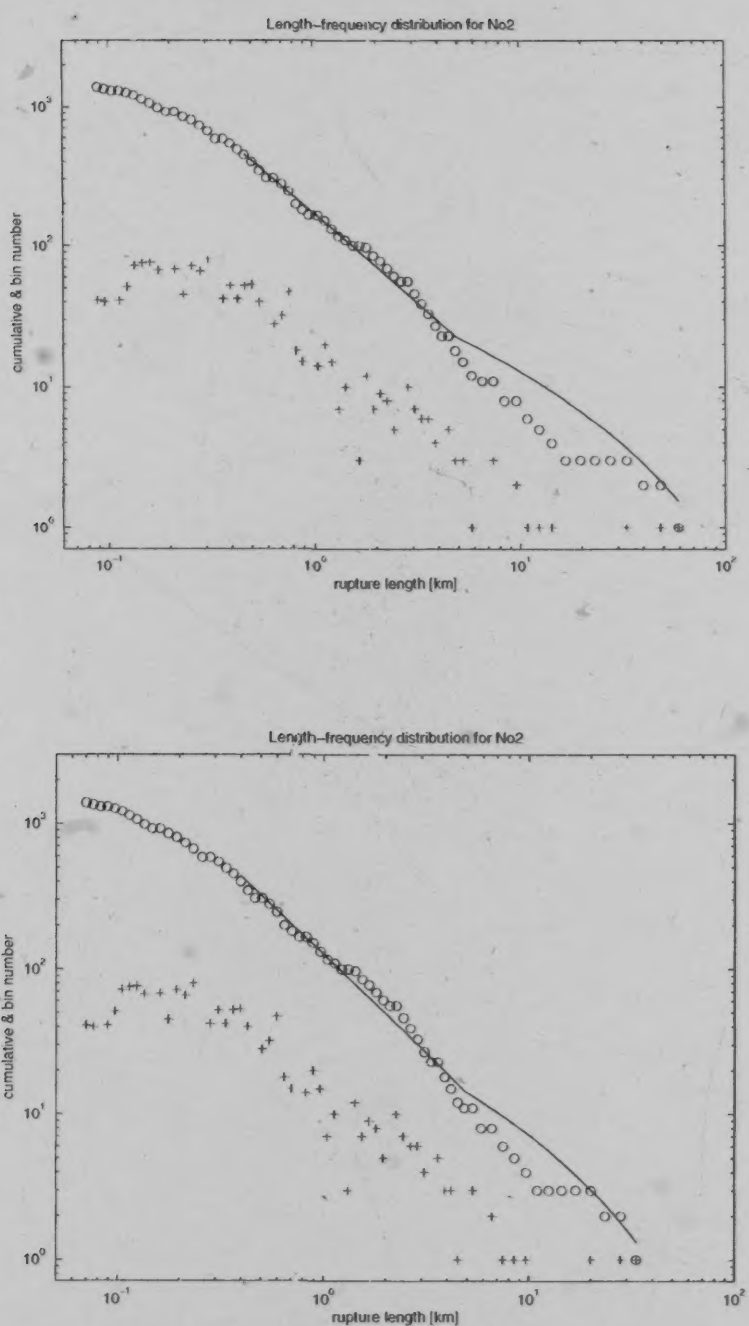

Figure 3.34: Length-frequency distribution for $No2$, with fitting curve (-) for cumulative dist. (o); bin dist. (+). Width of the fault is 5 km, stress drop is 0.75 MPa (top) and 1.471 MPa (bottom). For more details see text.

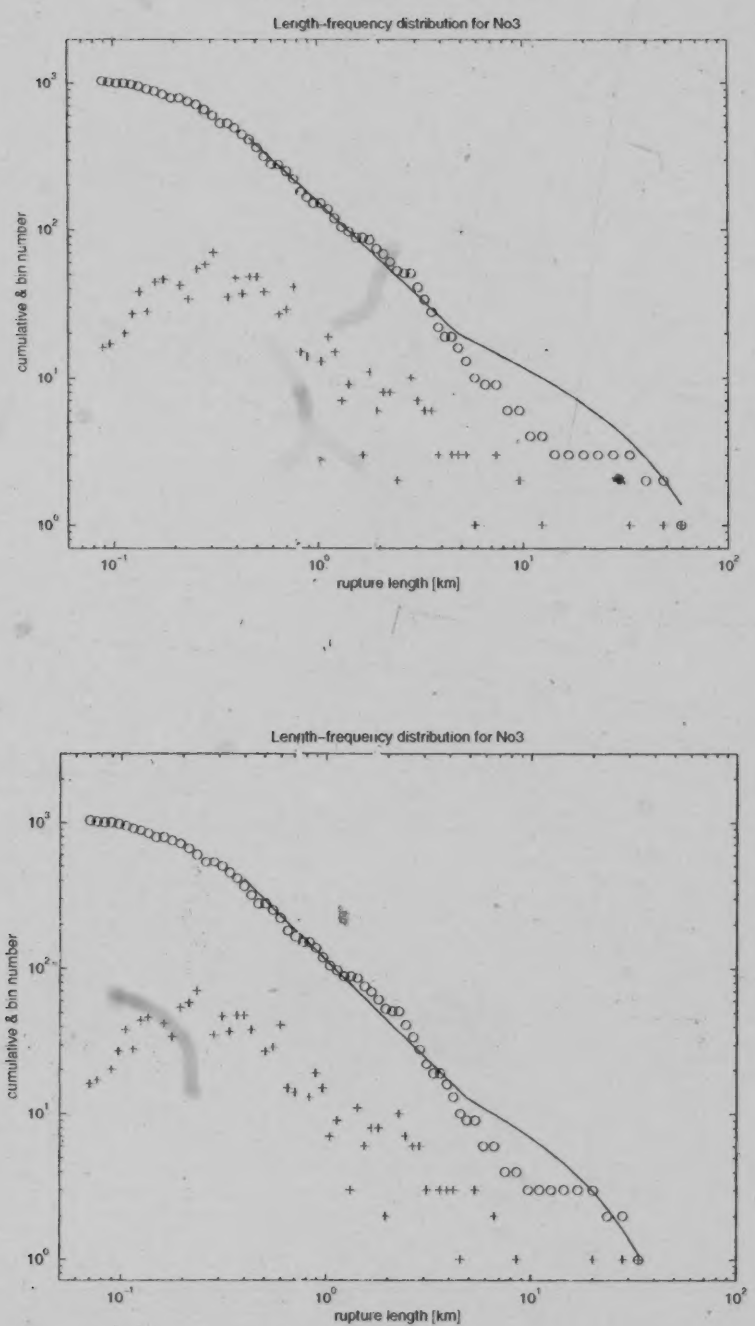

Figure 3.35: Length-frequency distribution for $No3$, with fitting curve (-) for cumulative dist. (o); bin dist. (+). Width of the fault is 5 km, stress drop is 0.75 MPa (top) and 1.471 MPa (bottom). For more details see text.

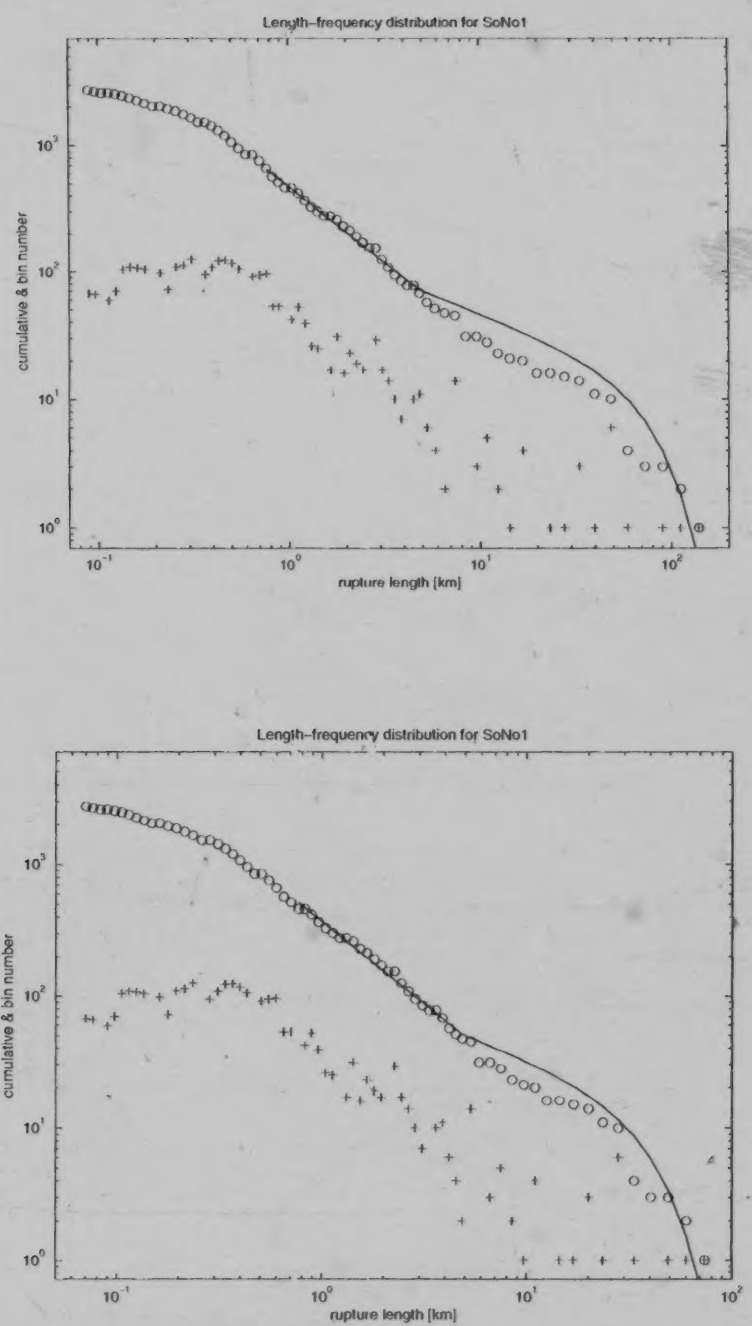

Figure 3.36: Length-frequency distribution for $SoNo1$, with fitting curve (-) for cumulative dist. (o); bin dist. (+). Width of the fault is 5 km, stress drop is 0.75 MPa (top) and 1.471 MPa (bottom). For more details see text.

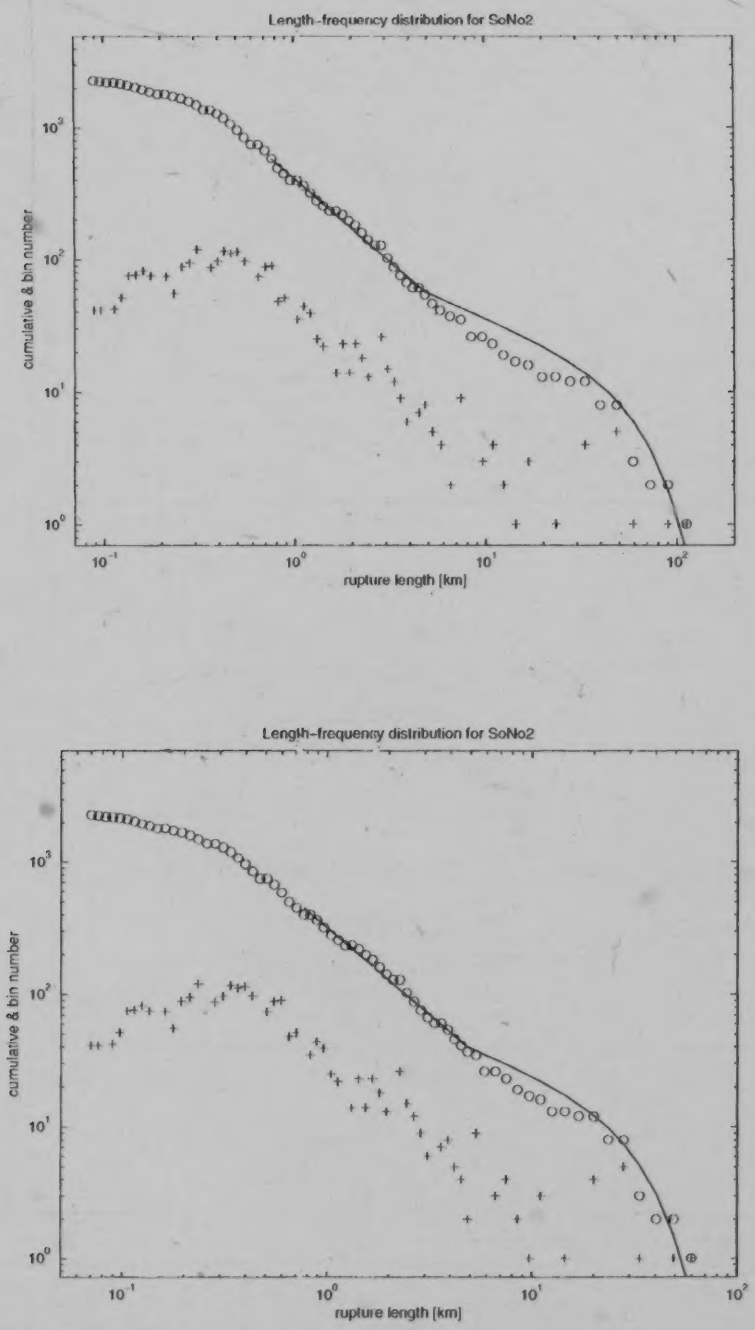

Figure 3.37: Length-frequency distribution for *SoNo2*, with fitting curve (-) for cumulative dist. (o); bin dist. (+). Width of the fault is 5 km, stress drop is 0.75 MPa (top) and 1.471 MPa (bottom). For more details see text.

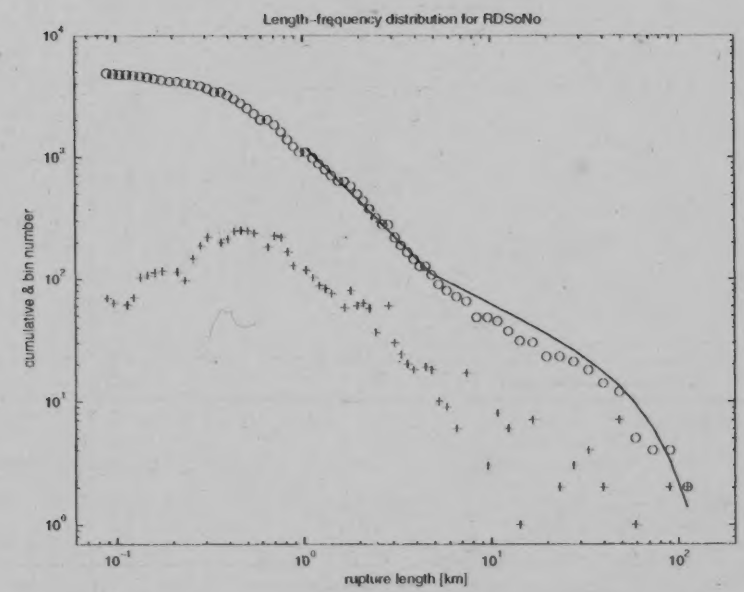

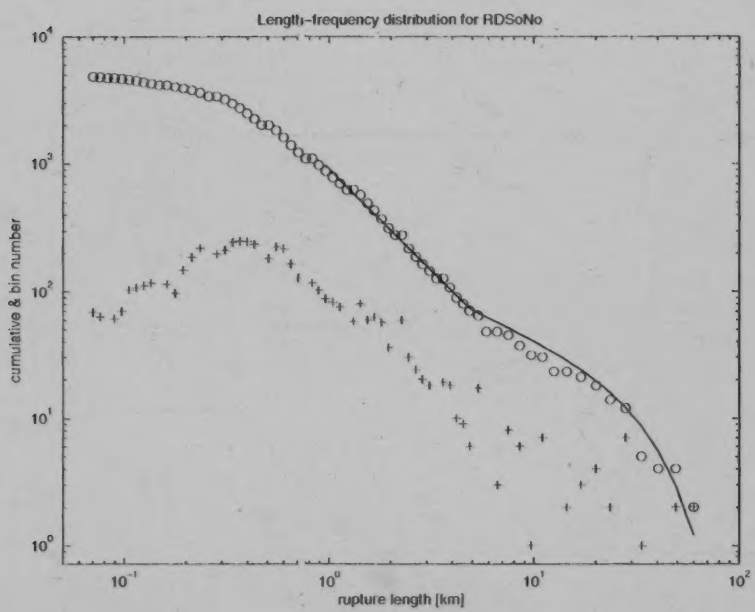

Figure 3.38: Length-frequency distribution for *RDSoNo*, with fitting curve (-) for cumulative dist. (o); bin dist. (+). Width of the fault is 5 km, stress drop is 0.75 MPa (top) and 1.471 MPa (bottom). For more details see text.

3.5 Numerical Models

We use numerical models for two purposes. First, to calculate the mean slip as a function of aspect ratio for the moment to length conversion (see also section 3.4.1). Second, to obtain moment and length distributions for various aspect ratios to be able to compare them with the data. This should help us to answer the question of the influence of the geometry of the fault on the size of earthquakes.

The models use exact solutions of static three-dimensional elasticity in the pseudo-dynamical approximation (meaning that the amplitudes of stresses neglect inertia, whereas the associated friction evolution during slip events are dynamical). In addition, viscous flow is modeled in an infinite half-space below the crust using a simple Maxwell relaxation. For strength a 'smooth' (simplified version of Dieterich-Ruina rate and state dependent friction law) or heterogeneous asperity model (random power law strength distribution) is implemented [Heimpel, 1997; Heimpel, 2003].

Some of the results of these models are shown in Figures 3.39 to 3.42. The corresponding fitting parameters are in Table 3.2. We present size distributions, both the moment and the length, for aspect ratio $Ar = 1$ with open side boundaries, $Ar = 1$ with periodic side boundaries, $Ar = 12$ and $Ar = 55$ with open side boundaries.

Figure 3.39 shows the distributions for $Ar = 1$ with open side boundaries. On the top is the moment-frequency distribution successfully fitted by the modified GR relation. Small events obeying power law distribution yield $\beta = 0.77$. This dependence smoothly changes into an exponential tail for the large events. The parameter γ is 0.6 and the parameter λ is 1.08×10^8. The presented seismic moment does not have any particular physical units. At the bottom of the figure is the corresponding length distribution, fitted by modified GR relation as well. The used lengths are dimensionless, they represent the length of the fault divided by the fault width. The β for this distribution is 1.09. It is higher than the β for moment distribution, but their ratio is not 3, as theory and data show. The exponential tail has much stronger transition than in the moment case. The γ parameter for length distribution is significantly ($\sim$ 9 times) higher than for the moment distribution ($\gamma = 5$). The λ parameter is 0.77.

The next Figure (3.40) represents distributions for aspect ratio 1 with the periodic side boundary conditions. Comparing to previous situation (the same aspect ratio), the distributions show completely different behavior. Cumulative distributions for both the moment and the rupture length, show so called characteristic behavior. From this reason

they could not be fitted by modified GR relation. The bin distributions show a different behavior as well. For all the aspect ratios with the open side boundaries the bin distributions behave similarly to cumulative ones, and the tail is dropping off. For the periodic side boundary conditions the bin distributions show peak of increase appearing at the end of the distribution, after the power-law part.

Aspect ratios 12 and 55 (Fig. 3.41, 3.42) have very similar shapes for moment and length distributions, respectively. All were successfully fitted using modified GR relation. The power law that described the distributions for small events changed more sharply than for $Ar = 1$ into the exponential tail. The fitting parameters are close for both aspect ratios (for the values of parameters see Table 3.2). Comparing β values for moment and length distributions, we see that their ratio is not 3. But the ratio for γ parameters is exactly 3 for both aspect ratios 12 and 55.

Comparison results of models with the data follows in the discussion.

	β	$d\beta$	γ	λ
Moment, $Ar = 1$	0.777	0.006	0.60	1.04×10^8
Length, $Ar = 1$	1.070	0.004	5.20	0.72
Moment, $Ar = 12$	0.749	0.003	1.00	3.18×10^8
Length, $Ar = 12$	1.018	0.004	3.00	5.58
Moment, $Ar = 55$	0.734	0.002	1.00	2.93×10^8
Length, $Ar = 55$	0.994	0.006	3.00	6.82

Table 3.2: Parameters for fitting curves for distributions of numerical models for different aspect ratios ($Ar = 1, 12, 55$) with open side boundaries; Moment refers to moment distributions; Length refers to length distributions.

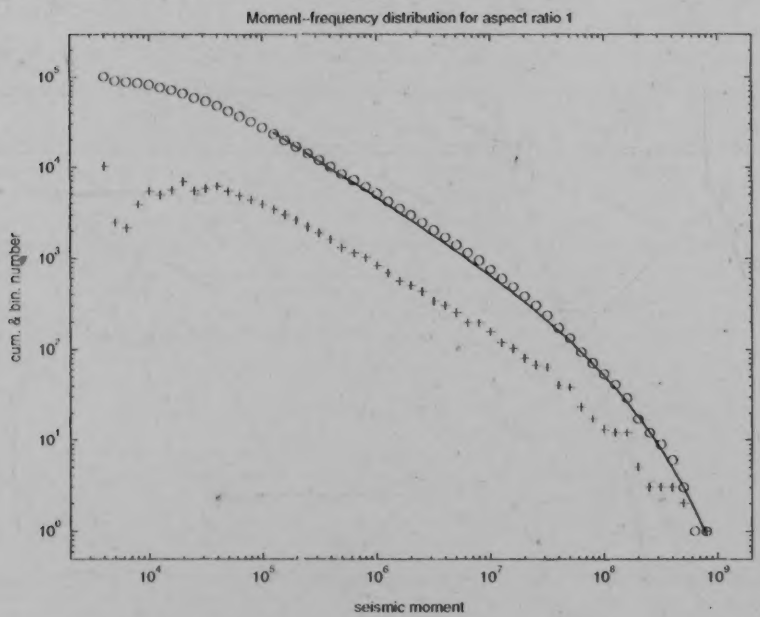

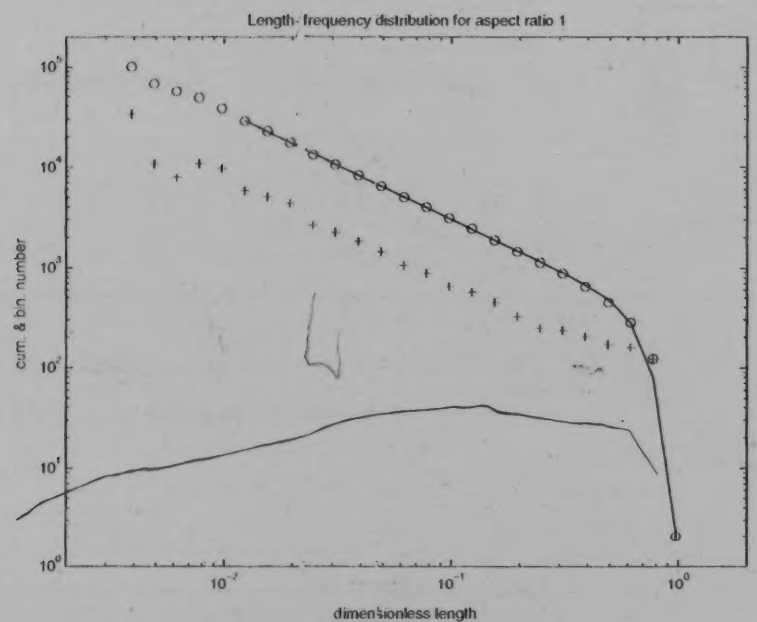

Figure 3.39: Top: moment-frequency distribution. Bottom: length-frequency distribution. Fitting curve (-), cumulative (o) and bin distribution (+).

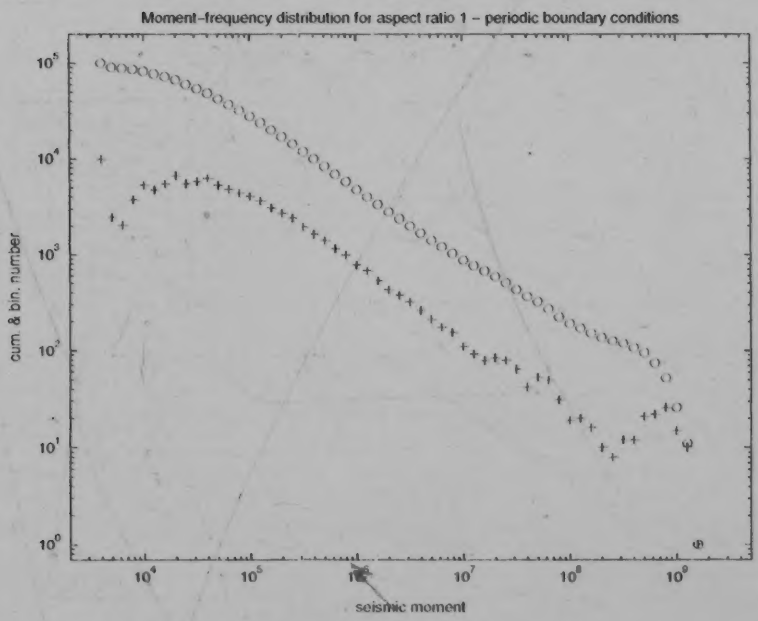

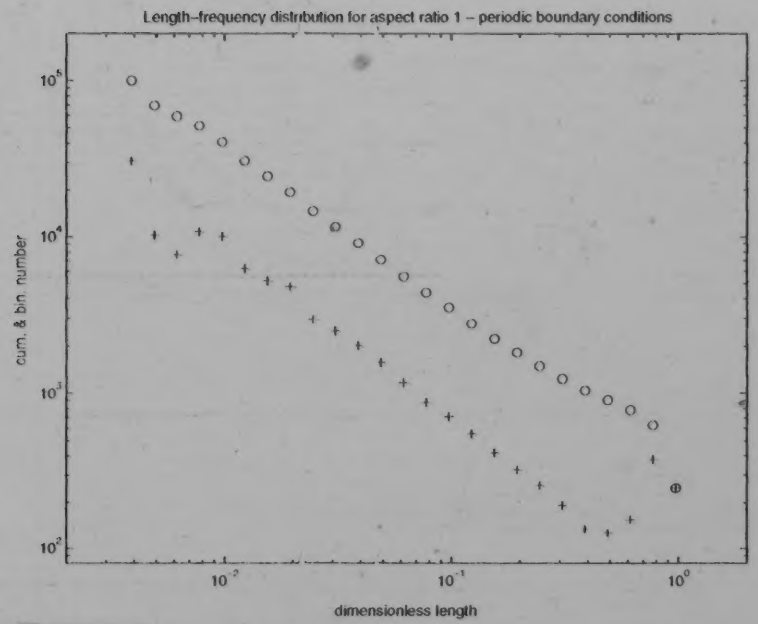

Figure 3.40: Top: moment-frequency distribution. Bottom: length-frequency distribution. Cumulative (o) and bin distribution (+).

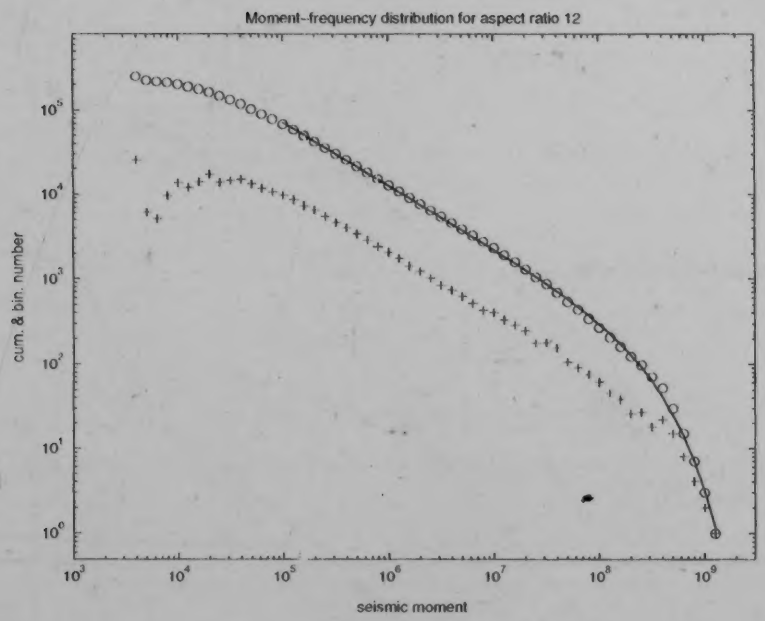

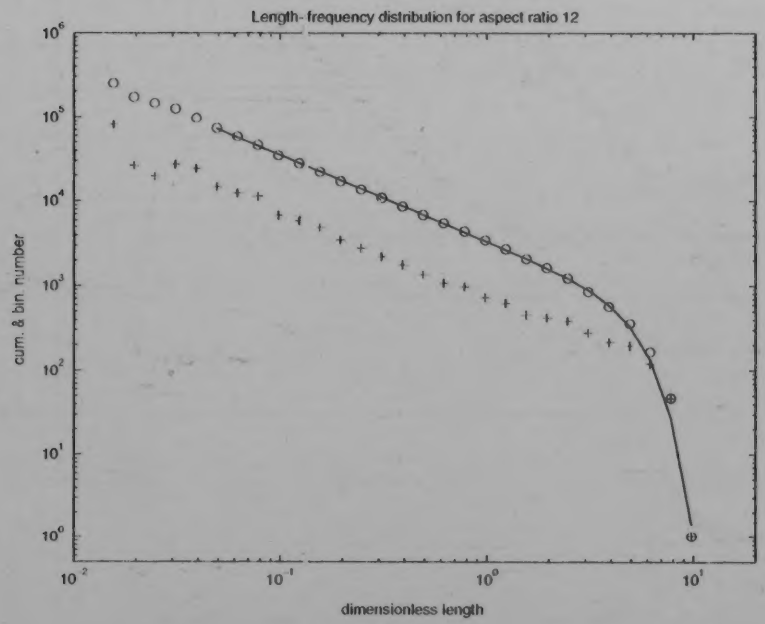

Figure 3.41: Top: moment-frequency distribution. Bottom: length-frequency distribution. Fitting curve (-), cumulative (o) and bin distribution (+).

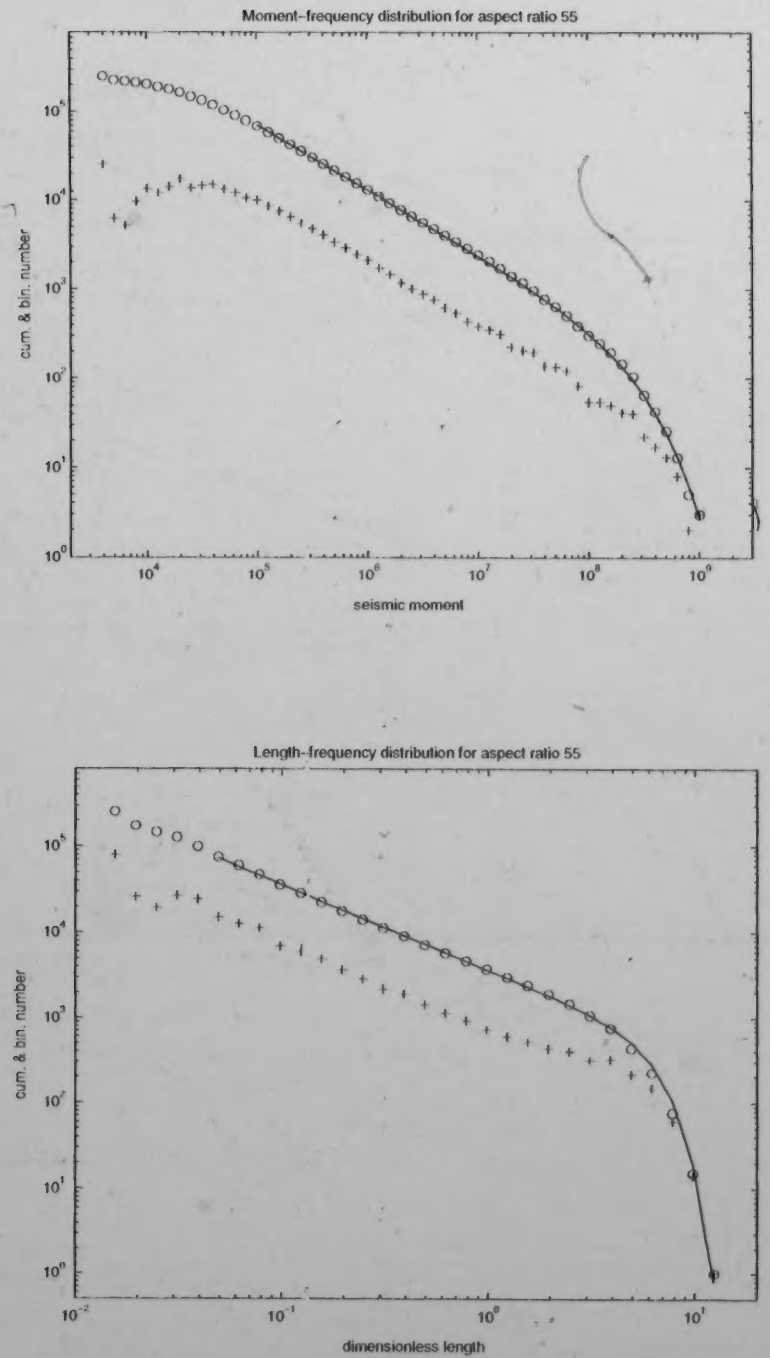
Moment-frequency distribution for aspect ratio 55
cum. & bin. number
seismic moment
Length-frequency distribution for aspect ratio 55
cum. & bin. number
dimensionless length

Figure 3.42: Top: moment-frequency distribution. Bottom: length-frequency distribution. Fitting curve (-), cumulative (o) and bin distribution (+).

3.6 Discussion

Here we discuss the results and their connection to the general observations for the main transform features in the North East Pacific plate boundary region.

Moment-frequency distributions

Most of the studied features ($QC, RD, So, No, SoNo$, and $RDSoNo$) characterize moment-frequency distributions fitted by modified GR relation. The Bl, and Me magnitude distributions show clear characteristic behavior. For the latter two, we used a different database with different reported magnitudes than for the rest of the faults.

Comparing our results to former studies of Hyndman and Wiechert, [1983], henceforth HW83, we can see very similar behavior of cumulative distributions of studied features. Only the characteristic behavior of Bl and Me may be more significant in our results. Also, β-values calculated by HW83 for QC, RD, So ($\beta = 0.41, 0.55, 0.42$, respectively) are very close to β values obtained from our calculations $(0.42, 0.58, 0.42)$. However No shows a quite significant difference. While HW83 examination yields for Nootka fault $\beta = 0.75$, our average value for β is only 0.46.

Generally, it is accepted that the b-value should be close to 1, which implies $\beta = 2/3$. The β-value for faults studied here is between 0.4 and 0.6. These values may seem to be rather low. But recent studies, for instance [Frohlich and Davis, 1993], showed that there might be quite a bit of variation in the value for the b parameter. For instance the b-value for shallow strike slip earthquakes from the Harvard catalogue is 0.77 [Frohlich and Davis, 1993], which implies $\beta = 0.51$. This value is close to values obtained in our studies. Also Kagan [1997, 1999], who precisely describes the inefficiency of using the b parameter, shows that β has a quite significant range in its value (0.27 to 1.85). Even with respect to HW83, we can assume that our β values are reasonable.

We have not considered the possible physical meaning of the γ parameter, which gives the steepness of the exponential roll-off. In our analysis γ is quite variable, and the values from data and model fittings differ. The value of γ for QC (the longest fault) is largest. RD and So show the same γ value (lower than QC), and No distributions yield the lowest value of γ.

Parameter λ is an important parameter which gives a measure of the characteristic size of the distribution. Specifically it gives the size (moment or length) for which the value of N (cumulative number) drops off exponentially. The Queen Charlotte fault, which is the

longest fault, has the largest value of λ. The RD, So, No, and their combinations have quite comparable values of λ. This may be related to the fact that their lengths are comparable as well. Though the So is on a geologically difficult region, its statistics behave similarly to the statistics for the simple single fault. Even moment distributions for Nootka fault have most atypical behavior the values of λ are comparable to λs for other studied short faults.

Length-frequency distributions

Cumulative distributions for rupture lengths for the QC, RD, So and the combined regions show the expected shape with change of the statistics around the transition fitted by the previously described curve. Only the distribution for the Nootka fault shows an anomalous shape. The first part is more concave than the power law, and the second part does not show such a strong exponential tail as did the other fault regions.

The parameter λ from length-frequency distributions yields important information about the characteristic rupture length for specific faults. Lambda may vary depending on chosen parameters for moment-length conversion. The most significant of these are width of seismogenic zone and the stress drop. For the QC we choose two widths, 20 km which is the most often referred width [Rogers, 1985] and 30 km, since the thickness of the oceanic crust grows with the distance from the ocean ridge. For the RD, So, No we took the width of 5 km as suggested by the newer studies [Wahlstrom and Rogers,1992; Cassidy and Rogers, 1995].

The stress drop plays an important role in moment-length conversion as well. Since it does not have a unique value (see section 3.4.1 and 2.3), we choose several possibilities. First, we considered quite low value $\sigma = 0.75$ MPa as Scholz [1982] suggest for the strike-slip faults. Then we increased the σ value to compare the rupture length of the maximum earthquake (1949, August 22, mag. =8.1) L_{max} to Rogers' [1985] estimate 450 km. For $W_0 = 30$ km, using $\sigma = 7.5$ MPa we got the maximum rupture length $L_{max} = 92$ km, for $\sigma = 3$ MPa $L_{max} = 178$ km, for $\sigma = 1.009$ MPa $L_{max} = 450$ km and for $\sigma = 0.75$ MPa $L_{max} = 593$ km. Considering $W_0 = 20$ km, we got for $\sigma = 7.5$ MPa $L_{max} = 110$ km, for $\sigma = 3$ MPa $L_{max} = 233$ km, for $\sigma = 1.471$ MPa $L_{max} = 450$ km, for $\sigma = 0.75$ MPa $L_{max} = 864$ km. These calculations imply that the best stress drop choice would be $\sigma = 1.009$ MPA for $W_0 = 30$ km or $\sigma = 1.471$ MPa for $W_0 = 20$ km, since other values lead to either overestimation or underestimation of the rupture length and then consequently the λ parameter.

Another fact influencing the conversion from moment to length is the value of shear

modulus μ. We considered a value of $\mu = 4 \times 10^{10}$ Pa as did Dziak [1991] for the Blanco region, but there are also different estimates $\mu = 3 \times 10^{10}$ Pa ([Scholz, 1982], [Yin and Rogers, 1996]) or $\mu = 2.8 \times 10^{10}$ Pa (in some calculations of Yin and Rogers [1996]).

Certain influence might be also consideration of circular or elliptical shape of the rupture, since in real, heterogeneous Earth the situation is much more complicated.

Examined data for the Queen Charlotte fault showed characteristic length of 468 km (the average of λ for $QC1$ and $QC2$) for the best fit. Since this value for characteristic size is much smaller than the total fault length, we might expect a width saturation on the QC. The other studied faults, Revere-Dellwood, Sovanco and Nootka with significantly lower aspect ratios, have their characteristic lengths comparable or smaller to the total fault lengths. Though both the length and width saturations are possible for these short faults. The length (width) saturation means that the horizontal (vertical) size of the rupture is comparable with the total length (width) of the fault. While in case of width saturation the remaining energy can be released in the horizontal direction, no further horizontal release is possible for length saturation case.

Our calculations of β parameters of length distributions for the first part (β_{L_1}) and β of moment distributions for the corresponding part (β_{M_1}) allow examination of their ratios. As we see from the values in Table 3.1, all calculated ratios are very similar. These values are in good agreement with the theoretical value 3 (theoretical explanation in Chapter 3.4.1). Maximum difference is 5% for $QC1$ ($W_0 = 30$ km, $\sigma = 0.75$ MPa).

Data versus Numerical Models

Next we would like to compare results of the data analysis to the results of numerical modeling. The QC, with its more than 1000 km length, is considered to be a fault with a large aspect ratio ($Ar \sim 30 - 50$), while the RD, So, and No belong to a group with lower aspect ratios ($Ar \sim 10 - 25$). The moment distributions for the data and modeling show some discrepancies. The β-values for moment distributions are significantly (up to 48%) higher for numerical models than for data. Numerical models for all the aspect ratios provide a value for the β parameter in the range 0.73 to 0.78. The value of β from the studied data varies from 0.39 to 0.62. It is probably due to an influence of various factors that cannot be completely included in the numerical models. Therefore the β parameter is regionally dependent [Frohlich and Currie, 1993; Kagan 1997,1999].

The shape of cumulative distributions for the data and for models is in general agreement, except the Nootka fault. No distributions are more like the distributions for $Ar = 1$

with open side boundaries. Since *No* is a complex fault, composed from many shorter segments, it might explain this atypical behavior. Even though the *So* has also different geological structure than the *QC* and *RD*, it does not show any distinct behavior. The γ-value for the $Ar = 55$ and $Ar = 12$ are the same, but differ from the data results. The γ value for $Ar = 1$ is close to the γ for the *No*. The λ-values from numerical models are very close, even the aspect ratios are in big range 12-55. Different situation is from data. The λ_M's for *QC* are significantly larger than λ_M's for short faults.

While length distributions from modeling are well fitted by modified GR relation, the length distributions from data use one curve to fit distribution for small earthquakes and the second curve to fit distribution for large earthquakes. The primary reason for this is the fact that unlike the real data, the numerical simulation is based on a simplified heterogeneous asperity model. The comparison of the data-based results with the numerical model is in the Table 3.3.

Numerical Model	A_r	β	γ	λ [dimensionless]
	1	0.78	0.6	1.0×10^8
	12	0.75	1.0	3.2×10^8
	55	0.73	3.0	2.9×10^8
Data Fault name	A_r	β	γ	λ [Nm]
No	24	0.46	0.7	1.4×10^{19}
So	25	0.42	1.4	2.7×10^{19}
RD	28	0.58	1.4	3.4×10^{19}
QC	56	0.42	3.8	1.1×10^{19}

Table 3.3: Comparison between the results of seismic moment distributions from the numerical model and from the data.

This shows that measuring and analyzing the rupture length would give more precise information about the seismic behavior, and it would consequently lead to better seismic hazard estimation for specific region, than does the seismic moment analysis.

3.7 Error evaluation

There are several possible sources of errors which more or less influence our results.

Some level of uncertainty appears already in the earthquake database, which usually improves with time. Also, using certain type of magnitude gives local specifications to the data. The obtaining of location and the depth of the epicenter are very sensitive features depending on the number of near-by stations.

Also our magnitude-moment conversion introduces some error, since the $M_w(M_L)$ and

also the Hanks and Kanamori's $M_o(M_w)$ relation are empirical. As well, the moment-length conversion has limitations, discussed in previous sections (specifically, the choice of proper seismogenic fault width, constancy and value for stress drop, value for shear modulus, shape of the rupture, disipation of energy under the seismogenic zone, etc.).

Other sources of errors are the limitations of the numerical models and the fitting method. For fitting the distributions we use the least squares method. Using this method, we calculated standard deviations $\delta\beta$ for the β parameter (for the values see Table 3.1, and Table 3.2). These deviations are up to 3%. But the values for γ and λ are product of iterations in solving two nonlinear equations (for program description see Chapter 3.3.2). This solution is rather dependent on the initial guess for γ which may be another possible error for the results.

Chapter 4

Conclusions

The estimate of the seismic hazard, and the forecasting of earthquakes, is vitally important for the many regions in active seismic zones, with high population density. There are various methods of the hazard evaluation. One possibility is the use of the statistics of the earthquake size distributions. One important factor, which is often neglected, is the geometry of the fault. Here we presented the earthquake size-frequency distributions in dependence on the fault geometry. Observations were also compared to numerical modeling of the seismic activity [Heimpel, 1997; 2003].

From the results of our work and the previous discussion we can conclude the following. Comparing our results to the L and W models (discussed in section 2.3.2) we obtained some interesting results. Although both models agree in scaling for the small earthquakes, they differ in the interpretations for the large earthquake scaling. Although Scholz [1997] proposed different behavior of moment-frequency distributions for single fault and fault population, all QC, RD, So, No moment distributions show very similar shape to Scholz' fault population. Even the QC and RD can be examined as single faults rather than a fault population. Our data yields $\beta = 0.4 - 0.5$ for QC, So, No, and $\beta \sim 0.6$ for RD, which is lower than the L model proposed ($\beta = 2/3$). On the other hand β's for large earthquakes are mostly higher for our data [$QC(\beta \sim 1.6), RD(\beta \sim 1.1), So(\beta \sim 1.4), No(\beta \sim 1.1), SoNo(\beta \sim 1.7), RDSoNo(\beta \sim 1.5)$] than the L model suggests ($\beta = 1$). Transition between distributions should appear at magnitude about 7.5 (according to Pacheco [1992] observations), and we observe it between magnitudes 6 to 8.

In terms of mean slip, the results of numerical models [Heimpel 1997, 2003] are in general agreement with the results of Yin and Rogers [1996], which implies that the mean slip scales approximately linearly with rupture length for smaller aspect ratios (as proposed in the L model). But for the large rupture lengths, the mean slip approaches a constant value and

thus scales with rupture width (as in W model).

Our length distributions confirm the above results, since all length distributions (with the exception of the Nootka fault) were successfully fitted by the proposed curve (for description of fitting parameters see section 3.4.1). Comparing moment and length distributions, all the examined ratios β_{L_i}/β_{M_i} are very close to 3 which is in agreement with L model as well [Scholz, 1997].

The geometry of the fault does influence the size distributions of the fault. We studied several marine strike-slip faults with different lengths and widths, which imply variability in aspect ratios. Our longest studied fault (1120 km), with relatively simple structure, is the Queen Charlotte fault. Considering the widths of 20 or 30 km implies aspect ratios 56 or 37, respectively. If we consider the QCs characteristic size the one of the data's best fit (W_0 = 30 km, σ = 1.009 MPa), then this yields the value of 468 km (the average of λ for $QC1$ and $QC2$). Since this value for the characteristic size is much smaller than the total fault length, we might expect a width saturation on the QC. Other strike-slip faults we studied were RD, So and No. Taking the uniform width of 5 km, this would imply the aspect ratios 28 for RD, 25 for So and 24-32 for No (taking the length 120 or 160 km, without or with the part subducting under Vancouver Island). Both the moment and rupture length characteristic sizes were examined. Characteristic lengths are in large range since we did consider different values of stress drop (0.75 MPa, 1.475 MPa). We present average λ values for all regions of specific faults. For RD $\lambda_M = 3.7 \times 10^{19}$ Nm and λ_L = 127, and 66 km (values for two stress drops respectively), for So $\lambda_M = 2.7 \times 10^{19}$ Nm, λ_L = 92, and 48 km, for No $\lambda_M = 1.4 \times 10^{19}$ Nm, λ_L = 48, and 25 km. RD, as a fault with a single fault plane, shows the largest characteristic sizes. So, with shorter total length and a complex structure of short faults and ridges, has smaller characteristic sizes. No is composed of short left lateral faults in a wide zone with accumulated deformation and its specific structure probably cause the atypical shape of size distributions, quite similar to Ar = 1 from numerical models. No's characteristic sizes show the lowest values, despite the length 160 km, which might imply that the subducting part either does not have significant influence or brings some different behavior into strike-slip distributions. Both So and No are in area with high internal deformation. Since characteristic lengths for studied short faults are comparable to total fault lengths, both the length and width saturation are possible for RD, So, and No.

It might be more useful to study rupture length distributions than the traditional statistics. With the knowledge of fault specifications (like the width of seismogenic zone, shear

modulus, mean slip) it is possible to convert the seismic moment to rupture length. Length-frequency distributions, unlike moment distributions, are not simple modified GR relations. In the case of observed rupture lengths it would be possible to determine the transition that corresponds to the width of the seismogenic zone. Rupture length distributions also provide information about the characteristic rupture lengths. A determination of characteristic rupture lengths for certain faults might be more useful for seismic hazard estimates, since it might be easier to predict possible damage.

Finally, it is important to study every fault separately, since the combination of different regions can lead to concealing of important information. In our study the combined regions SoNo and RDSoNo adopted a behavior of one dominant fault. For instance the SoNo fault system shows behavior very similar to So itself. Likewise, the moment-frequency distribution for RDSoNo looks like the distribution for So, with the steeper power law similar to RD. The information for combined regions is not lost, but the specification (as the shape of curve, or individual characteristic size) can be hidden and a complex fault system may behave as a single fault.

Bibliography

[1] http://neic.usgs.gov/neis/general/handouts/.

[2] *Annual Technical Report.* U.S. Geological Survey, 1999.

[3] D.F. Argus and R.G. Gordon. Present tectonic motion across the Coast Ranges and San Andreas fault system in central California. *GSA Bulletin*, 113:1580–1592, 2001.

[4] W. H. Bakun. Seismicity of California's North Coast. *Bull. Seismol. Soc. Am.*, 90:797–812, 2000.

[5] M. Bath. *Introduction to seismology.* Birkhauser Verlag, 1979.

[6] M. Bath. Earthquake magnitude - recent research and current trends. *Earth Sci. Rev.*, 17:315–398, 1981.

[7] T.R. Bruns, A.J. Stevenson, and M.R. Dobson. Gloria investigation of the exclusive economic zone in the Gulf of Alaska and off southeast Alaska: M/V Farnella cruise f7-89-ga, June 14-July 13, 1989. *U.S. Department of Interior, Open File report 92-317*, 1992.

[8] K.E. Bullen. *An introduction to the theory of seismology.* Cambridge Univ. Press, 1965.

[9] G. V. Burbach, C. Frohlich, W. D. Pennington, and T. Matumoto. Seismicity and tectonics of the subducted Cocos Plate. *J. Geophys. Res.*, 89:7719–7735, 1984.

[10] S.M. Carbotte, J. M. Dixon, E. Farrar, E. E. Davis, and R. P. Riddihough. Geological and geophysical characteristics of the Tuzo Wilson Seamounts: implications for plate geometry in the vicinity of the Pacific - North America - Explorer triple junction. *Can. J. Earth Sci.*, 26:2365–2384, 1989.

[11] J. F. Cassidy, R. M. Ellis, and G. C. Rogers. The 1918 and 1957 Vancouver Island earthquakes. *Bull. Seismol. Soc. Am.*, 78:617–635, 1988.

[12] J. F. Cassidy and G. C. Rogers. The rupture process and aftershock distribution of the 6 April 1992 M 6.8 earthquake, offshore British Columbia. *Bull. Seismol. Soc. Am.*, 85:716–735, 1995.

[13] J. F. Cassidy, G. C. Rogers, and F. Waldhauser. Characterization of active faulting beneath the Straight of Georgia, British Columbia. *Bull. Seismol. Soc. Am.*, 90:1188–1199, 2000.

[14] A. Cazenave, B. Lago, and K. Dominh. Geoid anomalies over the north-east Pacific fracture zones from satellite altimeter data. *Geophys. J. R. Astr. Soc.*, 69:15–31, 1982.

[15] R. M. Clowes, D. J. Baird, and S. A. Behler. Crustal structure of the Cascadia subduction zone, southwestern British Columbia, from potential field and seismic studies. *Can. J. Earth Sci.*, 34:317–335, 1997.

[16] E. E. Davis and R. G. Currie. Geophysical observations of the northern Juan de Fuca Ridge system: lessons in sea floor spreading. *Can. J. Earth Sci.*, 30:278–300, 1993.

[17] E. E. Davis and R. P. Riddihough. The Winona Basin: structure and tectonics. *Can. J. Earth Sci.*, 19:767–788, 1982.

[18] R. P. Denlinger. A model for large scale plastic yield of the Gorda Deformation Zone. *J. Geophys. Res.*, 97:15415–15423, 1992.

[19] R. P. Dziak, C. G. Fox, and R. W. Embley. Relationship between the seismicity and geological structure of the Blanco Transform Fault Zone. *Marine Geophys. Res.*, 13:203–208, 1991.

[20] R. P. Dziak, C. G. Fox, R. W. Embley, J. L. Nabelek, J. Braunmiller, and R. A. Koski. Recent tectonics on the Blanco Ridge, eastern Blanco transform fault zone. *Marine Geophys. Res.*, 21:423–450, 2000.

[21] M.R. Fisk, R.A. Duncan, C.G. Fox, and J.B. Witter. Emergence and petrology of the Mendocino Ridge. *Marine Geophys. Res.*, 15:283–296, 1993.

[22] C.M.R. Fowler. *The solid Earth: An introduction to global geophysics.* Cambridge University Press, 1990.

[23] A. Frankel. High frequency spectral falloff of earthquakes, fractal dimension of complex rupture, b value, and the scaling of strength on faults. *J. Geophys. Res.*, 96:6291–6302, 1991.

[24] Frohlich and Davis. Teleseismic b values; or much ado about 1.0. *J. Geophys. Res.*, 98:631–644, 1993.

[25] B. Gutenberg and C. F. Richter. Frequency of earthquakes in California. *Bull. Seismol. Soc. Am.*, 34:185–188, 1944.

[26] B. Gutenberg and C. F. Richter. *Seismicity in the Earth and Related Phenomena.* 2nd edn, Princeton Univ. Press, Princeton, NJ, 1954.

[27] M. Hamdache, M. Bezzeghoud, and A. Mokrane. Estimation of seismic hazard parameters in the northern part of Algeria. *Pure appl. geophys.*, 151:101–117, 1998.

[28] T.C. Hanks and H. Kanamori. A moment magnitude scale. *J. Geophys. Res.*, 48:2348–2350, 1979.

[29] M. Heimpel. Earthquake size-frequency relations from an analytical stochastic rupture model. *J. Geophys. Res.*, 101:22435–22448, 1996.

[30] M. Heimpel. Critical behavior and the evolution of fault strength during earthquake cycles. *Nature*, 388:865–868, 1997.

[31] M. Heimpel and P. Malin. Aseismic slip in earthquake nucleation and self-similarity: evidence from Parkfield, California. *Earth Plan. Scie. Lett.*, 157:249–254, 1998.

[32] M.H. Heimpel. Characteristic scales of earthquake rupture from numerical models. *Geoph. J. Int., submitted*, 2003.

[33] E. E. E. Hooft and R. S. Detrick. Relationship between axial morphology, crustal thickness and mantle temperature along the Juan de Fuca and Gorda Ridges. *J. Geophys. Res.*, 100:22499–22508, 1995.

[34] R. D. Hyndman. The lithoprobe corridor across the Vancouver Island continental margin: the structural and tectonic consequences of subduction. *Can. J. Earth Sci.*, 32:1777–1802, 1995.

[35] R.D. Hyndman and R. M. Ellis. Queen Charlotte fault zone: microearthquakes from a temporary array of land stations and ocean bottom seismographs. *Can. J. Earth Sci.*, 18:776–788, 1981.

[36] R.D. Hyndman, G.C. Rogers, M.N. Bone, C.R.B. Lister, U.S. Wade, D.L. Barrett, E.E. Davis, T. Lewis, S. Lynch, and D. Seemann. Geophysical measurements in the region of the Explorer Ridge off western Canada. *Can. J. Earth Sci.*, 15:1508–1525, 1979.

[37] R.D. Hyndman and D. H. Weichert. Seismicity and rates of relative motion on the plate boundaries of western North America. *Geoph. J. R.*, 72:59–82, 1983.

[38] Y.Y. Kagan. Seismic moment-frequency relation for shallow earthquakes: regional comparison. *J. Geophys. Res.*, 102:2835–2852, 1997.

[39] Y.Y. Kagan. Universality of the seismic moment-frequency relation. *Pure appl. geophys.*, 155:537–573, 1999.

[40] F. Kundracik. *Spracovanie experimentalnych dat.* MFF UK, 1997.

[41] T. Lay and T.C. Wallace. *Modern Global Seismology.* Academia Press, 1995.

[42] C. R. B. Lister. Plate-tectonics at an awkward junction - rules for the evolution of Sovanco ridge area, NE Pacific. *Geophys. J. - Oxford*, 96:191–201, 1989.

[43] D. J. Merriits. The Mendocino triple junction: Active faults, episodic coastal emergence and rapid uplift. *J. Geophys. Res.*, 101:6051–6070, 1996.

[44] E.A. Okal and S.H. Kirby. Frequency-moment distribution of deep earthquakes; implication for the seismogenic zone at the bottom of slabs. *Phys. Earth Planet. Inter.*, 92:169–187, 1995.

[45] E.A. Okal and B.A. Romanowicz. On the variation of b-values with earthquake size. *Phys. Earth Planet. Inter.*, 87:55–76, 1994.

[46] J. Pacheco, C.H. Scholz, and L.R Sykes. Change in frequency-size relationship from small to large earthquakes. *Nature*, 355:71–73, 1992.

[47] R. Palmer, R. Weldon, E. Humpreys, and F. Saucier. Earthquake recurrence on the southern San Andreas modulated by fault-normal stress. *Geophys. Res. Lett*, 22:535–538, 1995.

[48] M. D. Petersen and S. G. Wesnousky. Fault slip rates and earthquake histories for active faults in southern California. *Bull. Seismol. Soc. Am.*, 84:1608–1649, 1994.

[49] C. Qin, E.E. Papadimitriou, B.C. Papazachos, and G.F. Karakaisis. Spatial distribution of time dependent seismicity in China. *Pure appl. geophys.*, 154:101–119, 1999.

[50] R. P. Riddihough. A model for recent plate interactions off Canada West Coast. *Can. J. Earth Sci.*, 14:384–396, 1977.

[51] R. P. Riddihough and R.D. Hyndman. *Modern plate tectonic regime of the continental margin of Western Canada*, chapter 13, in Geol. of the Cordillerean Orogen, pages 435–455. Geolog. Survey Canada, Geology of Canada no. 4, 1991.

[52] K. M. M. Rohr, M. Scheidhauer, and A. M. Trehu. Transpression between two warm mafic plates: The Queen Charlotte revisited. *J. Geophys. Res*, 105:8147–8172, 2000.

[53] B. Romanowicz and J.B. Rundle. Short notes on scaling relations for large earthquakes. *Bull. Seismol. Soc. Am.*, 83:1294–1297, 1993.

[54] J.B. Rundle. Derivation of the complete Gutenberg-Richter magnitude-frequency relation using the principle of scale invariance. *J. Geophys. Res*, 94:12337–12342, 1989.

[55] C.H. Scholz. The frequency-magnitude relation of microfracturing in rock and its relation to earthquakes. *Bull. Seismol. Soc. Am.*, 72:399–415, 1968.

[56] C.H. Scholz. Scaling laws for large earthquakes: consequences for physical models. *Bull. Seismol. Soc. Am.*, 72:1–14, 1982.

[57] C.H. Scholz. *The mechanics of earthquakes and faulting.* Cambridge Univ. Press, 1990.

[58] C.H. Scholz. *Earthquakes and faulting: self-organized critical phenomena with a characteristic dimension*, chapter in Spontaneous Formation of Space-Time Structures and Criticality, T Riste and D. Sherington, eds., pages 41–56. Kluwer Academic Publishers, Netherlands, 1991.

[59] C.H. Scholz. Size distribution for large and small earthquakes. *Bull. Seismol. Soc. Am.*, 87:1074–1077, 1997.

[60] C.H. Scholz and C.A. Aviles. *The fractal geometry of faults and faulting*, pages 147–155. in Earthquake Source Mechanism, AGU monograph, 1986.

[61] D. P. Schwartz and K. J. Coppersmith. Fault behavior and characteristic earthquakes: examples from the Wasatch and San Andreas Fault Zones. *J. Geophys. Res.*, 89:5681–5698, 1984.

[62] M.M. Sobiesiak. Fault plane structure of the antofagasta, Chile earthquake of 1995. *Geophys. Res. Lett.*, 27:581–584, 2000.

[63] C. Stock and E.G.C. Smith. Evidence for different scaling of earthquake source parameters for large earthquakes depending on faulting mechanism. *Geophys. J. Int.*, 143:157–162, 2000.

[64] M. Sylvander. Identifying an asperity through 3-D mapping of the frequency-magnitude distribution. *Geophys. Res. Lett.*, 26:2657–2660, 1999.

[65] D.L. Turcotte. *Fractals and Chaos in Geology and Geophysics.* Cambridge Univ. Press, 1997.

[66] T. Utsu. Representation and analysis of the earthquake size distribution: A historical review, and some new approaches. *Pure appl. geophys.*, 155:509–535, 1999.

[67] R. Wahlstrom and G.C. Rogers. Relocation of earthquakes west of Vancouver Island, BC, 1965-1983. *Can. J. Earth Sci.*, 29:953–961, 1992.

[68] S.G. Wesnousky. The Gutenberg-Richter or characteristic earthquake distribution, which is it? *Bull. Seismol. Soc. Am.*, 84:1940–1959, 1994.

[69] S.G. Wesnousky. Crustal deformation processes and the stability of the Gutenberg-Richter relationship. *Bull. Seismol. Soc. Am.*, 89:1131–1137, 1999.

[70] S.G. Wesnousky, C.H.Scholz, K. Shimazaki, and T. Matsuda. Earthquake frequency distribution and the mechanics of faulting. *J. Geophys. Res.*, 88:9331–9340, 1983.

[71] S. Wiemer and M. Wyss. Mapping the frequency-magnitude distribution in asperites: An improved technique to calculate recurence times? *J. Geophys. Res.*, 102:15115–15128, 1997.

[72] Z.L. Wu. Frequency-size distribution of global seismicity seen from broad-band radiated energy. *Geophys. J. Int.*, 142:59–66, 2000.

[73] Z.M. Yin and G.C. Rogers. Toward a physical understanding of earthquake scaling relations. *Pageoph.*, 146:661–675, 1996.